



PT Symmetry and Exceptional Points in Metamaterials

James Gear

M.Sci

A thesis submitted to
The University of Birmingham
for the degree of
Doctor of Philosophy

Metamaterials Research Centre
School of Physics and Astronomy
College of Engineering and Physical Sciences
The University of Birmingham

UNIVERSITY OF
BIRMINGHAM

University of Birmingham Research Archive

e-theses repository

This unpublished thesis/dissertation is copyright of the author and/or third parties. The intellectual property rights of the author or third parties in respect of this work are as defined by The Copyright Designs and Patents Act 1988 or as modified by any successor legislation.

Any use made of information contained in this thesis/dissertation must be in accordance with that legislation and must be properly acknowledged. Further distribution or reproduction in any format is prohibited without the permission of the copyright holder.

Abstract:

Parity-Time (PT) symmetry has recently received much attention as an alternative to the condition of Hermiticity. PT symmetric systems have two distinct phases where behaviour is split between Hermitian evolution and non-Hermitian evolution. These two phases are connected by an exceptional point (EP): a special kind of eigenvalue degeneracy unique to non-Hermitian systems.

In this thesis, we will first examine metamaterials and show how they can be used to design electromagnetic potentials. We will also examine the current understanding of PT symmetry in electromagnetism. A new parity operator will then be developed, which can be used to derive generalized PT symmetry conditions on the constitutive matrix. The new parity operator is then used to link PT symmetry and EPs. The constitutive matrix has multiple potentials, unlike the single potential of quantum mechanics. Metamaterials allow us to access all of these potentials, giving us a flexible platform for studying PT symmetry and EPs. Using bianisotropic metamaterial structures, we have experimentally observed a PT-phase transition and the unidirectional zero reflection associated with an EP. We will additionally look at some other applications of PT symmetry in the context of lasing and absorption and attempt to design a structure which uses this symmetry.

Papers:

James Gear, Fu Liu, S.T. Chen, Stefan Rotter and Jensen Li, "Parity-time symmetry from stacking purely dielectric and magnetic slabs", Phys. Rev. A 91, 033825 (2015).

Shiyi Xiao, James Gear, Stefan Rotter and Jensen Li, "Effective PT-symmetric metasurfaces for subwavelength amplified sensing", New J. Phys. 18, 085004 (2016).

Shiyi Xiao, Yong Sun, Liwen Zhang, James Gear, Richard Fitzgerald, Stefan Rotter, Hong Chen and Jensen Li, "Observation of PT-symmetric exceptional point from magnetoelectric bianisotropy" (PIERS 2016 conference abstract).

James Gear, Yong Sun, Shiyi Xiao, Liwen Zhang, Richard Fitzgerald, Stefan Rotter, Hong Chen and Jensen Li, "Unidirectional zero reflection as gauged parity-time symmetry", submitted (arXiv version available at: <https://arxiv.org/ftp/arxiv/papers/1707/1707.09413.pdf>).

Declaration:

This thesis has been written entirely by myself and I have made efforts to ensure that any work from other sources other than myself have been properly referenced. The new results in this thesis are displayed in chapter 4.6 and 4.7 with the parity redefinition and the link between exceptional points and PT symmetry. Extensions and realisations of these are shown in chapter 5 (theoretical work) and chapter 6 (experimental work) respectively.

My contribution in section 4.7 and 4.8 was to derive the gauge transformations for E^+ and E^- fields, to derive the general condition on the constitutive parameters for gauged PT symmetry and to associate unidirectional zero reflection with PT symmetric contours. In chapter 5 my contribution was to derive the P and T transformations on the effective constitutive matrix, find the condition for an exceptional point in the two-slab system without using gain and confirm it in simulation, assist in the formulation of the coherent lasing and absorbing conditions and the effect of parity and time reversal transformations on scattering states (in collaboration with Shiyi Xiao), and assisting in the theoretical design of an amplified sensing surface (in collaboration with Shiyi Xiao).

In chapter 6 the laser-absorber designs were a collaboration between Shiyi Xiao and myself using CST Microwave Studio, the designs were fabricated at Shenzhen Sunsoar Electronic Co., Ltd, and the measurements and analysis were done by myself. The bianisotropic transmission line was designed by myself, fabricated at Shenzhen Sunsoar Electronic Co. and measurements were taken by myself. Analysis of the results was done by Jensen Li and myself.

Acknowledgements:

I would like to thank my supervisor, Dr. Jensen Li, for his encouragement of my research and for sharing his many insights with me. His patience and understanding have helped me greatly during my studies and I owe him a great deal. I extend similar gratitude to Dr. Shiyi Xiao, who was keen to share advice during our collaborations on the laser-absorber. His dedication was an inspiration to me and our discussions on the culture and history of our countries were enlightening and enjoyable.

I would also like to thank Dr. Fu Liu for his help in the initial stage of my PhD, as he helped me get to grips with the simulation software and mathematics we were using. He was quite welcoming during this time and introduced me to my favourite Chinese dish (Hong Shao Rou), for which I am very grateful. In a similar vein, I would also like to thank Dr. Teun-Teun Kim for his friendly demeanour during my first few years at Birmingham. I learned many things about Korea and postdoc life during our lunchtime conversations.

I thank Professor Shuang Zhang and the Metamaterials Research Group in general for their hard work and willingness to help me when needed. I learned a lot about science and research in general through our conversations.

I also appreciate the financial support of the Engineering and Physical Sciences Research Council and the administrative support of the University of Birmingham for enabling me in my studies.

Finally, I would like to thank my family for their continuous, loving support.

Table of Contents:

Abstract:	i
Papers:	ii
Declaration:	iii
Acknowledgements:	iv
Table of Contents:	v
Table of Figures:	vii
1. Introduction:	1
1.1. Motivation:	1
1.2. Thesis structure:	3
2. Functionalities of Metamaterials: theory and background:	5
2.1. Maxwell's equations and the constitutive parameters:	5
2.2. Properties of Metamaterials:	12
2.3. Oscillating electrons and the Lorentz model:	24
2.4. Artificial electric and magnetic resonating structures:	28
2.5. Chapter Summary:	36
3. Extracting the Constitutive Matrix and the Effects of Symmetries:	38
3.1. Modified Effective Medium Extraction for Bianisotropic Materials:	38
3.2. Effective Medium of Stratified Layers:	47
3.3. Spatial, Temporal and Other Symmetries:	49
3.3.1. Mirror Inversion (parity):	49
3.3.2. Rotation:	53
3.3.3. Time-reversal:	54
3.3.4. Electric-Magnetic Duality:	57
3.3.5. Reciprocity:	58
3.3.6. Hermiticity:	59
3.4. Chapter Summary:	61
4. Parity-Time Symmetry and Parity Redefinition:	63
4.1. Early Developments and Background:	63
4.2. PT Symmetry in Quantum Mechanics and the Link to Optics:	67
4.3. Perpendicular PT Symmetry:	69
4.4. Tangential PT Symmetry:	72
4.5. Azimuthal PT Symmetry:	74
4.6. PT Symmetry Without Gain:	76

4.7. Parity Redefinition via a Gauge Transformation:	77
4.8. Unidirectional Zero Reflection and the Link to PT Symmetry:	82
4.9. Chapter Summary:.....	86
5. Properties of PT Symmetric Metamaterials:	87
5.1. PT Symmetric Effective Medium:	87
5.2. Bandstructure of the PT Symmetric Medium:	89
5.3. Exceptional Points and Unidirectional Zero Reflection:.....	92
5.4. Lasing and Coherent Perfect Absorption:	96
5.5. Parity and Time Reversal Transformations on Lasing and Absorbing States:	99
5.6. Lasing and Absorption on PEC and PMC substrates:.....	102
5.7. Amplified sensing:	103
5.8. Chapter Summary:.....	106
6. Realising PT Symmetric Metamaterials with Transmission Line Structures:	108
6.1. Bianisotropic PT symmetric Transmission Line:	108
6.2. Using Tunnel Diodes to Produce Gain:.....	115
6.3. A Transmission Line Laser-Absorber:	117
6.4. Chapter Summary:.....	128
7. Conclusions and Outlook:.....	130
Appendix A: Resonance Shifting via Coupling	132
References:.....	134

Table of Figures:

Figure 1: One-dimensional electromagnetic wave propagation.....	6
Figure 2: Surface plasmons and the Lycurgus cup.	13
Figure 3: Two examples of gradient index devices.	15
Figure 4: Examples of complementary media.....	17
Figure 5: Examples of various chiral metamaterial unit cells.....	19
Figure 6: Examples of bianisotropic metamaterials.....	21
Figure 7: The effect of the Kramers-Kronig relations on enforced non-dispersivity.	22
Figure 8: A plot of the real (black line) and imaginary (red line) parts of the permittivity given by the Lorentz oscillator model.....	27
Figure 9: Simulated absolute value of the electric field around a bar resonator.	30
Figure 10: Dependence of ωr on the lattice constant.	31
Figure 11: Comparison of a ring, split ring and concentric split ring resonator.....	33
Figure 12: Unit cell of a designed negative index metamaterial.	35
Figure 13: Illustration of the reference plane collapse process.....	42
Figure 14: Example transmission line structure and its S parameters.....	44
Figure 15: Extracted χ_e and χ_m for the example transmission line structure.....	45
Figure 16: Mathematical representation of a section of a transmission line of length Δz and the associated voltages (V) and currents (J) at the ends of the section.	46
Figure 17: Illustration of the effects of a parity on the magnetic field.	50
Figure 18: Real energy eigenvalues of the Hamiltonian $H = p^2 - ixN$	63
Figure 19: Modes in a coupled PT waveguide system.	71
Figure 20: Eigenvalue plots for an example longitudinal PT symmetric system.....	73
Figure 21: Schematic and spectrum of a microring laser.....	75
Figure 22: PT exceptional point in system with non-symmetric but matched gain/loss profile.	81
Figure 23: PT symmetry in an adjusted constant intensity system.....	85
Figure 24: Material profile and bandstructure of the $P\pi/4T$ symmetric system.....	90
Figure 25: forwards and backwards reflectance for four, PT symmetric unit cells.	91
Figure 26: A comparison of UZR merit ρ (colour map) and exceptional points (black lines) in the effective medium matrix.....	93
Figure 27: Plots of the real and imaginary parts of the eigenvalues of C^{-1} (labelled as c_{i-1}) as a function of the gain/loss parameter γ	95
Figure 28: Confirming PT symmetry for the passive system.....	96
Figure 29: Illustration of a scattering system and the effects of the P and T operators on inputs.	100
Figure 30: Illustration of the correspondence between symm./asymm. inputs and PMC/PEC boundary conditions.....	103
Figure 31: Effective medium extraction and absorption properties of the amplified sensing surface.	105
Figure 32: Diagram and simulation schematic of the bianisotropic transmission line structure.	108
Figure 33: Experimental setup for the bianisotropic transmission line.	109
Figure 34: Photos of the unshifted and shifted transmission line structures and the extracted constitutive parameters of the shifted structure.....	110
Figure 35: The real (left four panels) and imaginary (right four panels) of the constitutive matrix elements as a function of the electric atom resistance (R) and the frequency in GHz (f), before gauging.	111

Figure 36: The constitutive matrix after choosing a gauge to have $\text{Re}(\chi_e)=\text{Re}(\chi_m)$, as a function of the electric atom resistance and the frequency in GHz (f).....	113
Figure 37: Unidirectional zero reflection merit and eigenvalue plots.	114
Figure 38: properties of a TD261 tunnel diode.	116
Figure 39: Detailed schematic of the original laser-absorber design.	118
Figure 40: Initial laser-absorber design and ideal simulation setup.	119
Figure 41: Simulated properties of the Initial laser-absorber design.	120
Figure 42: Pictures of the initial samples.	121
Figure 43: Comparison of the scattering parameters of the initial laser-absorber for experiment and simulation.....	122
Figure 44: Equivalent circuit diagram for the laser-absorber system.....	122
Figure 45: S parameters for the laser-absorber (with the diode) for different diode bias voltages. .	123
Figure 46: Redesigned laser-absorber.....	124
Figure 47: Magnitude of the [S] matrix components of the adjusted laser-absorber with a TD261 tunnel diode biased to 280mV.....	125
Figure 48: Scattered field magnitudes and constitutive parameters of the new LA design.....	126
Figure 49: Three electric resonators of different sizes and their properties.	127
Figure 50: Resonance shifting in the dipolar model.	133

1.Introduction:

1.1. Motivation:

Symmetries have always played an important role in physics. Not only do they allow for shortcuts in analysis but in certain circumstances, they allow for the identification of conserved quantities when the system is invariant (i.e. symmetric) under a certain transformation. For example, spatial translation symmetry implies the conservation of momentum and invariance under a rotation implies the conservation of angular momentum. A property related to symmetry is that of Hermiticity, a property of operators and matrices that guarantees real eigenvalues from their eigenstates. This property is not a space-time symmetry like those mentioned above but rather a mathematical symmetry of an operator. Hermiticity is extremely important in quantum mechanics, as a Hermitian Hamiltonian (i.e. energy) operator will result in the system's time evolution being unitary and means that any observed quantities will be described by real numbers. Unitary evolution means that probabilities are conserved, which is important because we do not want a system containing one electron to evolve into a state with 1.4 or 0.1 electrons. This probability conserving property is not limited to quantum mechanics; Hermitian operators can describe unitary evolution in many systems, such as fluid mechanics or electromagnetism (the latter of which will be the focus of this thesis).

While quantum mechanics has Hermiticity as one of its fundamental postulates, the realisation of Hermitian systems in electromagnetism is often hard. This is due to mechanisms such as Ohmic loss, where an electric field (static or oscillating) can have some of its energy

converted into phonons or heat via the interaction of electrons with the lattice in which they flow. This is obviously a problem for people wishing to achieve lossless systems (e.g. electrical power transmission, data transmission or high Q resonators). There is, however, another symmetry, related to Hermiticity, that can also give real eigenvalues for eigenstates: combined symmetry under the parity (spatial inversion) and time reversal transformations, a.k.a. PT symmetry [1]. This symmetry is characterized by the fact that any loss in some region of the system must be balanced by an equal amount of gain in the mirror counterpart of that region, implying that the system has no net gain or loss and the overall behaviour should look Hermitian. PT symmetric systems, however, have richer behaviour than simply Hermitian mimicry. They have two distinct phases when an external parameter of the system is varied: one where the system's eigenvalues are real and the evolution is unitary, and another where the system breaks from this Hermitian behaviour and non-unitary evolution can be observed. The crossing between these two points is called an exceptional point and passing through this can result in rapid changes in the system. Exceptional points can also be related to interesting phenomena such as unidirectional zero reflection and invisibility. This rapid change in behaviour also has possible applications in switching technology (e.g. optical computers).

In contrast to quantum mechanics, which only has a single potential, electromagnetism has multiple potentials describing the interaction of electric and magnetic fields with a medium. These potentials are known as constitutive parameters. To achieve PT symmetry, one must design the constitutive parameters of the system so that this symmetry can be established. To assist in this designing process, we turn to one of the most significant advancements in modern electromagnetism: metamaterials. Metamaterials, whose prefix "meta" comes from the Greek word for "beyond" or "after", are artificial materials composed of designed,

repeating structures known as unit cells. These unit cells are usually composed of some kind of metal structure embedded in a substrate medium and can imbue the bulk metamaterial with properties that are difficult (or in some cases, impossible) to realise with naturally occurring materials. Examples of these properties include strong chirality/bianisotropy [2], strong spatial dispersion [3] and a negative refractive index [4]. In light of the array of constitutive parameters made available by metamaterials, we hope to use them as a flexible platform to study PT symmetry in electromagnetism and the exceptional points associated with it.

1.2. Thesis structure:

The structure of this thesis is as follows: Section 2 is a review of the properties of metamaterials which starts with a basic introduction to Maxwell's equations and the constitutive parameters, then looks at the history, functionality and limitations of metamaterials, with some extra information on the mathematical modelling of metamaterial resonances using the Lorentz model and a guide to designing a metamaterial unit cell. Section 3 deals with extracting an effective constitutive matrix from scattering parameters, with discussion on various conventions for the effective medium. We additionally look at some common symmetries and how we can use these symmetries (or lack thereof) to predict the form of an extracted effective constitutive matrix. Section 4 looks at parity-time (PT) symmetry, starting with a brief discussion of its origins in quantum mechanics, then moving on to its use in electromagnetism. We also look at how to define PT symmetry using the constitutive and scattering matrices and how we can achieve PT symmetry without using gain.

To finish the section, we develop a unitary transformation which can be combined with the parity operator to produce new, ‘gauged’ PT symmetry conditions and we show how the phenomenon of unidirectional zero reflection can be related to PT symmetry in the constitutive matrix. In section 5, we develop two specific examples of PT symmetric systems and examine their properties analytically: the first is a PT symmetric two-slab system whose material properties are derived from the combination of the new parity operator with the time reversal operator. The second is a system known as a laser-absorber: a structure which can support lasing and coherent perfect absorption simultaneously and whose lasing and absorbing states can be related through our gauged PT symmetry. We show that such a structure could have use in sensing applications. In section 6, we seek experimental verification of our link between unidirectional zero reflection and PT symmetry, to do this we design a tuneable, bianisotropic transmission line structure containing two exceptional points, prove that the constitutive matrix structure is PT symmetric along contours of its phase space and that the unidirectional zero reflection points lie on these contours. We will also look at some attempts at the experimental realisation of the laser-absorber, starting with some data on tunnel diodes used in the structure, then looking at the design and simulated properties and then examining the properties of the fabricated structures.

2. Functionalities of Metamaterials: theory and background:

2.1. Maxwell's equations and the constitutive parameters:

In order to talk about metamaterials, we must discuss how they affect the propagation of light. The propagation of electromagnetic waves through a medium is modelled by Maxwell's equations. These equations relate the spatial variation of the incident electric and magnetic fields (\mathbf{E} and \mathbf{H}) to the temporal variation of the displacement and magnetic flux fields (\mathbf{D} and \mathbf{B}). Maxwell's equations in the \mathbf{E}/\mathbf{H} basis are given by:

$$\nabla \times \mathbf{E} = -\frac{\partial \mathbf{B}}{\partial t} = -\frac{\partial}{\partial t} \mu_0 (\mathbf{H} + \mathbf{M}) \quad (2.1)$$

$$\nabla \times \mathbf{H} = \frac{\partial \mathbf{D}}{\partial t} + \mathbf{J} = \frac{\partial}{\partial t} \epsilon_0 (\mathbf{E} + \mathbf{P}) + \mathbf{J} \quad (2.2)$$

where ϵ_0 and μ_0 are the permittivity and permeability of vacuum, \mathbf{J} is the current density (which can be absorbed into the displacement field) and we have introduced the electric polarizability, \mathbf{P} , and the magnetisation, \mathbf{M} (bold type denotes a vector). The \mathbf{D} and \mathbf{B} fields can be related to the \mathbf{E} and \mathbf{H} fields via the constitutive relations:

$$\begin{pmatrix} \mathbf{E} \\ \mathbf{H} \end{pmatrix} = [\mathbf{C}] \cdot \begin{pmatrix} \mathbf{D} \\ \mathbf{B} \end{pmatrix} \quad (2.3)$$

where the square brackets denote a matrix and the dot represents a matrix multiplication. In this thesis, we will mostly be concerned with propagation in a single direction. If we choose this direction to be the z axis, as depicted in Figure 1, and assume that we have no electric field in the z direction (i.e. we have plane wave incidence) and no x/z or y/z coupling terms in our constitutive relations, then we can write these equations as:

$$\partial_z \begin{pmatrix} 0 & 0 & 0 & -1 \\ 0 & 0 & 1 & 0 \\ 0 & 1 & 0 & 0 \\ -1 & 0 & 0 & 0 \end{pmatrix} \cdot \begin{pmatrix} E_x \\ E_y \\ H_x \\ H_y \end{pmatrix} = \frac{\partial}{\partial t} [C]^{-1} \cdot \begin{pmatrix} E_x \\ E_y \\ H_x \\ H_y \end{pmatrix} \quad (2.4)$$

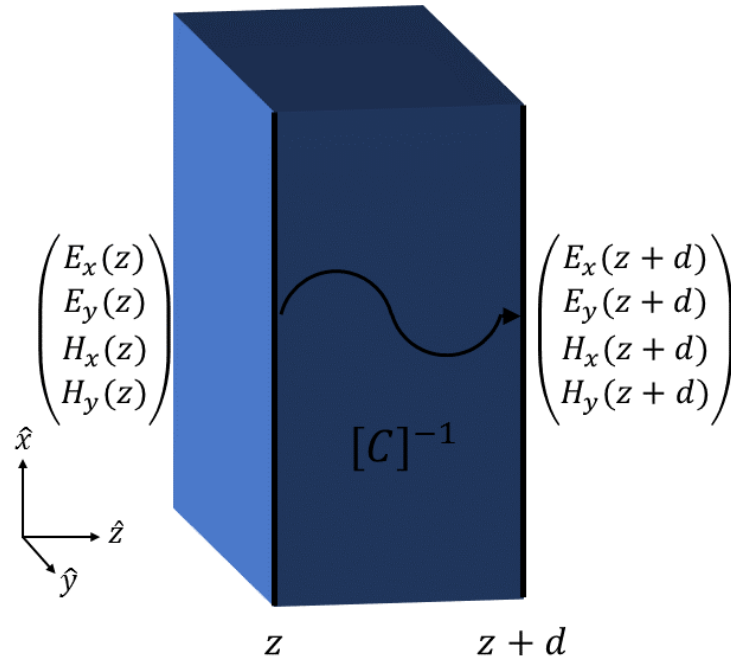


Figure 1: One-dimensional electromagnetic wave propagation. This shows the conventions for the propagation of an electromagnetic wave from z to $z + d$ through a medium described by $[C]^{-1}$. The solutions for $E_i(z + d)$ and $H_i(z + d)$ are given by equation (2.7).

The $[C]^{-1}$ matrix is defined by

$$\begin{pmatrix} D_x \\ D_y \\ B_x \\ B_y \end{pmatrix} = \begin{pmatrix} \epsilon_{xx} & \epsilon_{xy} & \xi_{xx} & \xi_{xy} \\ \epsilon_{yx} & \epsilon_{yy} & \xi_{yx} & \xi_{yy} \\ \zeta_{xx} & \zeta_{xy} & \mu_{xx} & \mu_{xy} \\ \zeta_{yx} & \zeta_{yy} & \mu_{yx} & \mu_{yy} \end{pmatrix} \cdot \begin{pmatrix} E_x \\ E_y \\ H_x \\ H_y \end{pmatrix} = [C]^{-1} \cdot \begin{pmatrix} E_x \\ E_y \\ H_x \\ H_y \end{pmatrix} \quad (2.5)$$

These parameters (ϵ_{ij} , μ_{ij} , ξ_{ij} and ζ_{ij}) are what we will call our constitutive parameters. For most systems, it is reasonable to assume that the constitutive parameters do not vary with time, so that $[C]^{-1}$ is not affected by the time derivative, and that the fields are time harmonic, so we can replace the time derivative by a factor of $-i\omega$. This means that we can rewrite the above equation as

$$\partial_z \cdot \begin{pmatrix} E_x \\ E_y \\ H_x \\ H_y \end{pmatrix} = i\omega \begin{pmatrix} 0 & 0 & 0 & 1 \\ 0 & 0 & -1 & 0 \\ 0 & -1 & 0 & 0 \\ 1 & 0 & 0 & 0 \end{pmatrix} \cdot [C]^{-1} \cdot \begin{pmatrix} E_x \\ E_y \\ H_x \\ H_y \end{pmatrix} = i[K] \cdot \begin{pmatrix} E_x \\ E_y \\ H_x \\ H_y \end{pmatrix} \quad (2.6)$$

This allows us to calculate one dimensional plane wave propagation through a medium described by $[C]^{-1}$ by relating the electric and magnetic fields at some point z to another point $z + d$:

$$\begin{pmatrix} E_x(z+d) \\ E_y(z+d) \\ H_x(z+d) \\ H_y(z+d) \end{pmatrix} = \exp \left(\int_z^{z+d} i[K] dx \right) \cdot \begin{pmatrix} E_x(z) \\ E_y(z) \\ H_x(z) \\ H_y(z) \end{pmatrix} \quad (2.7)$$

This is what is known as the transfer matrix method (TMM). If $[C]^{-1}$ is a function of the coordinate z , then one might expect to be able to get a solution of the form $\psi[z+d] = e^{\int_z^{z+d} K[z'] dz'} \psi[z]$ but this is not the case as transfer matrices do not commute with each other in general. The best way to solve such systems is to split up the region of interest (say, $-d/2 \leq z \leq d/2$) into N sub regions, each with its own homogeneous, averaged $[C]^{-1}$, and multiply them together in order. This means that we can approximate the total transfer matrix as

$$T = \prod_{n=1}^N \exp \left(i\omega \left(\frac{[K](-d/2 + (n-1)d/N) + [K](-d/2 + nd/N)}{2} \right) d/N \right) \quad (2.8)$$

where the capital pi symbol denotes an ordered matrix product and we can have the exact solution in the limit $N \rightarrow \infty$.

It should be noted here that in this thesis we will mainly be using Lorentz-Heaviside units. These units, named after Hendrick Lorentz and Oliver Heaviside, scale Maxwell's equations so that only relative quantities need to be considered (i.e. $\epsilon = \epsilon_r$ and $\mu = \mu_r$). This is done by setting the vacuum permittivity and permeability to unity, meaning that many physical

constants associated with electromagnetic waves (e.g. the speed of light, c , and the impedance of free space, Z_0) will also go to unity. This is useful as it allows one to use relative constitutive parameters freely without having to consider ϵ_0 and μ_0 and makes quantities such as the phase velocity easier to interpret. This unit system also has the useful property that the angular frequency (ω) and the freespace wavenumber (k_0) can be used interchangeably due to the fact that $c = 1$.

As we have seen, the propagation of electromagnetic waves in a medium is primarily governed by the constitutive parameters (equation 2.5 and 2.6). These relate the electric and magnetic fields in vacuum to the effective fields inside a material. For example, the permittivity components, ϵ_{ij} , describes the ability of the j component of the electric field to induce a polarizability in the i direction and the permeability components, μ_{ij} , describe the ability of the j component of the magnetic field to induce a magnetisation in the i direction. To get a deeper understanding of these parameters, we will briefly discuss their physical origins and give some examples of their values in some materials. The permittivity, in insulating materials, can be understood by considering the separation of charges: an electric field imposed on a stationary material will pull electrons in the opposite direction to the positively charged nuclei, creating a set of small dipoles and so an opposing electric field. As a result, the total electric field inside the material is smaller than in its surroundings due to the extra fields from the induced charge separation. This effect can also be seen as the ability of the material to store electric fields in these dipoles, similar to the concept of capacitance. For most bulk materials, the permittivity is greater than the vacuum permittivity ($\epsilon_r > 1$). Some examples of this are glass ($\epsilon_r = 5 - 10$, depending on composition), Teflon ($\epsilon_r = 2.1$), water ($\epsilon_r \sim 80$) and Strontium Titanate ($\epsilon_r = 310$) [5] (note: these permittivities are DC values measured at 20°C).

Materials which form these dipoles when exposed to an electric field are known as dielectrics. The values we have seen so far are all real but the permittivity can be (and generally is) a complex number. Having a complex permittivity will result in a displacement field which is phase-shifted compared to the electric field and is related to the loss in a medium.

Some materials, such as metals, have freely flowing electrons and cannot form dipoles like dielectrics. Electrons in a metal can be approximately modelled as a free electron gas, which means that they are free to move under an applied electric field. We can model the response of a metal by using the Drude model (see section 2.4 for details). This model states that the permittivity of metals for low frequencies will have a large, negative real part, resulting in a large, π -shifted electric field, and a large, positive imaginary part, resulting in rapid, exponential decay of the fields as they propagate through the metal. This is why most metals are opaque to nearly all electromagnetic waves.

For amorphous or disordered materials (such as water or most glasses), the permittivity will not depend on the incident polarization or angle of incidence, so we can say that $\epsilon_{xx} = \epsilon_{yy} = \epsilon$. For more ordered structures, however, ϵ_{xx} may not be the same as ϵ_{yy} due to a lack of symmetry in the material's structure. This can result in waves of different polarizations experiencing different permittivities (and so refractive indices), a phenomenon known as birefringence. Having $\epsilon_{xx} \neq \epsilon_{yy}$ can also allow us to access the ϵ_{xy} and ϵ_{yx} components of the constitutive matrix. Simply rotating the material off its x-y-z basis will result in non-zero ϵ_{xy} and ϵ_{yx} .

Permeability is the equivalent quantity describing how a magnetic field behaves in a material and can be understood by considering diamagnetism and paramagnetism. A magnetic field in

a dielectric material can produce opposing fields (diamagnetism) through a quantum mechanical effect called Langevin diamagnetism, in which the applied magnetic field induces a precession of electrons around the nucleus of the atoms and so an opposing magnetic field. The equivalent theory for metals is called Landau diamagnetism and involves a similar argument about electrons responding to the external field, though this time in the context of unbound electrons flowing within the metal's crystal lattice. Diamagnetism in materials will create a magnetic polarization (\mathbf{M}) which opposes that of the applied field (\mathbf{H}) and so will result in a relative permeability which is slightly less than one. Examples of materials that exhibit this phenomenon are bismuth, which has $\mu_r - 1 = -1.66 \times 10^{-4}$, and pyrolytic graphite (a more disordered version of graphene) which has $\mu_r - 1 = -4.09 \times 10^{-4}$ [6]. Conductors can also exhibit macroscopic, dynamic form of Landau diamagnetism by forming current loops within their bulk to oppose the incident magnetic fields. This effect is responsible for the famous demonstration where a magnet slows down when it is dropped through a metal pipe. A set of materials which act similarly to diamagnets (although are not technically classified as such) are superconductors. This is due to the Meisner effect, where a superconductor expels magnetic fields from its interior, meaning that they have a relative permeability of exactly zero. This property has been studied for use in very low frequency metamaterials [7], as designing magnetic resonant elements for very low frequencies is difficult without resorting to very large structures.

Paramagnetism may be considered a counterpart to diamagnetism, as it is also reliant on electrons but this time the effect is attractive. This is due to unpaired electrons in the shells of atoms; any unpaired electron (i.e. an electron which is not paired with an electron of opposite spin) has a net magnetic moment, which allows it to act as a small magnetic dipole which will

try to align with any applied magnetic field. The magnitude of this effect on the relative permeability is approximately equivalent to that of the diamagnetic examples earlier. For example: uranium has $\mu_r - 1 = 4 \times 10^{-4}$ and iron oxide (FeO) has $\mu_r - 1 = 7.2 \times 10^{-3}$ [6]. In some materials, a process known as the exchange interaction (related to the Pauli exclusion principle) encourages the magnetic dipoles in paramagnetic atoms to align with each other and form magnetic domains which themselves act as stronger magnetic dipoles. This is known as ferromagnetism and is responsible for the permanent magnets that we use in technologies today (e.g. fridge magnets or hard disk drives). Although this effect can be very strong, Metglas claim that their 2714A Magnetic Alloy can have a relative permeability of up to 1,000,000 for very low frequencies [8], it is only of relevance to DC or low frequency fields, where the domains have sufficient time to align with the alternating field.

Though there are many ways in which a material can exhibit a magnetic response, macroscopic diamagnetism through induced currents is by far the most useful in metamaterials, as it can occur at high frequencies and can be enhanced with specially designed structures to such an extent that a negative permeability is possible.

There can also be coupling between the electric and magnetic responses, where an electric field can induce a magnetisation and a magnetic field can induce a polarizability. Materials which have this cross coupling can be roughly separated into two categories: chiral and bianisotropic. Chiral metamaterials are materials which have non-zero values of ζ_{xx} , ζ_{yy} , ξ_{xx} and ξ_{yy} in their constitutive matrices, meaning that electric fields can induce a magnetisation parallel to the applied field and a magnetic field can induce a polarizability parallel to the applied field. There are some molecules, such as sucrose, which are naturally

chiral and can exhibit chiral behaviour, such as the rotation of the polarization of a wave in either crystals or solutions of these molecules [9]. Bianisotropic materials are similar to chiral materials in that an electric/magnetic field can result in a magnetisation/polarizability but in this case the direction of magnetisation is perpendicular to the applied electric field. They can be identified by having non-zero values for ζ_{xy} , ζ_{yx} , ξ_{xy} and ξ_{yx} . Now that we know more about the material parameters of a unit cell, we will discuss the literature on metamaterials and show what kind of properties have been realised so far.

2.2. Properties of Metamaterials:

Metamaterials are periodic arrays of sub-wavelength, artificial unit cells that can exhibit behaviour not seen in natural materials, such as high frequency magnetic response [10] and negative refraction [4]. Although they are a relatively new concept (one could argue that the field officially started when Pendry et al. [10] predicted an artificial magnetic response from appropriately shaped conductors in 1999), the practice of making artificially enhanced optical materials has been around for a long time. Perhaps the most famous historical example of an artificial optical material is the Lycurgus cup, which can be seen in Figure 2 c). This has the intriguing property that it appears to change colour when the direction of illumination is changed (left panel of Figure 2 (c) shows illumination from the front and the right panel shows illumination from the back). This is due to large frequency dispersion in the medium, whereby shorter wavelengths of light (blue/green) are reflected more than longer wavelengths (red). This can be understood by Drude permittivity model and the formation of surface plasmon polaritons (SPPs). For low frequencies, the Drude model predicts large, positive imaginary part

and a large, negative real part for the permittivity. As the frequency increases, the real part will increase and the imaginary part will decrease. Just below the plasma frequency (where $Re(\epsilon_r) = 0$), the real part of the permittivity will be small and negative. This is the region where SPPs can exist, as they require that the negative (real) permittivity of the metal approximately cancel out the positive (real) permittivity of the surrounding dielectric. SPPs are highly localized, propagating waves which are bound to the interface between a metal and a dielectric. The electric field and charge distribution of a SPP on a flat surface is depicted in Figure 2 (a), where we can see the electric field and the associated spatial oscillation of charge in the metal. The strength of the electric field decays exponentially away from the interface between the dielectric and metal, which can be seen in Figure 2 (b), showing the highly localised nature of the wave.

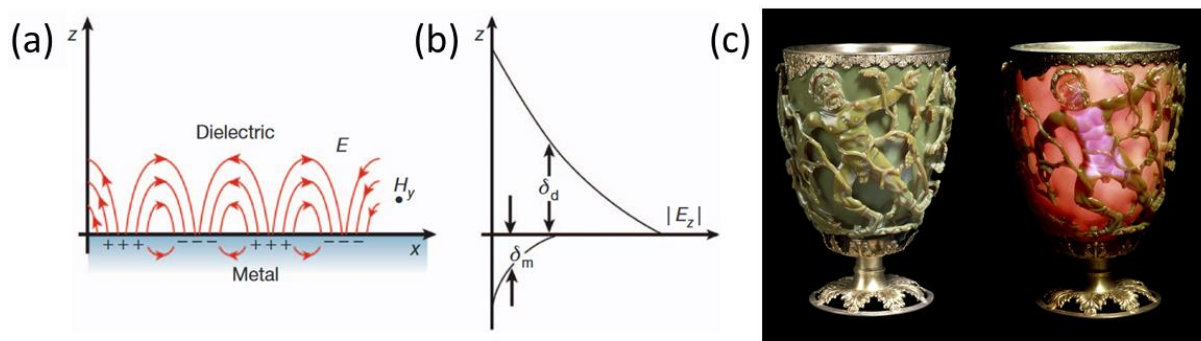


Figure 2: Surface plasmons and the Lycurgus cup. (a) shows a graph of the electric field (red lines) and charge (+/- signs) distribution for a surface plasmon travelling in the x direction and (b) shows the intensity of the z component of the electric field as a function of the distance from the metal-dielectric interface (both are taken from [13]). The Lycurgus cup (courtesy of the British Museum © The Trustees of the British Museum) is shown in (c), where the left-hand side shows the cup illuminated from the front and the right-hand side shows it illuminated from the back.

These SPPs lead to highly concentrated field distributions around the metal nanoparticles at certain frequencies which leads to dispersive scattering behaviour below the plasma frequency. As most metals have plasma frequencies in the ultraviolet range, this allows metal nanoparticles (under the right conditions) to have high dispersion in the visible frequency

range. This is what gives the Lycurgus cup its unusual optical properties and it was achieved by adding a mixture of silver and gold to the molten glass mixture (along with a trace of copper) and then heat treating the glass to create metallic nanoparticles [11]. Another common example of this is stained glass, which uses a variety of metals or metal salts to achieve a similar effect [12].

Modern metamaterials, due to their tuneable electromagnetic properties and sub-wavelength size, enable a great deal of control over the strength and spatial variation of bulk material properties such as the refractive index, $n(\mathbf{r})$ (where, for non-bianisotropic media, $n(\mathbf{r}) = \sqrt{\epsilon_r(\mathbf{r})\mu_r(\mathbf{r})}$). This allows gradient index devices, such as cloaks [3,14-16] and lenses [17-19] to be designed with relative ease. These gradient index devices work on the principle that a spatially varying refractive index can be used to redirect light rays, one can either see this as being the result of a kind of potential force, where the gradient of the refractive index is proportional to the 'bending force', or as a result of a compression/expansion transformation on the space, similar to how gravity is viewed in the General Theory of Relativity. This transformation optics approach is very popular in cloak design as it allows for a direct translation of a coordinate transformation into a material potential. For example, the designers of the carpet cloak in Figure 3 (a) used a quasi-conformal coordinate map to generate their index profile. The advantage of making lenses using metamaterials rather than a more standard dielectric like glass is that a metamaterial lens can be flat, with no variation in thickness necessary to achieve the difference in optical path length (unlike a conventional dielectric lens).

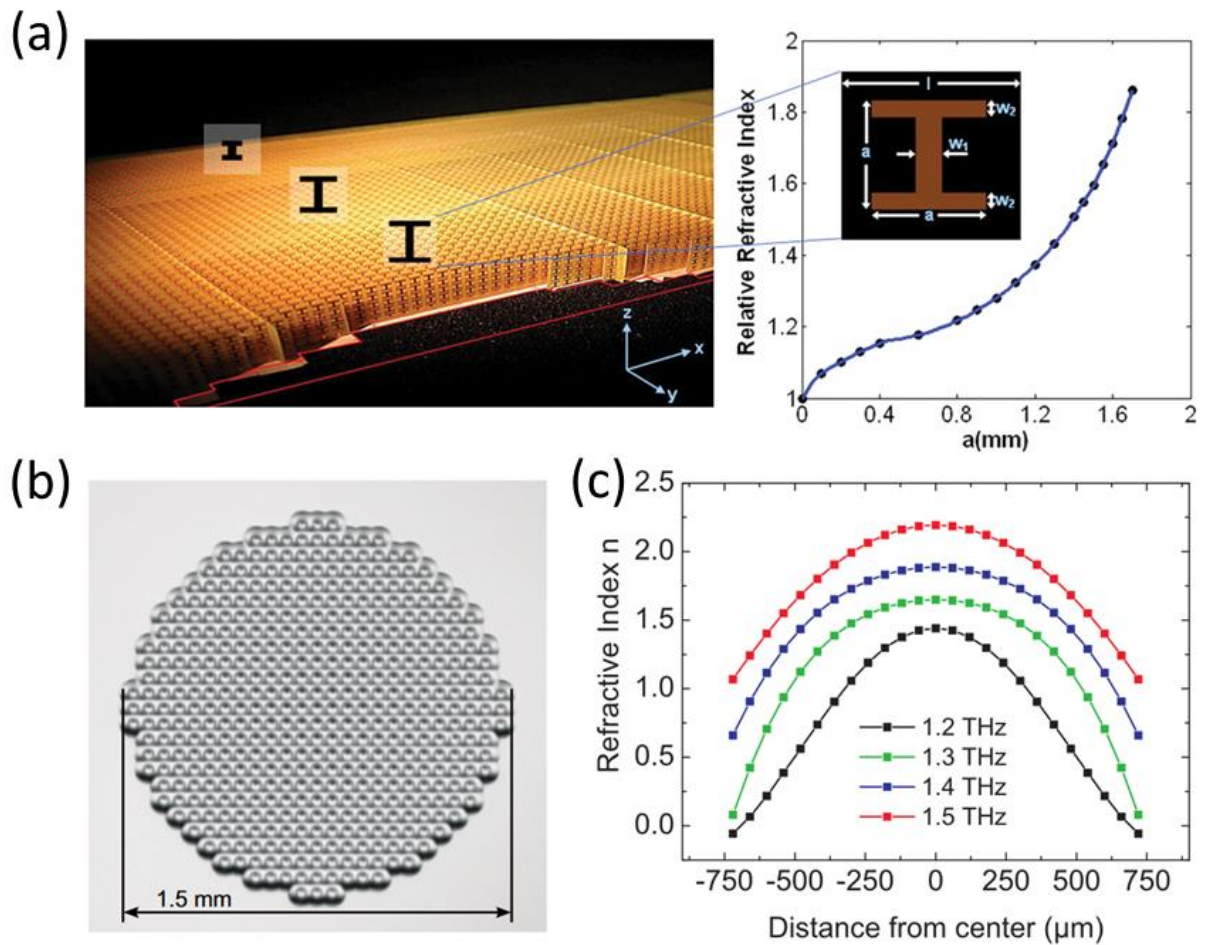


Figure 3: Two examples of gradient index devices. (a) shows a microwave gradient index carpet cloak where the cloaked area is indicated by the red line. A schematic of the unit cell is also shown along with a graph of the effective index of the unit cell as a function of the geometry parameter a [14]. (b) is a picture of a terahertz gradient index lens formed of annular slots of varying radii (from $23\mu\text{m}$ in the centre to $18\mu\text{m}$ near the edge) [17]. (c) shows the spatial variation of the refractive index of the lens for several frequencies.

Perhaps the most famous application of metamaterials, and an area of intense investigation, has been to develop media exhibiting a negative refractive index [4,20-25]. Negative index media (NIMs) have many interesting properties, such as negative refraction. This is a consequence of using Snell's law with negative refractive indices where the refraction angle of a ray inside the medium is negative, and left handedness: the property that the electric field, magnetic field and \mathbf{k} vector form a left-handed set and so the \mathbf{k} vector is anti-parallel to the Poynting flow and the wave appears to be accumulating negative phase. Identifying a

negative index medium from its ϵ and μ is not as simple as saying $Re(\epsilon_r) < 0$ and $Re(\mu_r) < 0$ as we have a square root sign to consider. Depine et al. [26] proved that in order to get a negative phase velocity and positive power transfer (i.e. a left handed medium) then we must have.

$$Re(\epsilon_r)|\mu_r| + Re(\mu_r)|\epsilon_r| < 0 \quad (2.9)$$

One intriguing application of negative refraction is to make perfect lenses; lenses that perfectly reform the wavefront on the other side of the lens and are not hindered by the diffraction limit, meaning that, theoretically, they could image objects much smaller than the wavelength of the light used to probe the structure [27-33].

This subwavelength imaging property is due to the behaviour of evanescent waves in NIMs. Evanescent waves are electromagnetic fields generated in a scattering process that are not travelling waves but localised, exponentially decaying waves, similar to the reactive nearfield in the vicinity of an antenna. These fields can contain information about an object that is not obtainable through standard microscopy due to the diffraction limit. In vacuum (or air), evanescent fields decay exponentially with distance from the source and so are not of much use in conventional microscopy. In a NIM, however, evanescent waves are exponentially amplified (see Figure 4 (b)), so an imaging system with a NIM lens would be able to recover this nearfield information.

Negative index lenses can be seen as exploiting a certain symmetry in material potentials, where (for a lossless system) the refractive index has an antisymmetric profile: $n(z) = -n(-z)$. Materials which have this symmetry are more commonly known as complementary media.

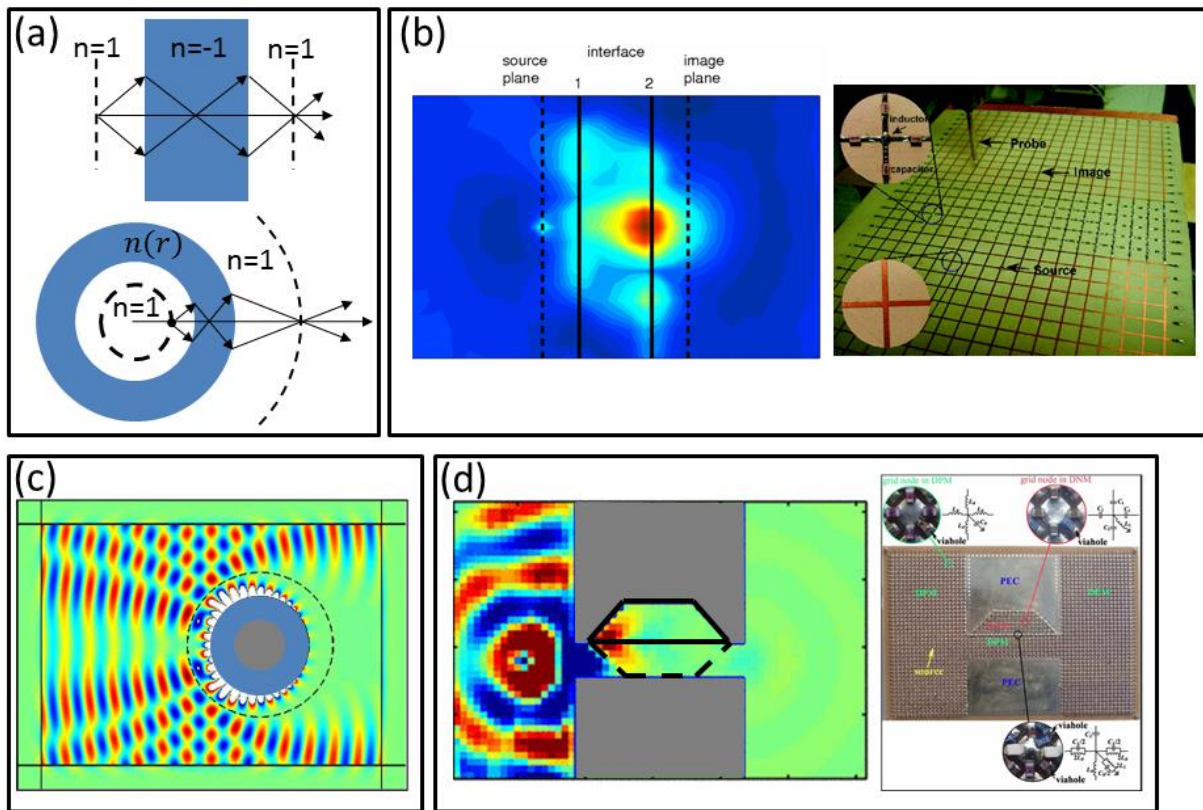


Figure 4: Examples of complementary media. (a) A homogeneous slab of $n = -1$ (blue color) compensates the same thickness of freespace around it with perfect information transport. A cylindrical ring of with a transformed material profile has similar properties, illustrated by the rays from a point source to its image. Source and image planes are denoted by the dashed lines. (b) Super-resolution from a negative index lens (measured field with sample picture on the right hand side) using a grid of transmission lines with connected capacitors and inductors [32]. (c) Superscatterer [34]: a negative index medium (blue) is wrapped around a perfect electric conductor (PEC) cylinder (gray) to mimic a larger PEC cylinder with the dashed line as its outer boundary. (d) An invisible gateway using a transmission line network [38]. The negative index medium (blue trapezoidal area) compensates the freespace (in black dashed line) and hence blocks the open channel between the two blocks of PEC (gray). Color maps show the measured field distribution with sample shown on the right.

Figure 4 shows examples of systems which utilise this antisymmetry. NIM lenses are shown in a), where the balance between the NIM ($n = -1$) and the surrounding medium ($n = 1$) means that a point source on the first dashed boundary is then imaged to the other dashed boundary, as can be seen from the ray traces. The information transfer for this ideal case is perfect, as if the left and right dashed lines are just the same line. This super-resolution ability has been experimentally verified using a transmission line system. Figure 4 (b) shows the measured field profile at a frequency around 1GHz when a transmission-line network of capacitors and

inductors are used to mimic the region of free-space and the region of complementary medium [33]. A bright spot at the image plane was found as small as 0.21 wavelengths, which is beyond the conventional diffraction limit. This anti-symmetric material profile matching can be carried to cylindrical symmetric systems through a coordinate transformation $x' + iy' = \ln(x + iy)$ (see lower part of Figure 4 (a)), though the coordinate transformation imposes limits on the imaging properties: objects outside the cylinder must be within a certain distance of the outer radius to form an image inside the cylinder and objects inside the cylinder must be a certain distance from the centre to form an image outside the cylinder. The material

potential in this case is $[\epsilon_r] = [\mu_r] = \begin{pmatrix} -1 & 0 & 0 \\ 0 & -1 & 0 \\ 0 & 0 & -r^{-2} \end{pmatrix}$, where the dependence on the

radius is due to the coordinate transformation. In a cylindrical system, a ring of negative index material (blue) can be used to compensate a ring of freespace in a similar manner to the cartesian perfect lens. This can also be used to construct a so-called superscatterer [34], shown in Figure 4 (c). The negative index material effectively magnifies the PEC cylinder (grey in colour) to a larger radius (the dashed black line), casting a bigger shadow for plane wave incidence shown in the simulation as an illusion effect [35-37]. Figure 4 (d) shows an interesting realization of an invisible gateway, again using transmission line analogy [38]. The system consists of different regions corresponding to a wave propagation channel (a gap) between two PEC blocks except that a trapezoidal region on one side of the block (the region inside the solid, black line) is replaced by a NIM, which cancels the dashed line region of freespace within the channel. As the NIM region is surrounded by PEC, this effectively extends the PEC to the boundaries of the cancelled region. As a result, no waves are allowed to go through the apparently open channel.

As we stated earlier, we can have materials which have cross-coupling between the electric and magnetic fields. One of the two main classes of such materials are chiral (or bi-isotropic) materials, which can rotate the polarization of a wave (optical activity) and have different responses for left and right circularly polarized light [2,39-44].

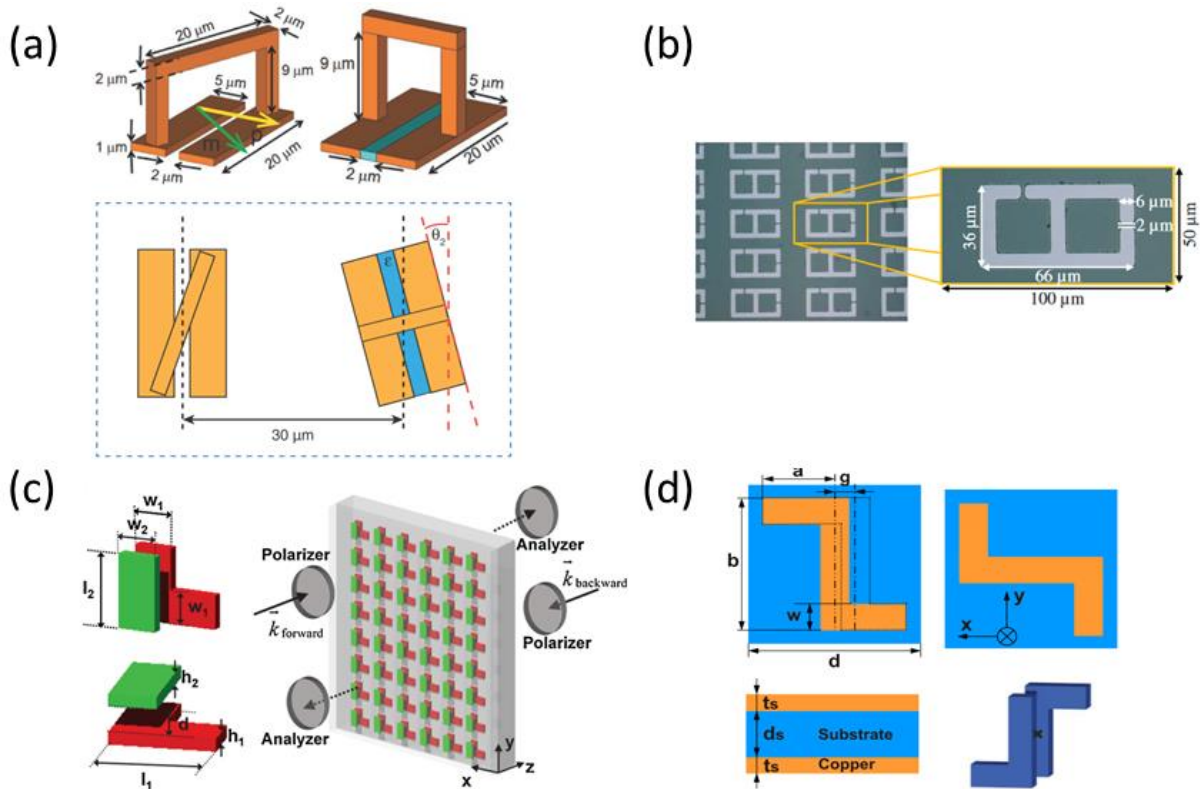


Figure 5: Examples of various chiral metamaterial unit cells. (a) shows a unit cell of a chiral metasurface consisting of a chiral component and an achiral component. This structure shows asymmetric linear polarization conversion in the terahertz region [39]. (b) shows a chiral metasurface designed to give asymmetric circular polarization conversion in the terahertz region [40]. (c) shows the unit cell and measurement configuration of a chiral metasurface designed to give asymmetric circular polarization conversion in the near infrared region [43]. (d) Shows another metasurface designed for asymmetric linear polarization conversion, this time in the microwave region [44].

Examples of chiral metamaterials can be seen in Figure 5, with references in the caption. These are structures designed to give asymmetric polarization conversion for linear ((a) and (d)) or circular ((b) and (c)) polarized light. In (a), chiral and achiral (i.e. symmetric) components are combined to give a metasurface which has different y to x linear polarization conversion

coefficients when illuminated from above or below by a 1.75 THz wave. In (b) we see an aluminium structure placed on a n-doped silicon substrate which exhibits asymmetric circular polarization conversion in the region of 0.4-1.2 THz (i.e. conversion of LCP→RCP is not the same as RCP→LCP). Additionally, a chirality-induced negative refractive index was observed for some modes. In (c) we see another chiral metasurface designed to give asymmetric circular polarization conversion, this time in the 200-300 THz region. In (d) we have another structure designed to give asymmetric linear polarization conversion, though this time in the microwave region (at 14.25 GHz) and care was taken to reduce the circular conversion by aligning the axes of the two arms (i.e. setting the g parameter in the first panel to zero).

The other main, though less popular, class of metamaterials with cross-coupling between their electric and magnetic responses are bianisotropic materials [45-48]. These materials can be used for tuning reflection phase [46], can result in negative refractive index [47] and have been proposed as an attractive alternative to optical NIMs based on permittivity and permeability resonances (due to the difficulty in obtaining significant magnetic response at optical frequencies) [48]. Bianisotropy can also result in a negative refractive index because it modifies the index so that it is given $n_i^2 = \epsilon_{ii}\mu_{jj} + \xi_{ij}\zeta_{ji}$, where $(i, j) = (x, y)$ or (y, x) . For reciprocal systems (see section 3.5.5) we have $\xi_{ij} = -\zeta_{ji}$, so if we have very strong bianisotropy we can have a negative refractive index without needing ϵ or μ to be as negative. Examples of these structures are shown in Figure 6, where (a) shows a microwave design (total thickness is approximately 32mm) where the bianisotropy comes from the tilt of the Ω shapes [48] and (b) shows a THz design, where the bianisotropy is generated from the offset of the two lattices [47].

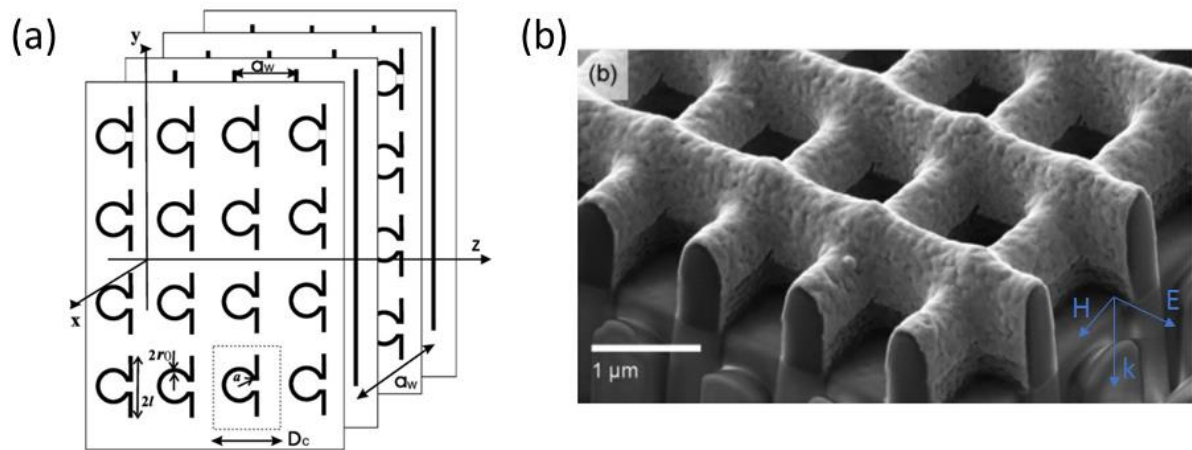


Figure 6: Examples of bianisotropic metamaterials. (a) shows a bianisotropic metamaterial composed of layers of Ω resonators and wires, designed to give a negative refractive index (propagation is in the z -direction) [48]. The bianisotropy comes from the tilt of the Ω shapes. (b) shows a fishnet microstructure which generates bianisotropy from the offset of its two lattices (i.e. it is not symmetric in the propagation direction) [47].

Both chirality and bianisotropy are a result of non-symmetric unit cells. Bianisotropic metamaterials are generally non-symmetric in the propagation direction and chiral metamaterials lack symmetry in all three spatial dimensions (discussion on the effects of spatial symmetry can be found in section 3.3).

Although they have the ability to give us a vast array of material parameters, metamaterials are not without their limitations. They cannot give arbitrary material profiles in frequency space, as their frequency dependence must still obey the Kramers-Kronig (K-K) relations. These are a set of relations resulting from causality, the idea that the systems response cannot occur before the excitation. In electromagnetism, this is equivalent to saying that the response fields (D and B) cannot occur before the incident fields (E and H). Enforcing this condition leads to a relation between the real and imaginary parts of the permittivity (or permeability), that they are Hilbert transforms of each other:

$$\begin{aligned}
\text{Re}(\epsilon_r(\omega)) &= 1 + \frac{1}{\pi} P \int_{-\infty}^{\infty} \frac{\text{Im}(\epsilon_r(\omega'))}{\omega' - \omega} d\omega' \\
\text{Im}(\epsilon_r(\omega)) &= -\frac{1}{\pi} P \int_{-\infty}^{\infty} \frac{\text{Re}(\epsilon_r(\omega')) - 1}{\omega' - \omega} d\omega',
\end{aligned} \tag{2.10}$$

where P indicates the Cauchy principle value of the integral. A consequence of these relations is that forcing the real part of the refractive index of a material to be constant over some bandwidth will increase the imaginary part of the index (i.e. the loss) within that bandwidth and so reduce the effectiveness of the material in lensing or other applications [49].

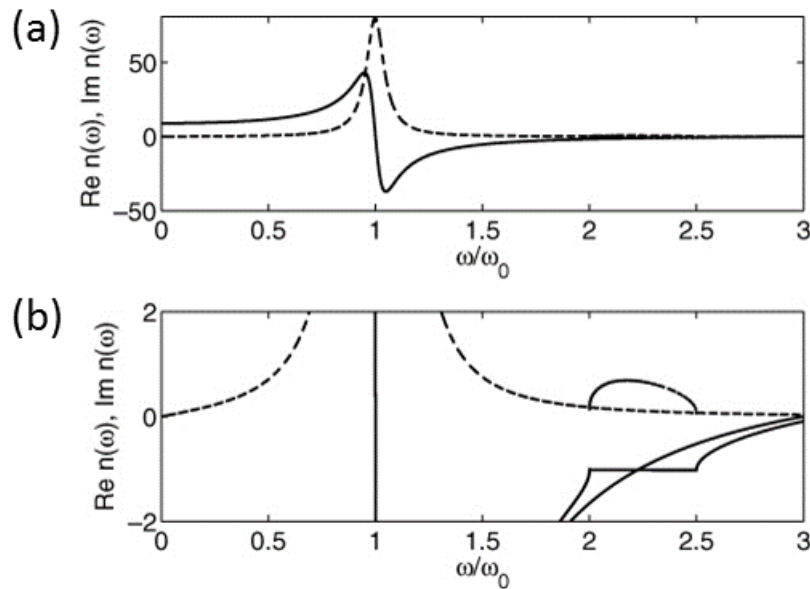


Figure 7: The effect of the Kramers-Kronig relations on enforced non-dispersivity. (a) shows the real (solid line) and imaginary (dashed line) of the refractive index ($n(\omega)$) of a medium containing two, coinciding electric and magnetic Lorentzian resonances (see next section). (b) shows the effect of enforcing non-dispersivity in the scaled frequency region 2-2.5. We can see that setting the real part of $n(\omega)$ to be constant in this region will (due to the Kramers-Kronig relations) increase the imaginary part of $n(\omega)$ and so make the medium more lossy. From [49].

This is depicted in Figure 7, where the authors show that enforcing $\text{Re}[n] = -1$ in a certain region for a given refractive index (shown in (a)) will automatically increase the imaginary part of n (i.e. the loss), as can be seen by the bump in the imaginary part of the index in (b). Another related problem is intrinsic ohmic losses: all metals exhibit some resistive losses due to their

imperfect lattices and this, coupled with the lossy surface plasmon polariton (SPP) propagation effects at optical and terahertz frequencies [50,51], can significantly impair the performance of metamaterial devices at higher frequencies.

Another limitation of metamaterials is that they are often highly dispersive, meaning that the functionality of devices is restricted to a narrow bandwidth around the designed operating frequency. This severely limits their applicability to cloaking technology [52], where broadband behaviour is vital, and communications, as highly dispersive media will deform the pulses used to transmit data. Metamaterials can be designed to have broadband functionality but, as with antennas, this is usually at the cost of performance [53].

Although the restrictions of the K-K relations and dispersion are very difficult to tackle, the issue of ohmic loss has a more obvious solution: gain. There are two main ways to do this; one which has gathered a lot of attention in the optical metamaterial community involves replacing part or all of the substrate of the metamaterial with a dye-embedded dielectric [54-57], i.e. a 3 level system that can be pumped into a high energy state and then relax down into its ground state by either spontaneous or stimulated emission. Due to the high field concentrations associated with resonant structures in optical metamaterials, the gain achieved from these dye-nanostructure composites can be much higher than that achieved with just the dye. However, this has the drawback that stimulated emission, by its very nature, is frequency-selective, meaning broadband applications are difficult to achieve. Another method, applicable to GHz metamaterials, is to incorporate nonlinear, negative differential resistance devices, such as tunnel diodes or resonant tunnelling diodes into the structure [58-60]. These are very thin, highly doped p-n junction semiconductor devices which can allow

electrons to tunnel through them when a bias voltage is applied. When supplied with a suitable bias voltage these devices can exhibit a negative differential resistance, which can amplify AC signals and so provide gain (more details, along with measurements of a tunnel diode can be found in section 6.2).

2.3. Oscillating electrons and the Lorentz model:

In order to use metamaterials as a platform for constructing potentials, we must try to obtain a microscopic model to describe their behaviour. As we saw in the previous section, the electromagnetic properties of materials are dominated by the motions of electrons under an applied field. These electrons can be in an electron shell, bound to a molecule or, in the case of metamaterials, in a resonating structure. If we assume that the amplitude and energy (i.e. frequency) of the incident field is relatively small, so that we don't have to worry about ionisation or photoelectric emission, then we can model this behaviour by considering an electron oscillating under an externally applied field about a fixed point with a linear restoring force acting to keep it in place and a loss term proportional to the velocity of the particle. This is similar to a damped, forced harmonic oscillator and is known as the Lorentz model. The equation of motion for the electron around its equilibrium point is given by:

$$m \frac{d^2 \mathbf{r}}{dt^2} + m\gamma \frac{d\mathbf{r}}{dt} + m\omega_r^2 \mathbf{r} = -e\mathbf{E}_{inc} \quad (2.11)$$

where \mathbf{r} is the position vector of the electron (centred on its equilibrium point), m is the electron mass (or effective mass if the electron is bound to a lattice), γ is a resistance term to model losses, $m\omega_r^2 \mathbf{r}$ is the restoring force, e is the electron charge and \mathbf{E}_{inc} is the incident

electric field. In an atom or molecule, the restoring force is the bonding between the electron and its atom or molecular structure. In a resonator, however, the restoring force comes from the compressibility of the electron fluid when confined to a conducting structure. If we then make the assumption that both the incident electric field and the position vector have a time harmonic dependence (i.e. $\mathbf{r} = \mathbf{r}(\omega)e^{-i\omega t}$ and $\mathbf{E}_{inc} = \mathbf{E}_0e^{-i\omega t}$), our equation then becomes:

$$-m\omega^2\mathbf{r}(\omega) - im\gamma\omega\mathbf{r}(\omega) + m\omega_r^2\mathbf{r}(\omega) = -e\mathbf{E}_0 \quad (2.12)$$

which we can rearrange into

$$\mathbf{r}(\omega) = -\frac{e}{m} \frac{\mathbf{E}_0}{\omega_r^2 - \omega^2 - i\gamma\omega} \quad (2.13)$$

From this position vector, we can get the electric dipole moment of the oscillator: $\boldsymbol{\mu}(\omega) = q\mathbf{r}(\omega)$ and from this we can get the polarizability: $\boldsymbol{\mu}(\omega) = \alpha(\omega)\mathbf{E}_0$. To get the bulk material parameters for the medium, we need to consider the polarization per unit volume and so the density of oscillating electrons. We denote this density as N and note that the polarization per unit volume is given by $\mathbf{P}(\omega) = N\alpha(\omega)\mathbf{E}_0$, which we can relate the susceptibility (χ) to by $\mathbf{P}(\omega) = \epsilon_0\chi(\omega)\mathbf{E}_0$. By recognizing that $\mathbf{D}(\omega) = \epsilon_0\mathbf{E}_0 + \mathbf{P}(\omega) = \epsilon_0\epsilon_r(\omega)\mathbf{E}_0$, we can finally get an equation for the relative permittivity:

$$\epsilon_r(\omega) = 1 + \frac{\omega_p^2}{\omega_r^2 - \omega^2 - i\gamma\omega} \quad (2.14)$$

where $\omega_p^2 = Ne^2/\epsilon_0m$. The special case where $\omega_r \rightarrow 0$ is known as the Drude model and is a popular model for the permittivity of bulk metals. If we have multiple (N), independent resonators in our medium then the permittivity is given by a sum of them:

$$\epsilon_r(\omega) = 1 + \sum_{j=1}^N \frac{f_j \omega_{pj}^2}{\omega_{rj}^2 - \omega^2 - i\gamma_j \omega} \quad (2.15)$$

where f_j is the relative strength of the oscillator ($\sum_{j=1}^n f_j = 1$).

To examine the properties of this function, it is useful to split it up into real and imaginary parts:

$$\epsilon_r(\omega) = 1 + \frac{\omega_p^2(\omega_r^2 - \omega^2)}{(\omega_r^2 - \omega^2)^2 + \omega^2\gamma^2} + i \frac{\omega_p^2\omega\gamma}{(\omega_r^2 - \omega^2)^2 + \omega^2\gamma^2} \quad (2.16)$$

From this, we can extract some information about its behaviour at certain points. When $\omega \rightarrow 0$ (i.e. DC), we have $\epsilon_r \rightarrow 1 + \frac{\omega_p^2}{\omega_r^2} + 0i$. When $\omega \rightarrow \omega_r$, we have $\epsilon_r \rightarrow 1 + \frac{\omega_p^2}{\omega_r\gamma} i$. When $\omega \rightarrow \infty$, we have $\epsilon_r \rightarrow 1 + 0i$. Figure 8 shows the real and imaginary parts of ϵ_r for $\omega_p = 5 \times 10^9 \text{ rad/s}$, $\gamma = 5 \times 10^8 \text{ rad/s}$ and $\omega_r = 5 \times 10^9 \text{ rad/s}$, where the points of interest are marked.

The three parameters involved in this function determine what values it can take. The resonating frequency, ω_r , determines the frequency about which the variation in ϵ occurs. The plasma frequency, ω_p , determines the magnitude of the resonance and is key to obtaining negative values. Lastly, the damping term γ , sometimes called the linewidth, determines the strength and breadth of the resonance (i.e. lower γ means a stronger, narrower resonance). In order to get a negative ϵ_r after the resonant frequency, the plasma frequency must satisfy $\omega_p^2 > \gamma^2 + 2\gamma\omega_r$. From this, we can see that using resonances can enable us to have materials with both positive and negative real parts of the permittivity (depending on the excitation frequency) if we can achieve the right resonance parameters.

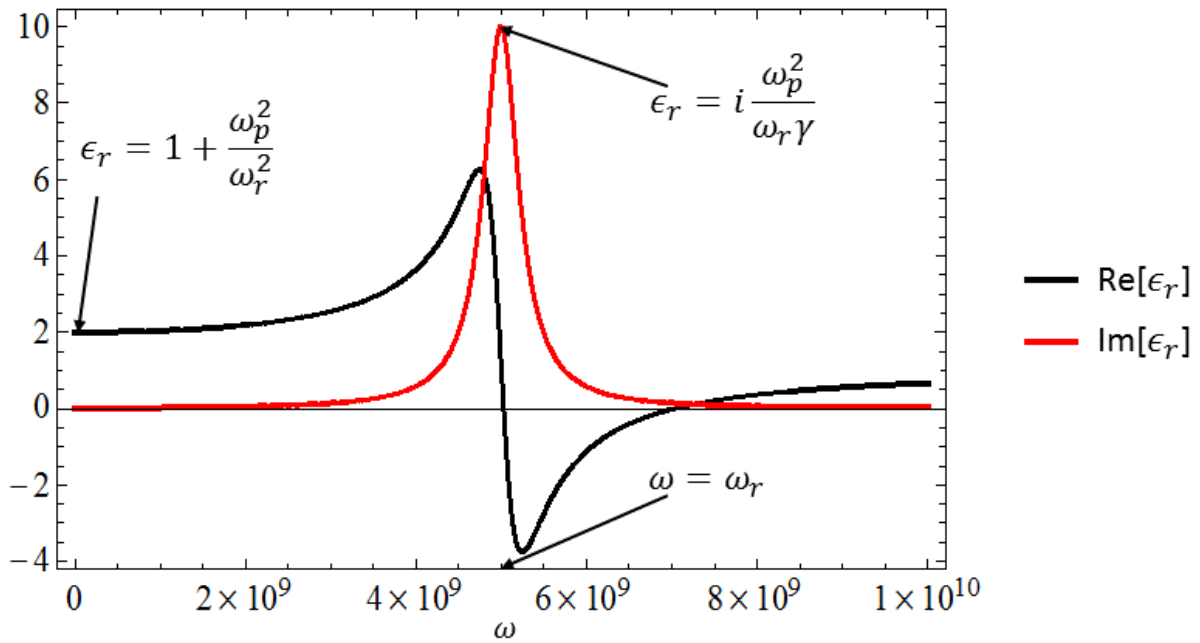


Figure 8: A plot of the real (black line) and imaginary (red line) parts of the permittivity given by the Lorentz oscillator model. Where $\omega_p = 5 \times 10^9 \text{ rad/s}$, $\gamma = 5 \times 10^8 \text{ rad/s}$, $\omega_r = 5 \times 10^9 \text{ rad/s}$. Values of interest are labelled.

The Lorentz model for a magnetic resonance is essentially the same as that of the electric resonance, though there is some disagreement in the literature about the exact form of the permeability of a magnetic resonator (usually a split ring resonator). Most agree that the permeability around a single resonance has the form

$$\mu_r(\omega) = 1 + \frac{F\omega_p^2}{\omega_r^2 - \omega^2 - i\gamma\omega} \quad (2.17)$$

But some sources have $F = F_0\omega^2$ [61-63] whereas others leave it as a constant which can be absorbed into ω_p [64,65]. This discrepancy comes from the methods and assumptions used to derive the equation. Those who use $F = \text{constant}$ treat the magnetisation of the medium exactly as one would treat the polarizability, meaning that we can swap the polarization, $\mathbf{P}(\omega)$, in the above derivation for the magnetization, $\mathbf{M}(\omega)$, and obtain a model which is identical in form to that of $\epsilon_r(\omega)$. Those who use $F = F_0\omega^2$ derive their model by assuming

that the structure can be modelled as a series RLC circuit, with the current in the resonator being described by

$$L\ddot{J} + J/C + R\dot{J} = -\ddot{\phi} \quad (2.18)$$

Where J is the current and ϕ is the magnetic flux through the resonator. The ω^2 dependence then comes from the double time derivative of the magnetic flux. Both of these models can be used to fit extracted permeabilities but in the author's experience using $F = F_0\omega^2$ tends to lead to a better frequency fit for SRRs.

2.4. Artificial electric and magnetic resonating structures:

Now that we have seen the large range of constitutive parameters that can be achieved via resonances, we will look at how to design some electric and magnetic resonating structures. Based on the Lorentz model, we have three parameters to work with for designing a resonance: ω_p , γ and ω_r . As we saw in the previous section, ω_p is related to the density of resonating electrons and hence the density of resonators. γ is proportional to the resistivity of the material, so a resonator made of a highly conductive material like gold ($\sigma = 4.1 \times 10^6 S/m$) will have a much sharper resonance than an equivalent resonator made of a less conductive material like amorphous carbon ($\sigma \approx 2 \times 10^3 S/m$). ω_r is mainly a function of the geometry of the resonator and the permittivity of any substrates, though other factors such as lattice constant can also affect it. Determining some of the factors which affect the ω_r of a resonator will be the main focus of this section.

As an example, we will take one of the most basic electric resonance structures: a metallic bar of length L orientated in the x -direction, excited by an x -polarized wave. The fundamental

resonant frequency corresponds to when the magnetic field across the wire has two antinodes either end, i.e. when $f_c = c/\lambda_c = c/2L$, similar to the fundamental resonance in a cavity or a dipole antenna. If we also consider a supporting dielectric substrate, which the wires will be embedded into, then the resonance will still occur at our $\lambda = 2L$ condition but now the wavelength is the wavelength inside the substrate. So, if we have a dielectric substrate with a refractive index n_{sub} , then our resonant frequency will become $f_c = c/2n_{sub}L$. As the surface of the wire is effectively a PEC at frequencies lower than optical frequencies, the x component of the electric field will be zero along the surface of the wire. This leads to a huge build-up of the electric field near the ends of the wire, often more than a one-hundred-fold increase compared to the strength of the incoming field. We can see this in Figure 9, which shows the absolute value of the electric field when a 30mm bar, suspended in a dielectric with $\epsilon_r = 4$, (which has a resonant frequency of around 2.5 GHz) is excited by a plane wave. When the frequency of the exciting wave is far from the resonant frequency, e.g. 1 GHz as in Figure 9 (a), we see some build-up of the electric field at the ends of the bar. However, when the wave is oscillating at the resonant frequency of the structure, we see a huge build-up of electric field, over 160 times the incident field strength (Figure 9 (b)).

This field concentration effect can enhance any nonlinear properties of the substrate, making metamaterials an attractive platform to study nonlinear devices [10]. One may think that simply using very high index substrates would lead to very subwavelength metamaterials, but using high index substrates also increases the impedance mismatch between the metamaterial and the surrounding environment: reducing the amount of light able to interact with the resonator, thereby reducing its effectiveness.

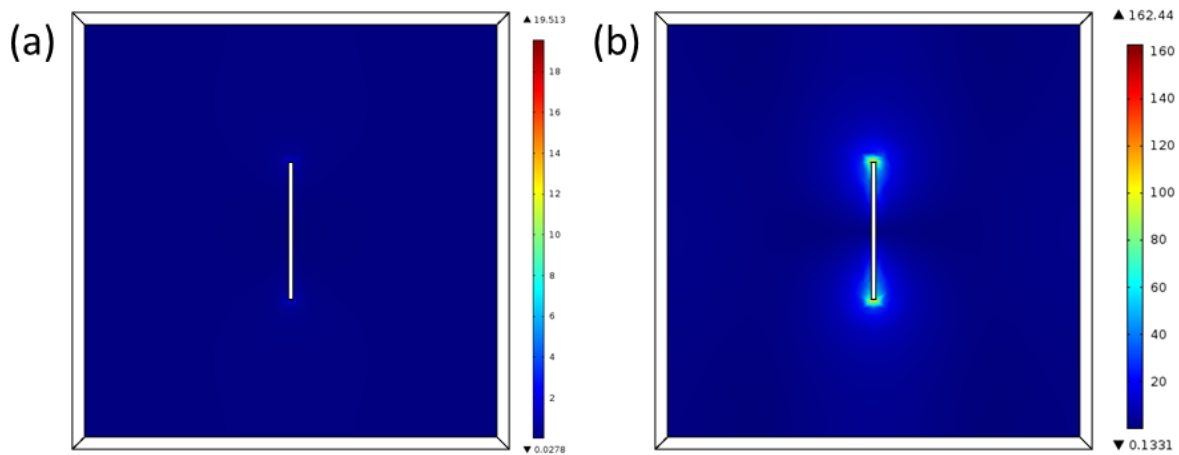


Figure 9: Simulated absolute value of the electric field around a bar resonator. A cross section of $|E|$ is shown for a 30mm bar oriented in the x direction, where (a) shows the field when the exciting wave oscillates at 1 GHz (max value $\sim 20\text{V/m}$) and (b) shows the field when the wave is oscillating at 2.5 GHz, close to the resonant frequency (max value $\sim 160\text{V/m}$). Strength of the incident field for both cases is set to unity and the incident wave polarisation is aligned with the bar (i.e. E_x polarisation). Simulated with COMSOL Multiphysics.

Another factor governing the resonating frequency of a metamaterial unit cell is its lattice constant. A single resonator on its own will resonate according to the cavity argument given above, however, when multiple resonators are placed in a lattice they can interact with each other through their scattered fields. This effect can either increase or decrease the resonant frequency of the metamaterial, depending on the phase elapsed between the resonators. This effect is demonstrated in Figure 10, where (a) shows the schematic of a metasurface consisting of 30mm metallic bars suspended in a dielectric medium with a relative permittivity of 4 (so $n_{sub} = 2$) and with a variable lattice constant b . Based on the previous cavity arguments, we expect the resonant frequency to be around 2.5 GHz. We start off with $b=90\text{mm}$, this means that the bars are approximately one and a half wavelengths apart if we measure from the centre of the bars. The real (solid line) and imaginary (dashed line) parts of the extracted, relative permittivity are shown in black in Figure 10 (b) and we can see that the

resonant frequency is approximately 2.53 GHz. Also shown in Figure 10 (b) are the relative permittivities for $b=80\text{mm}$ and $b=100\text{mm}$. For $b=80\text{mm}$ (shown in blue), we can see that the resonant frequency is blue shifted up to 2.6 GHz and for $b=100\text{mm}$ (shown in red), the resonant frequency is red shifted down to 2.44 GHz. The relationship between the resonance shift and the coupled waves can be explained via the dipolar model, which is discussed in appendix A. We can also see the effect of the lattice constant on ω_p (i.e. the strength of the resonance). ω_p is proportional to the density of the resonators and so should be inversely proportional to b^2 , which we can see evidence of when comparing the magnitudes of the resonances in Figure 10 (b). Due to the lattice constant sensitivity, it is often easier to set the lattice constant during the design process and then tune the geometry and substrate until the desired frequency profile is achieved.

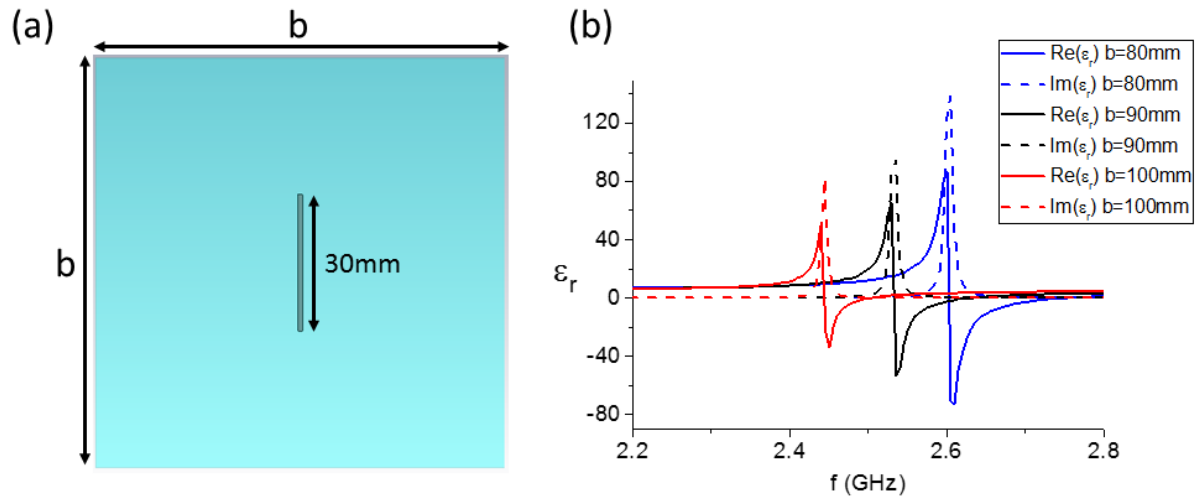


Figure 10: Dependence of ω_r on the lattice constant. (a) shows the unit cell of the metamaterial, where the grey bar is a PEC (dimensions $30 \times 1 \times 1\text{mm}$) and the blue square is the substrate into which the bar is embedded (dimensions $b \times b \times 4\text{mm}$). (b) shows the real (solid lines) and imaginary (dashed line) parts of the extracted permittivity. The colours indicate the value of b used, black is 90mm , red is 100mm and blue is 80mm .

We will now discuss the other building block of metamaterials: split ring resonators (SRRs).

We will start by considering a closed ring resonator (CRR) with a radius of 8mm . CRRs can

support a small diamagnetic response but no magnetic resonances. For example, if a ring is placed as in Figure 11 (a), with the incident field polarized as shown in the bottom left of the figure, then there will be electric resonances associated with cavity modes (similar to the wire) and a small magnetic response due to the circulation of current in the ring which is driven by the alternating magnetic field. The electric resonance for this occurs around 5 GHz, which is outside the $\phi_0 < 1$ region applicable to metamaterials and so we will not discuss it further. The CRR structure shown in Figure 11 (a) does not have a magnetic resonance but is slightly diamagnetic with $\mu_r \approx 0.9$, which can be seen from the real (black) part of μ_r in (d). It was found that making a slit in the ring could allow it to support subwavelength resonances and lead to a much stronger response. As we can see from the black and red lines in (e) (corresponding to the real and imaginary parts of μ for the split ring structure in (b)), adding a split in the ring (1mm in this case) allows the structure to support a low frequency resonance at 1.8 GHz.

Another important development for SRRs is the inclusion of a second smaller, concentric SRR within the first one. This has the effect of further increasing the capacitive effect and pushing the resonance down to even lower frequencies. We can see this in (d), where the real (blue) and imaginary (green) parts of μ_r for the concentric ring structure shown in (c) show a red shifting of the SRR resonance down to 0.94 GHz. This frequency corresponds to a wavelength of approximately 320mm, which is 16 times larger than the unit cell depth, making it good for metamaterial applications.

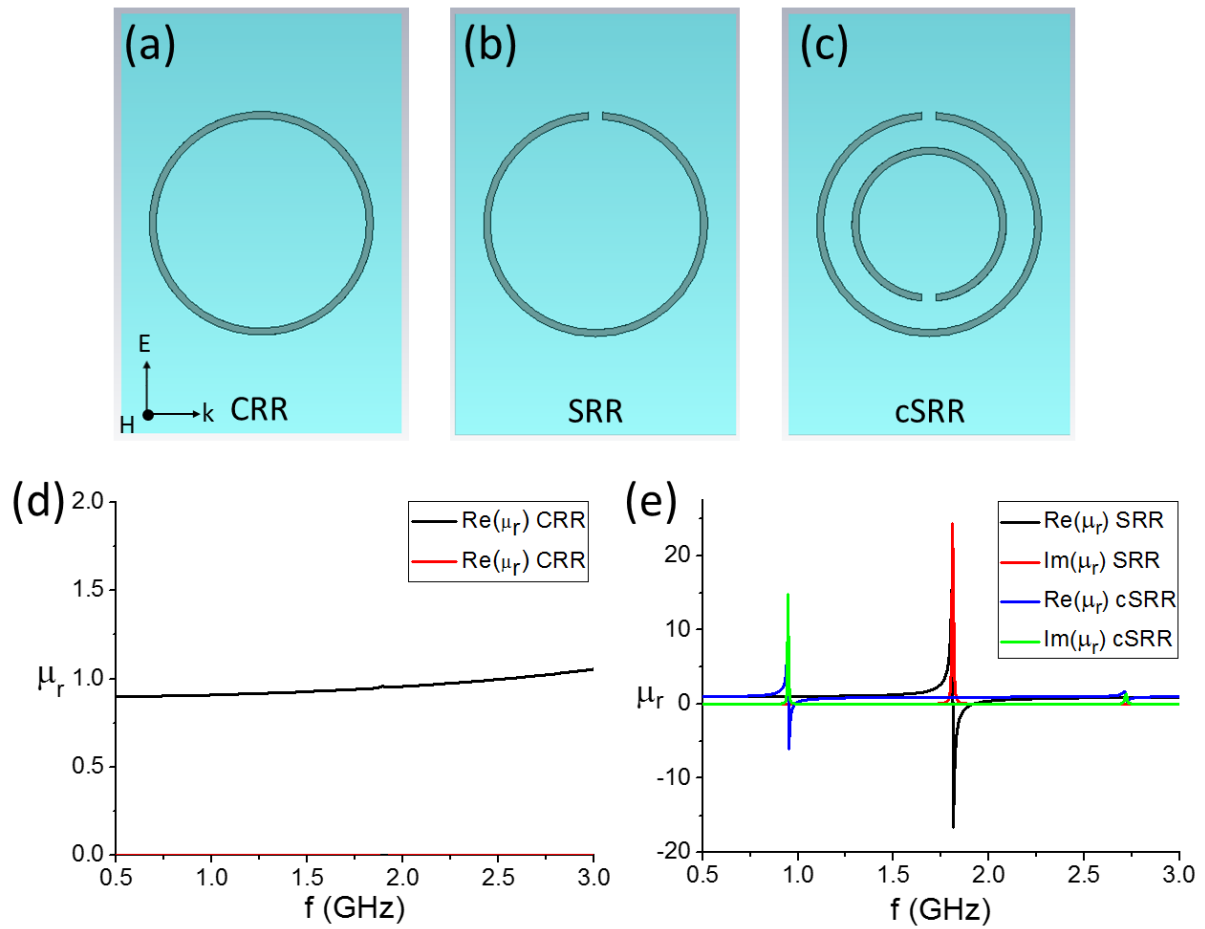


Figure 11: Comparison of a ring, split ring and concentric split ring resonator. (a), (b) and (c) show the CRR, SRR and cSRR structures. In each case the outer radius of the larger ring is 8mm and its width is 0.5mm, with the substrate being 20mm deep in the direction of propagation and 4mm wide. The direction and polarisation of the excitation wave are show in the bottom-left of (a). The gaps in the rings in (b) and (c) are all 1mm and for (c) the inner ring's outer radius is 5.5mm with a width of 0.5mm. (d) shows the real (black) and imaginary (red) parts of the extracted μ_r for the CRR. (e) shows the real (black and blue) and imaginary (red and green) parts of μ_r for the SRR and cSRR structures.

The design specifics of this kind of composite SRR are significantly more complicated than a simple wire or single SRR, so we will not go into much more detail here (for a detailed discussion see [66] or [67]). However, many of the guiding principles of the wire resonator are also applicable to the SRR: the resonant frequency is inversely proportional to the radius of the resonator, the resonant frequency is also inversely proportional to the refractive index of the substrate, and putting them in a lattice will generate coupling, the effect of which will vary with the ratio of the separation to the incident wavelength.

This knowledge of electric and magnetic resonances should allow us to construct a wide variety of potentials. As an example of this, we will design a negative refractive index material. For the refractive index to be negative, we require that equation 2.9 hold. An easy way to do this is to ensure that both the permittivity and permeability of the material are negative. We can achieve this by constructing a unit cell which has electric and magnetic resonances of a higher frequency than the desired operating frequency. Figure 12 (a) shows the unit cell of the designed metamaterial. The unit cell is 70mm in height, 80mm in width and 80mm in depth. The modified bar resonator has a total height of 59mm and its top and bottom bars are 60mm long with a width of 3mm. The extra bars were added to lower the frequency of the electric resonance to about 0.71 GHz, which gives us a negative ϵ_r from 0.71 to 0.96 GHz. The SRRs each have a length of 50mm and a height of 20mm and the capacitive gap is 4mm across, the copper strips in this case are 2mm wide. The spacing between the two SRRs is 10mm (two were used to increase the ω_p of μ_r enough to achieve a negative index) and the combination of the two has a magnetic resonance at 0.91 GHz, giving us a negative μ_r from 0.91 to 0.95 GHz. The resonators are placed on either side of a substrate block 4mm across with $\epsilon_r = 2.2$ to approximate the popular FR4 substrate. As we have seen before, placing resonators in proximity introduces coupling which affects the resonant frequencies of the resonators. In this case the resonance of the bar without the split rings is shifted from 0.72 GHz to 0.71 GHz and the resonance of the rings without the bar is shifted from 0.99 GHz to 0.91 GHz. We can see the extracted refractive index in Figure 12 (b), where we have used the refractive index extraction formula developed by Smith et al. [68]:

$$n = \frac{1}{k_0 d} \cos^{-1} \left(\frac{1 + t^2 - r^2}{2t} \right) \quad (2.19)$$

which can be derived via the transfer matrix. A similar equation for the intrinsic impedance can also be derived in this manner, giving

$$Z = \pm \sqrt{\frac{(1+r)^2 - t^2}{(1-r)^2 - t^2}} \quad (2.20)$$

From these, we can get the permittivity and permeability via $\epsilon = n/Z$ and $\mu = nZ$. The real part of the refractive index (black line) is clearly negative in the 0.87 to 0.96 GHz region and ranges from 0 to -2.

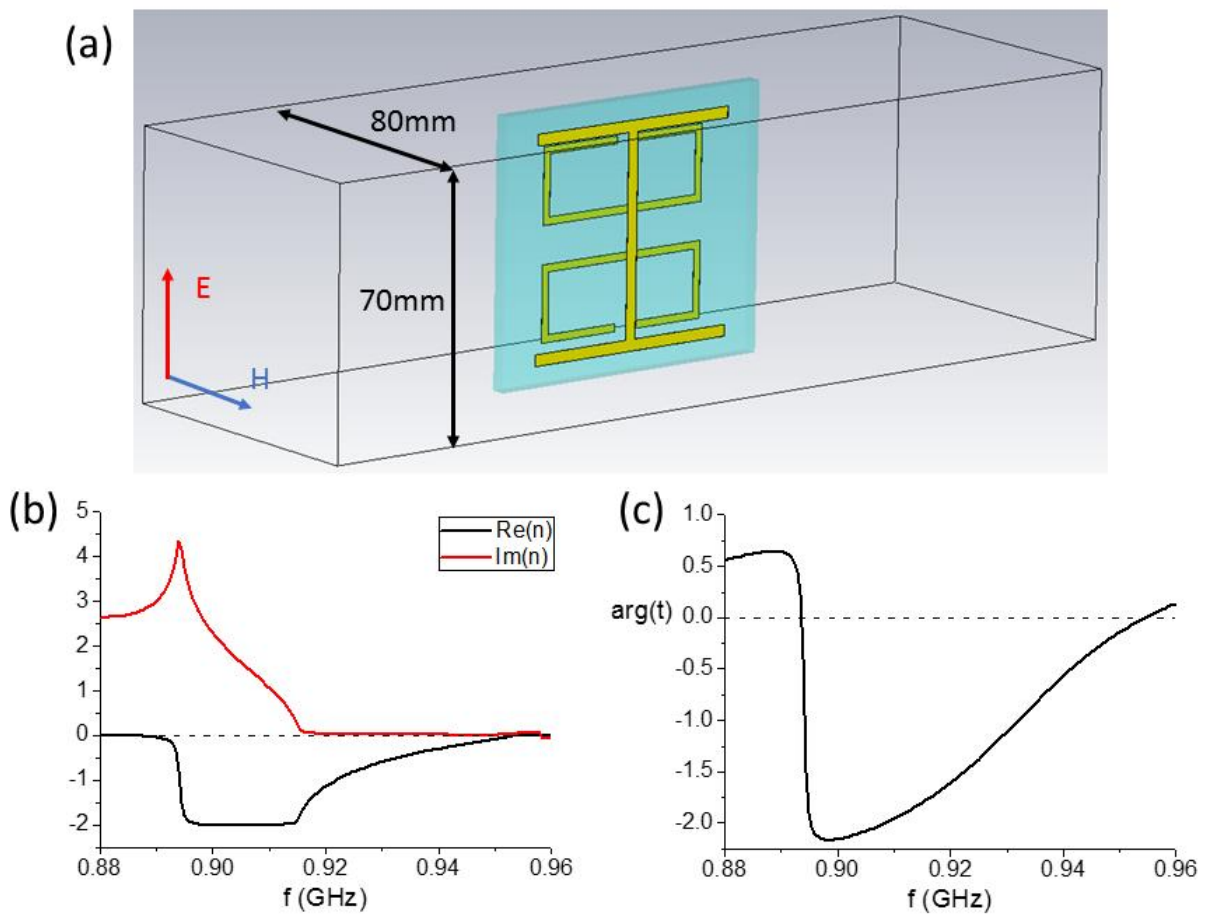


Figure 12: Unit cell of a designed negative index metamaterial. (a) shows the design of the unit cell, with the copper resonating structures (a modified bar and two split rings) shown in gold and the substrate ($\epsilon_r = 2.2$) shown in blue. The box frame shows the simulation domain and the red/blue arrows show the polarization of the incident \mathbf{E}/\mathbf{H} field. b) shows the extracted real (black line) and imaginary (red line) refractive index of the unit cell, with the dashed line showing zero for reference. c) shows the transmission phase of the unit cell, confirming that we have a negative index material.

The imaginary part is initially very large but reduces significantly in the 0.92 to 0.96 GHz region. Although the extracted refractive is negative in the stated region, the left handed medium condition which we quoted earlier (equation 2.9) is only satisfied from 0.91 to 0.95 GHz.

At 0.922 GHz we have $n = -1 + 0.03i$, which is close to the properties required for a negative index lens. Unfortunately, an impedance mismatch means that the magnitude of transmission is only 0.44 at this frequency. It should be noted that the effective refractive index formula has some issues due to the inverse cosine function, which has singularities associated with the multivalued nature of the function which can lead to sign issues. Due to this issue, it is also important to look at the transmission phase of the medium, which should go negative for a NIM. This transmission phase is plotted in Figure 12 (c), where we can see that it does indeed go negative, confirming that we have a NIM.

2.5. Chapter Summary:

In this chapter, we have explored the ideas behind the constitutive parameters which govern wave propagation in metamaterials. Starting from our definition of the constitutive matrix, we have seen the functionality of various metamaterial systems and how this functionality is linked to their effective constitutive parameters. We have also discussed some of the limitations of metamaterials in regards to losses and dispersion. A harmonic oscillator model was then used to describe electrons oscillating within a resonant structure, from which we derived equations for the permittivity and permeability of a structure based on parameters such as the resonant frequency and plasma frequency. We then analysed some basic resonating structures to see how we can determine the resonating frequency of a metamaterial from its geometry. Finally, we used this knowledge to design a basic NIM.

We have mentioned the refractive index and impedance extraction formulas developed by Smith et al. and used them on the S parameters of a NIM to extract its refractive index but this method has some significant disadvantages. One, which we have already mentioned, is the sign problem when dealing with the inverse cosine function. Another significant disadvantage is that the refractive index and impedance of a medium do not have a single value if the medium is chiral or bianisotropic, which can lead to ambiguity [69]. In the next chapter, we will derive a closed form equation which can relate the scattering parameters of a system to its constitutive matrix and so bypass this ambiguity, though at the cost of requiring the system to be subwavelength in the direction of propagation. To start, we will look again at the TMM for Maxwell's equations and show how it can be used to derive an equation to extract the constitutive parameters of a system from its scattering parameters. We will also discuss how spatial, temporal and other symmetries of the unit cell can affect these parameters.

3. Extracting the Constitutive Matrix and the Effects of Symmetries:

In order to quantify the constitutive properties of a structure, we require some method of extracting them from other measurements. The most common approach is to use the S parameters of the system, parameters which relate the reflected and transmitted waves of a system to the incident waves. In the next section, we will develop an equation which links the constitutive matrix to the scattering matrix, which will allow us to extract the constitutive parameters of a structure from simulation or experimental data. We will then discuss how we can predict the form of the effective constitutive matrix by considering spatial, temporal or other symmetries.

3.1. Modified Effective Medium Extraction for Bianisotropic Materials:

We will now derive a closed form equation relating the scattering matrix to the constitutive matrix with a method similar to that of J. Li *et al.* [70]. We saw in section 2.1 that we can use the effective constitutive matrix of a medium to relate the fields at some point z to another point $z + d$. If we now set our values of z , we can label the surfaces at z and $z + d$ as 1 and 2 respectively and write:

$$\begin{pmatrix} E_{2x} \\ E_{2y} \\ H_{2x} \\ H_{2y} \end{pmatrix} = \exp(ik_0 d [K]). \begin{pmatrix} E_{1x} \\ E_{1y} \\ H_{1x} \\ H_{1y} \end{pmatrix} \quad (3.1)$$

To get the scattering matrix, we need to convert the \mathbf{E} and \mathbf{H} fields into forwards and backwards propagating plane waves. This can be done by noting that:

$$\begin{pmatrix} E_{ix} \\ E_{iy} \\ H_{ix} \\ H_{iy} \end{pmatrix} = \begin{pmatrix} 1 & 0 & 1 & 0 \\ 0 & 1 & 0 & 1 \\ 0 & -1/Z_0 & 0 & 1/Z_0 \\ 1/Z_0 & 0 & -1/Z_0 & 0 \end{pmatrix} \cdot \begin{pmatrix} E_{ix}^+ \\ E_{iy}^+ \\ E_{ix}^- \\ E_{iy}^- \end{pmatrix} = [B] \cdot \begin{pmatrix} E_{ix}^+ \\ E_{iy}^+ \\ E_{ix}^- \\ E_{iy}^- \end{pmatrix} \quad (3.2)$$

where Z_0 is the impedance of the background medium ($Z_0 = 1$ for Lorentz-Heaviside units).

We also define the $[S]$ matrix to be:

$$\begin{pmatrix} E_{2x}^+ \\ E_{2y}^+ \\ E_{1x}^- \\ E_{1y}^- \end{pmatrix} = \begin{pmatrix} S_{xx}^{++} & S_{xy}^{++} & S_{xx}^{+-} & S_{xy}^{+-} \\ S_{yx}^{++} & S_{yy}^{++} & S_{yx}^{+-} & S_{yy}^{+-} \\ S_{xx}^{-+} & S_{xy}^{-+} & S_{xx}^{--} & S_{xy}^{--} \\ S_{yx}^{-+} & S_{yy}^{-+} & S_{yx}^{--} & S_{yy}^{--} \end{pmatrix} \cdot \begin{pmatrix} E_{1x}^+ \\ E_{1y}^+ \\ E_{2x}^- \\ E_{2y}^- \end{pmatrix} = [S] \cdot \begin{pmatrix} E_{1x}^+ \\ E_{1y}^+ \\ E_{2x}^- \\ E_{2y}^- \end{pmatrix} \quad (3.3)$$

We can now write equation (3.1) as:

$$[B] \cdot \begin{pmatrix} E_{2x}^+ \\ E_{2y}^+ \\ E_{2x}^- \\ E_{2y}^- \end{pmatrix} = \exp(ik_0 d [M] \cdot [C]^{-1}) \cdot [B] \cdot \begin{pmatrix} E_{1x}^+ \\ E_{1y}^+ \\ E_{1x}^- \\ E_{1y}^- \end{pmatrix} \quad (3.4)$$

or

$$\begin{aligned} & \left([B] \cdot \begin{pmatrix} 1 & 0 & 0 & 0 \\ 0 & 1 & 0 & 0 \\ 0 & 0 & 0 & 0 \\ 0 & 0 & 0 & 0 \end{pmatrix} - \exp(ik_0 d [M] \cdot [C]^{-1}) \cdot [B] \cdot \begin{pmatrix} 0 & 0 & 0 & 0 \\ 0 & 0 & 0 & 0 \\ 0 & 0 & 1 & 0 \\ 0 & 0 & 0 & 1 \end{pmatrix} \right) [B] \cdot \begin{pmatrix} E_{2x}^+ \\ E_{2y}^+ \\ E_{1x}^- \\ E_{1y}^- \end{pmatrix} \\ & = \left(\exp(ik_0 d [M] \cdot [C]^{-1}) \cdot [B] \cdot \begin{pmatrix} 1 & 0 & 0 & 0 \\ 0 & 1 & 0 & 0 \\ 0 & 0 & 0 & 0 \\ 0 & 0 & 0 & 0 \end{pmatrix} - [B] \cdot \begin{pmatrix} 0 & 0 & 0 & 0 \\ 0 & 0 & 0 & 0 \\ 0 & 0 & 1 & 0 \\ 0 & 0 & 0 & 1 \end{pmatrix} \right) \begin{pmatrix} E_{1x}^+ \\ E_{1y}^+ \\ E_{2x}^- \\ E_{2y}^- \end{pmatrix} \end{aligned}$$

Then, assuming that the argument of the exponential is small (i.e. the phase elapsed across the unit cell is small) and using the expansion $e^x \sim (1 + x/2)/(1 - x/2)$, we can then rearrange this into

$$[C]^{-1} = \frac{2}{ik_0 d} [M]^{-1} \cdot [B] \cdot \begin{pmatrix} 1 & 0 & 0 & 0 \\ 0 & 1 & 0 & 0 \\ 0 & 0 & -1 & 0 \\ 0 & 0 & 0 & -1 \end{pmatrix} \cdot ([S] - [I]) \cdot ([S] + [I])^{-1} \cdot [B]^{-1}$$

which simplifies to

$$[C]^{-1} = \frac{2}{ik_0 d} [B] \cdot ([S] - [I]) \cdot ([S] + [I])^{-1} \cdot [B]^{-1} \quad (3.5)$$

where $[I]$ is the 4x4 identity matrix.

For some systems, we are only concerned with how one polarization behaves, such as in waveguides where only one mode is allowed in a certain frequency range. In this case, we will have no polarization conversion (i.e. $\epsilon_{ij} = \mu_{ij} = 0$ for $i \neq j$ and $\xi_{ii} = \zeta_{ii} = 0$) so that the two polarizations are totally decoupled and we can neglect one of them. We can now describe this system with a reduced 2x2 constitutive matrix. If we choose our polarization to be E_x , then our effective medium is given by

$$\begin{pmatrix} D_x \\ B_y \end{pmatrix} = \begin{pmatrix} \epsilon_{xx} & \xi_{xy} \\ \zeta_{yx} & \mu_{yy} \end{pmatrix} \cdot \begin{pmatrix} E_x \\ H_y \end{pmatrix} \quad (3.6)$$

and our scattering matrix is defined by

$$\begin{pmatrix} E_{2x}^+ \\ E_{1x}^- \end{pmatrix} = \begin{pmatrix} S_{xx}^{++} & S_{xx}^{+-} \\ S_{xx}^{-+} & S_{xx}^{--} \end{pmatrix} \cdot \begin{pmatrix} E_{1x}^+ \\ E_{2x}^- \end{pmatrix} = [S] \cdot \begin{pmatrix} E_{1x}^+ \\ E_{2x}^- \end{pmatrix} \quad (3.7)$$

In general, we will not specify the polarization for these kinds of systems so we will refer to the scattering parameters $S_{xx}^{++}, S_{xx}^{+-}, S_{xx}^{-+}$ and S_{xx}^{--} as t_f, r_b, r_f and t_b , respectively. In this reduced case, we can still use equation 3.5 to connect $[C]^{-1}$ and $[S]$. All we need to do is change $[I]$ and $[B]$ where $[I]$ is now the 2x2 identity matrix and $[B]$ is given by

$$[B] = \begin{pmatrix} 1 & 1 \\ 1/Z_0 & -1/Z_0 \end{pmatrix}. \quad (3.8)$$

Although we have specified E_x polarization, this reduced extraction method can be used anywhere where only one polarization is of concern.

In the previous discussion, we have assumed that the reference planes for the scattering matrix follow the standard convention, i.e. the S parameters are defined using the forwards and backwards propagating fields measured at the two interfaces (1 and 2). However, there are other conventions we can use that can make analysis easier. One of these involves collapsing the reference planes to the middle of the sample, which is similar to the process of de-embedding in the context of transmission lines. This is done by cancelling out the phase accumulated by the background material. For example, if we have propagation through a homogeneous medium, then the scattering matrix will be $[S] = e^{ikd}I$, where k is the wavenumber inside the medium and d is the distance propagated. To collapse the reference planes to the centre, then all we need to do is cancel out the propagation phase, i.e. divide by e^{ikd} . So, our ‘collapsed’ scattering matrix is now just the identity matrix. In the case of a freespace background (and for $k_0d \ll 1$), extracting the effective medium from this ‘collapsed’ scattering matrix (via equation 3.13) will give the polarizability of the medium (i.e. $[C]^{-1} - I$). This process is shown in Figure 13, where we start off with the standard reference plane convention in (a) and then collapse the reference planes by propagating the electric and magnetic fields to the middle plane by a phase factor, shown in (b). This method can be useful in analysis, as zeroes in the phase of the S parameters (e.g. when phase is wrapped from π to $-\pi$ then passes through zero) and standing waves between the ports can cause false resonances in the extracted effective medium, which can obscure the resonances originating from the structures. For a more general background medium, we can derive the method by considering a transfer matrix approach.

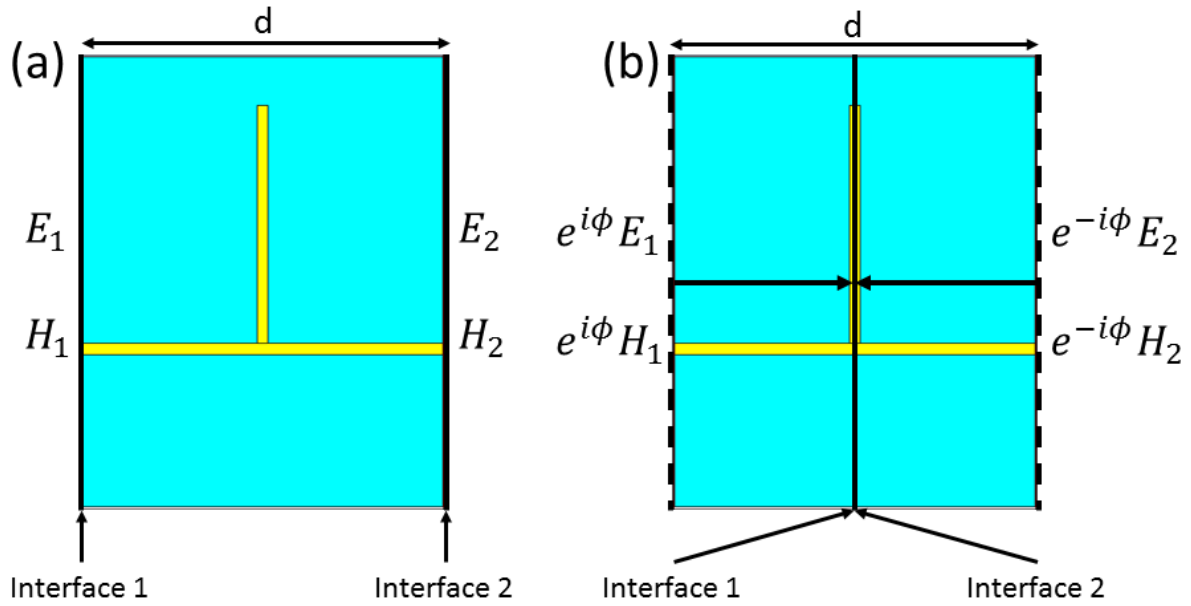


Figure 13: Illustration of the reference plane collapse process. The standard reference plane convention for measuring S parameters is shown in (a), with the measured electric and magnetic fields at the planes denoted by E_i and H_i . The middle plane convention is shown in (b), where the corresponding electric and magnetic fields are shifted to the middle plane by a phase factor $e^{\pm i\phi}$ ($\phi = kd/2$).

If we have some component(s) embedded in a background medium (e.g. a transmission line), then the total transfer matrix will be given by

$$[T_{total}] = [T_b]^{1/2} \cdot [T_{comp}] \cdot [T_b]^{1/2} \quad (3.9)$$

Where $[T_{comp}]$ is the effective transfer matrix of the components and $[T_b]$ is the transfer matrix of the background medium. This means that if we can measure $[T_b]$, then we can remove its effects from the transfer matrix (and so the scattering parameters) via the equation

$$[T_{comp}] = [T_b]^{-1/2} \cdot [T_{total}] \cdot [T_b]^{-1/2} \quad (3.10)$$

This method can be particularly useful when analysing scattering parameters, as it means that any phase accumulated in the transmission coefficients will be due to electric/magnetic activity in the sample and not the background propagation. However, for this transfer matrix method to work, the background medium must be symmetric.

This use of collapsed reference planes, however, makes the length of the system slightly ambiguous, as we are now treating the extra activity from the structures essentially as an interface in the middle of the background medium. To help alleviate this issue, there is a slightly modified version of this collapsed effective medium which is multiplied by a factor of $k_0 d$, which we refer to as the $[Y]$ matrix. This is somewhat analogous to the idea of lumped elements in electrical circuits and allows us to analyse the material response of a system without knowing its dimensions. The $[Y]$ matrix can be formulated in terms of the \mathbf{E} and \mathbf{H} fields at two interfaces by

$$\begin{aligned} \begin{pmatrix} H_{y2} - H_{y1} \\ E_{x2} - E_{x1} \end{pmatrix} &= \frac{i}{2} [Y] \cdot \begin{pmatrix} E_{x2} + E_{x1} \\ H_{y2} + H_{y1} \end{pmatrix} \\ &= \frac{i}{2} \left(kL \begin{pmatrix} 1 & 0 \\ 0 & 1 \end{pmatrix} + \begin{pmatrix} \chi_e & \xi \\ \zeta & \chi_m \end{pmatrix} \right) \cdot \begin{pmatrix} E_{x2} + E_{x1} \\ H_{y2} + H_{y1} \end{pmatrix} \end{aligned} \quad (3.11)$$

Where the kL term can be eliminated by using collapsed reference planes. This $[Y]$ matrix can now be seen to be equivalent to the susceptibilities.

To illustrate the process of extracting the $[Y]$ matrix with a middle plane, we will examine a metal bar connected to a microstrip transmission line and fit its electric susceptibility with the Lorentz model we discussed earlier. For our example structure, we have a bar resonator 2.5mm across, 53mm tall and 0.035mm deep (see Figure 14 (a)), which is attached to a transmission line. The illuminating wave in this case is a quasi-TEM mode E_z polarized wave traveling between the microstrip and the ground plane. The microstrip transmission line is formed from a central metal strip (80mm x 2.5mm x 0.035mm), a Rogers RT 5880 substrate ($\epsilon_r = 2.2 + 0.001i$) with a thickness of 0.787mm and a PEC lower surface (illustration shown in Figure 14 (a)). The extent of the simulation domain is 80mm in the x direction, 100mm in

the y direction and 20mm in the z direction. The Boundary conditions were chosen to be open in the x directions (i.e. the port faces), perfect magnetic conductor (PMC) in the y directions and PEC for the lower z surface (to enable the microstrip modes) and PMC for the upper z surface (to avoid modes forming between the upper and lower z surfaces).

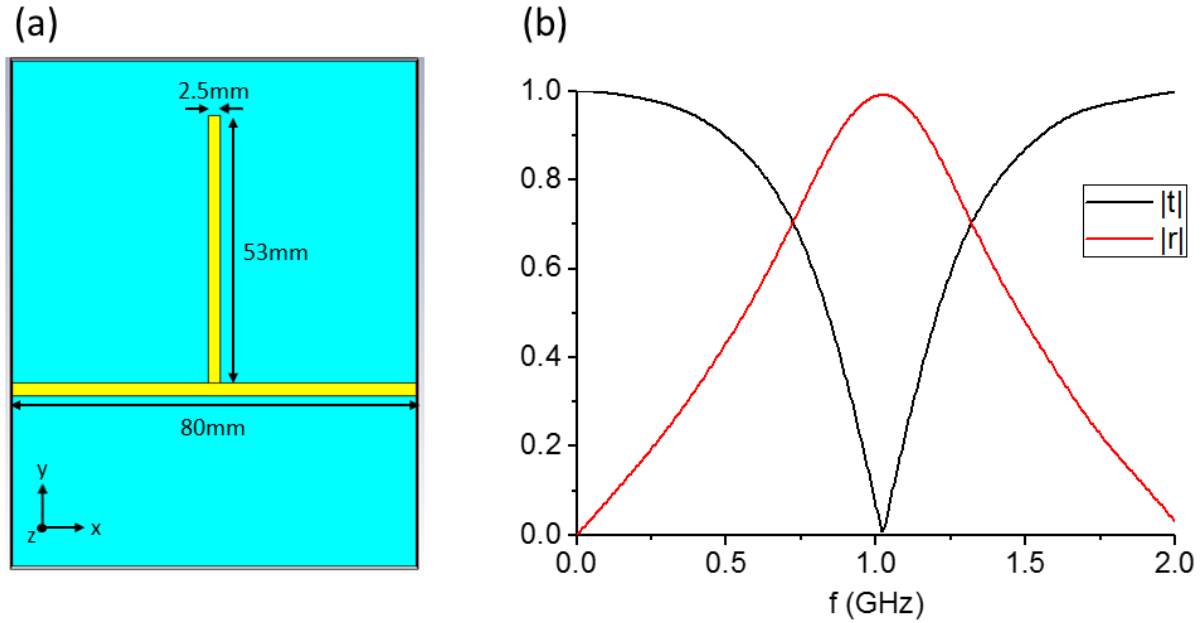


Figure 14: Example transmission line structure and its S parameters. (a) shows a picture of the simulated structure and (b) is a graph of the absolute value of the transmission and reflection coefficients, showing that there is a resonance close to 1 GHz.

Here, the simulation is using the middle plane convention discussed earlier, so we will be measuring the adjusted susceptibility (i.e. $\chi_e = \phi_0(\epsilon_r - 1)$). Using the parameters $\omega_p = 5.7 \times 10^9 \text{ rad/s}$, $\omega_r = 6.434 \times 10^9 \text{ rad/s}$ (or 1.024 GHz) and $\gamma = 3 \times 10^7 \text{ rad/s}$, we can fit the simulation data quite well (see Figure 15 (a)). We can also see from Figure 15 (b) that there is a small amount of magnetisation, indicated by a non-zero χ_m component. This is due to the approximation of the exponential function in deriving the effective medium formula. The resonating frequency of this bar can be understood through a similar argument to that in the previous section on designing resonances. The wavelength of the microwaves in the substrate at 1.024 GHz is about 200mm, so we see that now we have a quarter-wavelength resonance

in this structure. This $\lambda/4$ resonance is due to the bar's connection to the upper strip of the transmission line. This strip acts as a ground plane for the bar and allows it to act like a monopole antenna, supporting a $\lambda/4$ resonance.

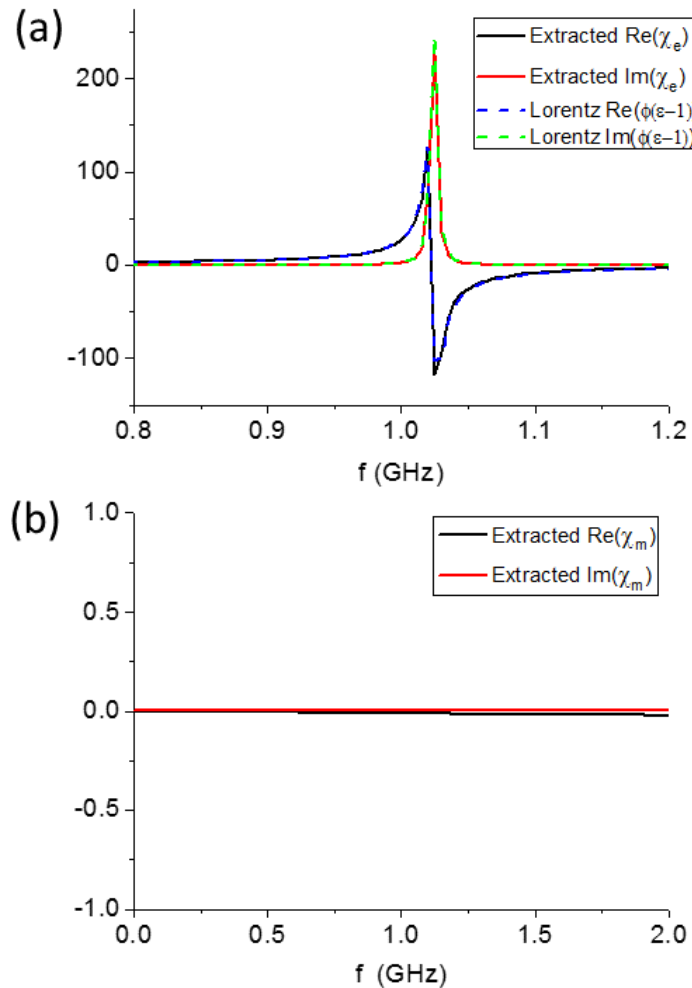


Figure 15: Extracted χ_e and χ_m for the example transmission line structure. (a) real and imaginary parts of the extracted electric susceptibility χ_e (blue and purple solid lines) and the fitted Lorentz model (dashed yellow and green lines). (b) real and imaginary parts of the extracted χ_m , which are non-zero due to the approximate nature of the extraction formula.

So far, we have only been working with the constitutive parameters of Maxwell's equations but a similar effective medium representation can also be derived for electrical circuits. If we consider a system described by Figure 16, then we can apply Kirchoff's voltage and current law in the circuit to obtain:

$$V(z, t) - V(z + \Delta z, t) = R\Delta z J(z, t) + L\Delta z \frac{\partial}{\partial t} J(z, t) \quad (3.12)$$

$$J(z, t) - J(z + \Delta z, t) = G\Delta z V(z + \Delta z, t) + C\Delta z \frac{\partial}{\partial t} V(z + \Delta z, t) \quad (3.13)$$

If we then take the limit that $\Delta z \rightarrow 0$, then we can turn the above equations into differential equations in z :

$$\frac{\partial}{\partial z} V(z, t) = -RJ(z, t) - L \frac{\partial}{\partial t} J(z, t) \quad (3.14)$$

$$\frac{\partial}{\partial z} J(z, t) = -GV(z, t) - C \frac{\partial}{\partial t} V(z, t) \quad (3.15)$$

Which bear a similarity to the equations governing the propagation of plane waves in equations 3.6.

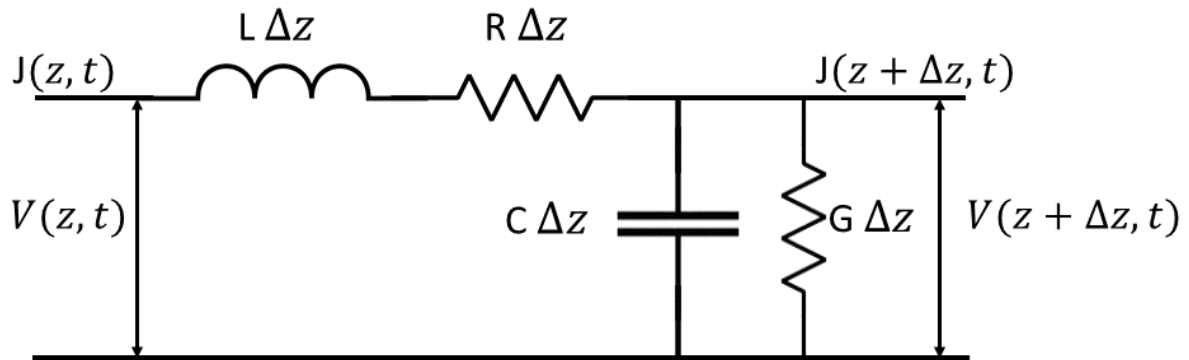


Figure 16: Mathematical representation of a section of a transmission line of length Δz and the associated voltages (V) and currents (J) at the ends of the section. The series inductance per unit length and resistivity are labelled as L and R and the shunt capacitance per unit length and conductivity are labelled as C and G .

The usual method of analysis for transmission lines is to use the ABCD matrix, which can be defined as:

$$\begin{pmatrix} V_2 \\ J_2 \end{pmatrix} = \begin{pmatrix} A & B \\ C & D \end{pmatrix} \cdot \begin{pmatrix} V_1 \\ J_1 \end{pmatrix} \quad (3.16)$$

Where the currents at the interfaces i , J_i , are defined such that they flow in the same direction. We can see that this is quite similar to the transfer matrix we saw earlier. Although this matrix is quite popular, we seek a matrix that is more like the constitutive matrix we have been discussing. In such a case, we can formulate a matrix similar to the $[Y]$ matrix that describes the propagations of voltage and current waves:

$$\begin{pmatrix} J_2 - J_1 \\ V_2 - V_1 \end{pmatrix} = \frac{i}{2} [Y] \cdot \begin{pmatrix} V_2 + V_1 \\ J_2 + J_1 \end{pmatrix}. \quad (3.17)$$

Due to the relations between the V/J and \mathbf{E}/\mathbf{H} basis (where $\mathbf{E} = -\nabla V$ and $\oint \mathbf{H} = \mathbf{J}$), this $[Y]$ matrix can be seen as an integrated version of the \mathbf{E}/\mathbf{H} basis $[Y]$ matrix. If we have the S parameters of a transmission line system, then we can use the 2x2 version of equation 3.5 to extract the transmission line equivalent of the $[Y]$ matrix.

3.2. Effective Medium of Stratified Layers:

When designing layered systems, it is not always obvious what the properties of the combined layers will be. We can make this process easier by using the TMM in conjunction with the constitutive matrix extraction method to get an overall effective medium for a composite slab system based on the parameters of the individual slabs. To do this, we first need to construct the transfer matrix of the individual slabs. Say we have a composite system composed of n slabs (where n is an integer), then the transfer matrix of the i th slab is given by $[T_i] = [B]^{-1} \cdot \exp(ik_0 d_i [M] \cdot [C_i]^{-1}) \cdot [B]$, where $[C_i]^{-1}$ and d_i are the constitutive matrix and thickness of the i th slab. We can now get the transfer matrix of the composite system by simply multiplying the individual matrices together in order: $[T_{total}] = \prod_i^n [T_i]$. We can then

convert this into the total scattering matrix of the system by noting that, for a 2x2 scattering matrix:

$$\begin{aligned}
 t_f &= T_{11} - \frac{T_{12}T_{21}}{T_{22}} \\
 r_b &= T_{12}/T_{22} \\
 r_f &= -T_{21}/T_{22} \\
 t_b &= 1/T_{22}
 \end{aligned} \tag{3.18}$$

Now we can use equation 3.5 to get the effective medium of the total slab, where d in this case is the total thickness of the composite system. Taking a first-order Taylor series of the resulting constitutive matrix in k_0d (i.e. assuming the system is subwavelength in thickness) will then allow us to see how the parameters combine.

As a simple example, we can derive the total effective medium of two homogeneous, non-bianisotropic slabs of equal thickness $d/2$, where $[C_i]^{-1} = \begin{pmatrix} \epsilon_i & 0 \\ 0 & \mu_i \end{pmatrix}$. Performing the calculations above results in a $[C]^{-1}$ of the form

$$[C_{eff}]^{-1} = \begin{pmatrix} \frac{\epsilon_1 + \epsilon_2}{2} & \frac{ik_0d}{8}(\epsilon_1\mu_2 - \epsilon_2\mu_1) \\ -\frac{ik_0d}{8}(\epsilon_1\mu_2 - \epsilon_2\mu_1) & \frac{\mu_1 + \mu_2}{2} \end{pmatrix} \tag{3.19}$$

3.3. Spatial, Temporal and Other Symmetries:

We noted previously that symmetries (or lack thereof) can be used to predict if a medium is bianisotropic or chiral. Here, we will derive the forms of $[\mathcal{C}]^{-1}$ when we have certain spatial, temporal and other symmetries. These will include the parity and time reversal operations in preparation for our discussion of PT symmetry.

3.3.1. Mirror Inversion (parity):

The act of a mirror (parity) transformation involves transforming the coordinates into those reflected through a certain plane, similar to perceiving the system as if it were viewed through a mirror. We start by quantifying the act of a mirror transformation. A mirror transformation is an improper rotation (i.e. the matrix describing it has determinant -1) which will flip the sign of any electric field components normal to the mirror plane but leave the transverse components unchanged. For magnetic fields, the effect is reversed: mirroring will leave the normal component unchanged but will reflect transverse components. To get a physical picture of why this is the case, we consider a current loop and its resulting magnetic field when it is reflected with respect to a plane which is perpendicular to the plane of the loop. The current vector in the loop will be changed such that the components normal to the reflection surface will flip sign but the tangential components will remain the same. In Figure 17 we have shown this reflection for the loop (black ring) and the resulting magnetic field lines (red lines), where we have assumed that the magnetic field obeys the same transformation rules. However, a quick application of Ampère's right-hand rule will show that Figure 17 (a) is clearly incorrect as the magnetic field produced from the current loop is pointing in the wrong direction. Figure 17 (b) shows the correct field distribution for the flipped current loop. From

this discussion, it is clear that the magnetic field must transform differently to ‘standard’ vectors under a reflection. Mathematically, this difference is due to the nature of the electric and magnetic field vectors; the electric field is a polar vector whereas the magnetic field is an axial vector because it is defined as the cross-product of polar vectors. The polar nature of the electric field can be seen from Coulomb’s law, where the static electric field vector near a charged object, defined by a position defined by a vector \mathbf{r} , can be seen to be proportional to $(\mathbf{r} - \mathbf{r}_c)/|\mathbf{r} - \mathbf{r}_c|^3$, where \mathbf{r}_c is the position of the charge. As both \mathbf{r} and \mathbf{r}_c are polar vectors and the denominator is just a number, we can see that any mirror reflection on \mathbf{r} and \mathbf{r}_c will have a similar effect on the electric field. For the magnetic field, we can note that for a constant current in a wire, the induced magnetic field at a point \mathbf{r} is proportional to $\int (d\mathbf{l} \times \mathbf{r}')/|\mathbf{r}'|^3$, where \mathbf{l} is the tangent vector for the wire and $\mathbf{r}' = \mathbf{r} - \mathbf{l}$. So, we can see that the magnetic field is defined as the cross-product of two polar (position) vectors, making it a pseudovector.

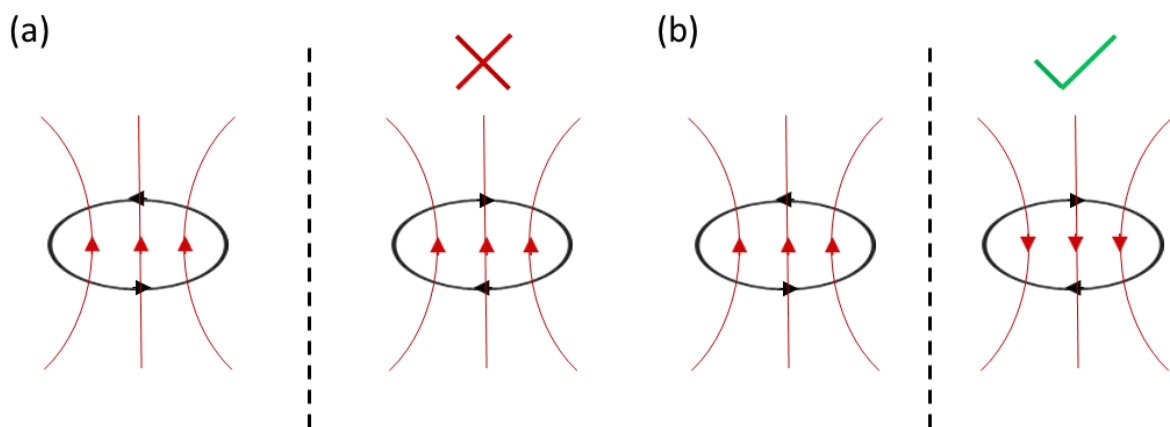


Figure 17: Illustration of the effects of a parity on the magnetic field. We show two transformations of a current loop (black ring) and its magnetic field (red lines), where the magnetic field is assumed to transform like a polar vector in (a) and like a pseudovector in (b). We can see that the magnetic field is clearly a pseudovector as the transformation in (a) produces an incorrect field pattern.

We can quantify the change in the field and constitutive parameters by a matrix transformation: if we define our fields in terms of components which are perpendicular

(subscript \perp) and parallel (subscript \parallel) to the plane of reflection, then we can describe the reflection of the parallel fields as

$$\begin{pmatrix} \mathbf{E}_{\parallel}(r) \\ \mathbf{H}_{\parallel}(r) \end{pmatrix} \rightarrow \begin{pmatrix} [I] & 0 \\ 0 & -[I] \end{pmatrix} \cdot \begin{pmatrix} \mathbf{E}_{\parallel}(-r) \\ \mathbf{H}_{\parallel}(-r) \end{pmatrix} \quad (3.20)$$

And the reflection of the perpendicular fields as

$$\begin{pmatrix} \mathbf{E}_{\perp}(r) \\ \mathbf{H}_{\perp}(r) \end{pmatrix} \rightarrow \begin{pmatrix} -[I] & 0 \\ 0 & [I] \end{pmatrix} \cdot \begin{pmatrix} \mathbf{E}_{\perp}(-r) \\ \mathbf{H}_{\perp}(-r) \end{pmatrix} \quad (3.21)$$

Where $[I]$ is the 2x2 identity matrix.

If we limit ourselves to the case where we are working with averaged \mathbf{E} and \mathbf{H} fields (so no coordinate dependence) and where the normals of our mirror planes are parallel to the Cartesian axes, we have $\mathcal{M}_x: (E_x, E_y, E_z, H_x, H_y, H_z) \rightarrow (-E_x, E_y, E_z, H_x, -H_y, -H_z)$, $\mathcal{M}_y: (E_x, E_y, E_z, H_x, H_y, H_z) \rightarrow (E_x, -E_y, E_z, -H_x, H_y, -H_z)$, $\mathcal{M}_z: (E_x, E_y, E_z, H_x, H_y, H_z) \rightarrow (E_x, E_y, -E_z, -H_x, -H_y, H_z)$. These can be written in terms of a matrix operation $\begin{pmatrix} \mathbf{E}' \\ \mathbf{H}' \end{pmatrix} = [\mathcal{M}_i] \cdot \begin{pmatrix} \mathbf{E} \\ \mathbf{H} \end{pmatrix}$, where $i \in \{x, y, z\}$.

The \mathbf{D} and \mathbf{B} fields change in a similar way to the \mathbf{E} and \mathbf{H} fields, so in order for our $[C]^{-1}$ to be invariant under a mirror operation it must satisfy $[C]^{-1} = [\mathcal{M}_i] \cdot [C]^{-1} \cdot [\mathcal{M}_i]^{-1}$. This condition allows us to derive which effective medium components must go to zero for a certain symmetry. The table below shows the forms of $[C]^{-1}$ for x , y and z symmetries (where x , y and z denote the axis which is normal to the mirror plane). We use the 3x3 constitutive matrix here to show the full effects of these symmetries.

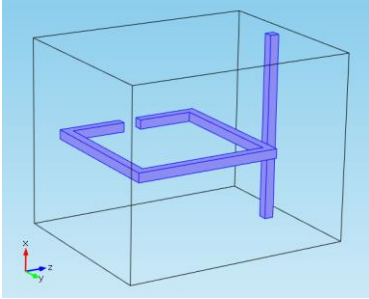
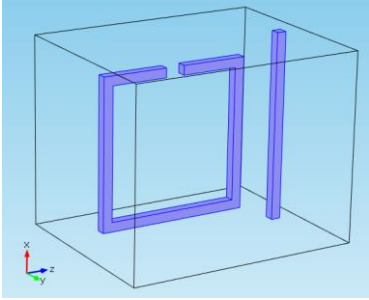
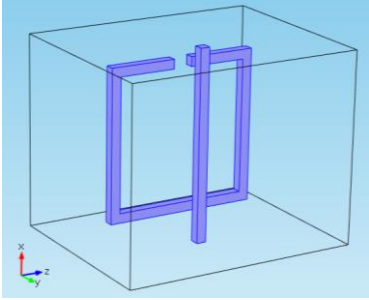
Mirror symmetry	Example structure	Form of C^{-1}
\mathcal{M}_x		$\begin{pmatrix} \epsilon_{xx} & 0 & 0 & 0 & \xi_{xy} & \xi_{xz} \\ 0 & \epsilon_{yy} & \epsilon_{yz} & \xi_{yx} & 0 & 0 \\ 0 & \epsilon_{zy} & \epsilon_{zz} & \xi_{zx} & 0 & 0 \\ 0 & \zeta_{xy} & \zeta_{xz} & \mu_{xx} & 0 & 0 \\ \zeta_{yx} & 0 & 0 & 0 & \mu_{yy} & \mu_{yz} \\ \zeta_{zx} & 0 & 0 & 0 & \mu_{zy} & \mu_{zz} \end{pmatrix}$
\mathcal{M}_y		$\begin{pmatrix} \epsilon_{xx} & 0 & \epsilon_{xz} & 0 & \xi_{xy} & 0 \\ 0 & \epsilon_{yy} & 0 & \xi_{yx} & 0 & \xi_{yz} \\ \epsilon_{zx} & 0 & \epsilon_{zz} & 0 & \xi_{zy} & 0 \\ 0 & \zeta_{xy} & 0 & \mu_{xx} & 0 & \mu_{xz} \\ \zeta_{yx} & 0 & \zeta_{yz} & 0 & \mu_{yy} & 0 \\ 0 & \zeta_{zy} & 0 & \mu_{zx} & 0 & \mu_{zz} \end{pmatrix}$
\mathcal{M}_z		$\begin{pmatrix} \epsilon_{xx} & \epsilon_{xy} & 0 & 0 & 0 & \xi_{xz} \\ \epsilon_{yx} & \epsilon_{yy} & 0 & 0 & 0 & \xi_{yz} \\ 0 & 0 & \epsilon_{zz} & \xi_{zx} & \xi_{zy} & 0 \\ 0 & 0 & \zeta_{xz} & \mu_{xx} & \mu_{xy} & 0 \\ 0 & 0 & \zeta_{yz} & \mu_{yx} & \mu_{yy} & 0 \\ \zeta_{zx} & \zeta_{zy} & 0 & 0 & 0 & \mu_{zz} \end{pmatrix}$

Table 1: Examples of unit cells composed of SRRs and bars with certain symmetry planes and the resulting form of the effective C^{-1} matrix.

One consequence of these reflection symmetries is that they ensure that the co-polarization magneto-electric coupling terms of $[C]^{-1}$ (i.e. ξ_{ii} and ζ_{ii}) are zero. In fact, these terms are called chiral parameters as only chiral media (media which lack any mirror symmetry, such as spirals) can have them. We can also see that \mathcal{M}_z symmetry will result in the bianisotropy parameters ($\xi_{xy}, \xi_{yx}, \zeta_{xy}, \zeta_{yx}$) being zero, this implies that in order to have bianisotropy, we must break symmetry in the propagation direction. We can interpret these symmetries physically too. For example, the \mathcal{M}_x and \mathcal{M}_y structures both have zero ϵ_{xy} and ϵ_{yx} . This is because there no way for an x-polarized electric field to induce a current in the y direction in these structures. If the SRR were rotated about the z axis by 45° , then an x-polarized field

would induce a current along the arms of the SRR, which would have a y component and so we could have non-zero ϵ_{xy} and ϵ_{yx} .

For symmetry planes whose normal vectors are not the coordinate basis vectors, one can either rotate the constitutive matrix so that one of its axes is parallel to the normal vector of the mirror plane, perform the required mirror operation and then rotate it back to its original basis, or use the Householder transformation matrix, remembering that polar and axial vector components change differently under a reflection.

3.3.2. Rotation:

A rotation transformation is a proper rotation (i.e. described by a matrix with determinant 1) and so we do not need to distinguish between polar and axial vectors (i.e. the \mathbf{E} and \mathbf{H} fields) when we transform them. For rotational symmetries about a coordinate axis (denoted by subscript i) we need to enforce that $[C]^{-1} = R_i(\theta) \cdot [C]^{-1} \cdot R_i^{-1}(\theta)$ ($i \in \{x, y, z\}$) where:

$$[R_i] = \begin{pmatrix} [X_i(\theta)] & [0] \\ [0] & [X_i(\theta)] \end{pmatrix} \quad (3.22)$$

and

$$\begin{aligned} [X_x(\theta)] &= \begin{pmatrix} 1 & 0 & 0 \\ 0 & \cos \theta & -\sin \theta \\ 0 & \sin \theta & \cos \theta \end{pmatrix} \\ [X_y(\theta)] &= \begin{pmatrix} \cos \theta & 0 & -\sin \theta \\ 0 & 1 & 0 \\ \sin \theta & 0 & \cos \theta \end{pmatrix} \\ [X_z(\theta)] &= \begin{pmatrix} \cos \theta & -\sin \theta & 0 \\ \sin \theta & \cos \theta & 0 \\ 0 & 0 & 1 \end{pmatrix} \end{aligned} \quad (3.23)$$

To find discrete symmetries of order n (i.e. C_n symmetries) in a certain plane, we need to enforce that $[C]^{-1} = [R_i(2\pi/n)] \cdot [C]^{-1} [R_i(2\pi/n)]^{-1}$. As an example, if we take rotation

about the z axis, or rotation in the x - y plane, then a summary of the forms of $[C]^{-1}$ for structures which are C_2 , C_3 and C_4 symmetric can be seen in the table below.

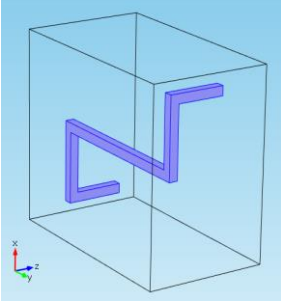
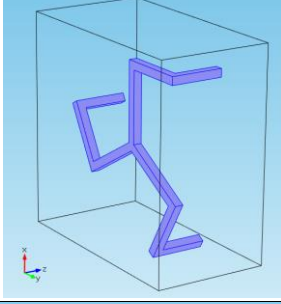
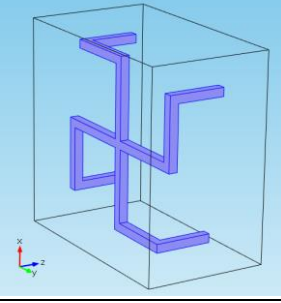
x - y plane rotational symmetry	Example structure	Form of $[C]^{-1}$
C_2		$\begin{pmatrix} \epsilon_{xx} & \epsilon_{xy} & 0 & \xi_{xx} & \xi_{xy} & 0 \\ \epsilon_{yx} & \epsilon_{yy} & 0 & \xi_{yx} & \xi_{yy} & 0 \\ 0 & 0 & \epsilon_{zz} & 0 & 0 & \xi_{zz} \\ \zeta_{xx} & \zeta_{xy} & 0 & \mu_{xx} & \mu_{xy} & 0 \\ \zeta_{yx} & \zeta_{yy} & 0 & \mu_{yx} & \mu_{yy} & 0 \\ 0 & 0 & \zeta_{zz} & 0 & 0 & \mu_{zz} \end{pmatrix}$
C_3		$\begin{pmatrix} \epsilon_{xx} & \epsilon_{xy} & 0 & \xi_{xx} & \xi_{xy} & 0 \\ -\epsilon_{xy} & \epsilon_{xx} & 0 & -\xi_{xy} & \xi_{xx} & 0 \\ 0 & 0 & \epsilon_{zz} & 0 & 0 & \xi_{zz} \\ \zeta_{xx} & \zeta_{xy} & 0 & \mu_{xx} & \mu_{xy} & 0 \\ -\zeta_{xy} & \zeta_{xx} & 0 & -\mu_{xy} & \mu_{xx} & 0 \\ 0 & 0 & \zeta_{zz} & 0 & 0 & \mu_{zz} \end{pmatrix}$
C_4		

Table 2: Examples of the forms of the C^{-1} matrix for C_2 , C_3 and C_4 symmetric unit cells. For C_3 and C_4 symmetries, we can see additional constraints such as the condition that the yx terms are negatives of the xy terms. In a reciprocal medium (where $[\epsilon] = [\epsilon]^T$ and $[\mu] = [\mu]^T$) this condition is equivalent saying that $\epsilon_{xy} = \epsilon_{yx} = \mu_{xy} = \mu_{yx} = 0$. We can also see that these systems now become uniaxial. It should be noted that structures with higher order symmetries (i.e. C_5 , C_6 , C_7 etc.) we have the same symmetry conditions on $[C]^{-1}$ as C_3 and C_4 symmetric structures.

3.3.3. Time-reversal:

Time reversal is essentially the setting of $t \rightarrow -t$, meaning that time reversed systems will appear to run backwards in time. This transformation will obviously not affect spatial vectors

but any quantities that are the time derivatives of spatial quantities, such as velocities and currents, will all be reversed under a time reversal operation. To see what effects this will have on our field quantities, we look at one of Maxwell's equations:

$$\nabla \times \mathbf{H} = \frac{\partial \mathbf{D}}{\partial t} + \mathbf{J}$$

If we set $\partial/\partial t \rightarrow -\partial/\partial t$ and $\mathbf{J} \rightarrow -\mathbf{J}$, then we can see that if Maxwell's equations are to retain the same form then we must have $\mathbf{H} \rightarrow -\mathbf{H}$. This also makes sense from a physical perspective, as reversing the current vectors should consequently reverse the magnetic field vectors. Using this method, we can derive how the other field quantities transform: $\mathbf{E}(\mathbf{r}, t) \rightarrow \mathbf{E}(\mathbf{r}, -t)$, $\mathbf{D}(\mathbf{r}, t) \rightarrow \mathbf{D}(\mathbf{r}, -t)$, $\mathbf{J}(\mathbf{r}, t) \rightarrow -\mathbf{J}(\mathbf{r}, -t)$, $\mathbf{H}(\mathbf{r}, t) \rightarrow -\mathbf{H}(\mathbf{r}, -t)$, $\mathbf{B}(\mathbf{r}, t) \rightarrow -\mathbf{B}(\mathbf{r}, -t)$. We can also apply this transformation to the constitutive parameters: $\epsilon(\mathbf{r}, t) \rightarrow \epsilon(\mathbf{r}, -t)$, $\mu(\mathbf{r}, t) \rightarrow \mu(\mathbf{r}, -t)$, $\zeta(\mathbf{r}, t) \rightarrow -\zeta(\mathbf{r}, -t)$, $\xi(\mathbf{r}, t) \rightarrow -\xi(\mathbf{r}, -t)$, where the bianisotropic terms change sign due to the change of sign of the \mathbf{H} field. When working with Maxwell's equations we usually assume that the time dependence is time-harmonic (i.e. is proportional to $e^{-i\omega t}$), which means that we can relate the frequency and time varying parameters via a Fourier transformation. This means that for some variable $F(\mathbf{r}, \omega)$, a transformation of $t \rightarrow -t$ is equivalent to $F(\mathbf{r}, \omega) \rightarrow F^*(\mathbf{r}, \omega)$. This means that in the frequency domain we have $\mathbf{E}(\mathbf{r}, \omega) \rightarrow \mathbf{E}^*(\mathbf{r}, \omega)$, $\mathbf{J}(\mathbf{r}, \omega) \rightarrow -\mathbf{J}^*(\mathbf{r}, \omega)$, $\mathbf{H}(\mathbf{r}, \omega) \rightarrow -\mathbf{H}^*(\mathbf{r}, \omega)$. We can quantify the effect of a time reversal on the electric and magnetic fields in terms of a matrix $[T]$:

$$\begin{pmatrix} \mathbf{E}(\mathbf{r}, \omega) \\ \mathbf{H}(\mathbf{r}, \omega) \end{pmatrix} \rightarrow \begin{pmatrix} [I] & [0] \\ [0] & -[I] \end{pmatrix} \cdot \begin{pmatrix} \mathbf{E}(\mathbf{r}, \omega) \\ \mathbf{H}(\mathbf{r}, \omega) \end{pmatrix} = [T] \cdot \begin{pmatrix} \mathbf{E}(\mathbf{r}, \omega) \\ \mathbf{H}(\mathbf{r}, \omega) \end{pmatrix} \quad (3.24)$$

where $[I]$ is the 3x3 identity matrix, $[0]$ is the 3x3 null matrix and K is the complex conjugation operator. As is usual with matrix transformations, the transformed constitutive matrix is given by $[T].[C]^{-1}.[T]^{-1}$. Invariance under this transformation implies that $[T].[C]^{-1}.[T]^{-1} = [C]^{-1}$. If we apply this to an effective $[C]^{-1}$ as before, we can prove that if a medium is time symmetric, then its effective constitutive parameters must obey $[\epsilon] = [\epsilon]^*$, $[\mu] = [\mu]^*$, $[\zeta] = -[\zeta]^*$, $[\xi] = -[\xi]^*$. So, in order for our system to be time-invariant, we must have purely real permittivities and permeabilities and purely imaginary bianisotropic/chiral terms.

Most real materials are not symmetric with respect to time as they contain loss mechanisms where EM waves can be converted into other forms of energy, such as phonons, which show up as imaginary terms in the constitutive parameters. There are, however, some lossless systems which break time reversal symmetry. An example is a gyrotropic medium, where a DC magnetic field can produce a permittivity of the form

$$[\epsilon] = \begin{pmatrix} \epsilon_{xx} & \epsilon_{xy} + ig_z & \epsilon_{xz} - ig_y \\ \epsilon_{xy} - ig_z & \epsilon_{yy} & \epsilon_{yz} + ig_x \\ \epsilon_{xz} + ig_y & \epsilon_{yz} - ig_x & \epsilon_{zz} \end{pmatrix} \quad (3.25)$$

Where the vector $\mathbf{g} = (g_x, g_y, g_z)$ is proportional to the applied magnetic field. This medium has the intriguing property that, although it is not time symmetric, it is still lossless (i.e. reflected power + transmitted power=incident power) as long as ϵ_{ij} and g_i are all real numbers. This is because it is still Hermitian and so describes a unitary process. The trade-off for the breaking of time symmetry is that the medium is no longer reciprocal for circularly polarized light, so a left/right circularly polarized wave will have different transmission coefficients for different directions of incidence.

3.3.4. Electric-Magnetic Duality:

There is a fundamental symmetry of Maxwell's equations which relates to a rotation of the \mathbf{E} and \mathbf{H} fields. To derive it, we start with Maxwell's equations in free space:

$$\begin{pmatrix} 0 & \nabla \times \\ \nabla \times & 0 \end{pmatrix} \cdot \begin{pmatrix} \mathbf{E} \\ \mathbf{H} \end{pmatrix} = \begin{pmatrix} \partial_t & 0 \\ 0 & -\partial_t \end{pmatrix} \cdot \begin{pmatrix} \mathbf{E} \\ \mathbf{H} \end{pmatrix}$$

we then transform the fields via some transformation matrix A so that

$$\begin{pmatrix} \mathbf{E}' \\ \mathbf{H}' \end{pmatrix} = \begin{pmatrix} a & b \\ c & d \end{pmatrix} \cdot \begin{pmatrix} \mathbf{E} \\ \mathbf{H} \end{pmatrix} = [A] \cdot \begin{pmatrix} \mathbf{E} \\ \mathbf{H} \end{pmatrix} \quad (3.26)$$

If we then insist that Maxwell's equations should have the same form under this transformation, we can prove that the elements of A should satisfy $ab + cd = 0$, $(a^2 + c^2)/(ad - bc) = 1$ and $(b^2 + d^2)/(ad - bc) = 1$. One non-trivial solution of this is a rotation matrix:

$$[A] = \begin{pmatrix} \cos(\theta) & \sin(\theta) \\ -\sin(\theta) & \cos(\theta) \end{pmatrix} \quad (3.27)$$

If we extend the equations to include charges, then we can prove they will transform in a similar manner:

$$\begin{pmatrix} q'_e \\ q'_m \end{pmatrix} = [A] \cdot \begin{pmatrix} q_e \\ q_m \end{pmatrix} \quad (3.28)$$

where q_e is the electric charge and q_m is the (so far hypothetical) magnetic charge. This transformation is a continuous function of θ , so we can have an infinite number of conditions on the constitutive matrix. As an example, we can take the most typical duality

transformation: $\mathbf{E} \rightarrow \mathbf{H}$ and $\mathbf{H} \rightarrow -\mathbf{E}$, which corresponds to setting $\theta = \pi/2$. $[\mathbf{C}]^{-1}$ will be invariant under this transformation if $[\epsilon] = [\mu]$ and $[\xi] = -[\zeta]$.

3.3.5. Reciprocity:

Reciprocity is the property of a medium which says that for a field source at a point 1 and a receiver at a point 2, the transmission measured from point 1 to point 2 would be the same as if it were measured when the source was at point 2 and the receiver at point 1. In terms of the scattering parameters, this can be written as $S_{ij}^{++} = S_{ji}^{--}$.

To derive the properties of the constitutive tensor of our reciprocal medium, we must define a way of quantifying the electromagnetic interaction between two points. The most common way to do this is to formulate a reactance linking two points (labelled p and q). This reactance is defined as

$$\langle p, q \rangle = \int (\mathbf{J}_e^p \cdot \mathbf{E}^q - \mathbf{J}_m^p \cdot \mathbf{H}^q) dV \quad (3.29)$$

Where \mathbf{J}_e^i is the electrical displacement current at point i, defined as $\mathbf{J}_e^i = \nabla \times \mathbf{H}^i + i\omega \mathbf{D}^i$ and the magnetic displacement current (\mathbf{J}_m^i) is defined as $\mathbf{J}_m^i = \nabla \times \mathbf{E}^i - i\omega \mathbf{B}^i$. So we can re-write our reactance as

$$\begin{aligned} \langle p, q \rangle = \int & (\nabla \times \mathbf{H}^p + i\omega([\epsilon] \cdot \mathbf{E}^p + [\xi] \cdot \mathbf{H}^p)) \cdot \mathbf{E}^q \\ & - (\nabla \times \mathbf{E}^p + i\omega([\zeta] \cdot \mathbf{E}^p + [\mu] \cdot \mathbf{H}^p)) \cdot \mathbf{H}^q dV \end{aligned} \quad (3.30)$$

The principle of reciprocity states that the reactions between p and q must be the same, i.e. $\langle p, q \rangle = \langle q, p \rangle$. Assuming this to be true implies that

$$\begin{aligned}
& \int (\nabla \times \mathbf{H}^p \cdot \mathbf{E}^q - \nabla \times \mathbf{E}^p \cdot \mathbf{H}^q - \nabla \times \mathbf{H}^q \cdot \mathbf{E}^p + \nabla \times \mathbf{E}^q \cdot \mathbf{H}^p) dV \\
& + i\omega \int ([\epsilon] \cdot \mathbf{E}^p \cdot \mathbf{E}^q - [\epsilon] \cdot \mathbf{E}^q \cdot \mathbf{E}^p + [\xi] \cdot \mathbf{H}^p \cdot \mathbf{E}^q - [\xi] \cdot \mathbf{H}^q \cdot \mathbf{E}^p + [\zeta] \cdot \mathbf{E}^p \cdot \mathbf{H}^q \\
& - [\zeta] \cdot \mathbf{E}^q \cdot \mathbf{H}^p + [\mu] \cdot \mathbf{H}^p \cdot \mathbf{H}^q - [\mu] \cdot \mathbf{H}^q \cdot \mathbf{H}^p) dV = 0
\end{aligned}$$

By realising that for two vectors \mathbf{A} and \mathbf{B} and an arbitrary matrix, $[Q]$, $([Q] \cdot \mathbf{A}) \cdot \mathbf{B} = ([Q]^T \cdot \mathbf{B}) \cdot \mathbf{A}$ and that reversing the direction of propagation reverses the sign of \mathbf{H} , we can rewrite the second half as

$$\begin{aligned}
& i\omega \int (([\epsilon] - [\epsilon]^T) \cdot \mathbf{E}^p \cdot \mathbf{E}^q + ([\xi] + [\zeta]^T) \cdot \mathbf{H}^p \cdot \mathbf{E}^q + ([\zeta] + [\xi]^T) \cdot \mathbf{E}^p \cdot \mathbf{H}^q + ([\mu] \\
& - [\mu]^T) \cdot \mathbf{H}^p \cdot \mathbf{H}^q) dV = 0
\end{aligned}$$

Which gives us the usually quoted reciprocity relations for a medium:

$$[\epsilon] = [\epsilon]^T, [\mu] = [\mu]^T, [\zeta] = -[\xi]^T \quad (3.31)$$

Most systems are reciprocal but some prominent exceptions are those with nonlinear circuit elements, such as diodes and transistors, and magneto-optical systems, such as the gyrotropic medium discussed earlier.

3.3.6. Hermiticity:

The condition of Hermiticity (named after the mathematician Charles Hermite) is a property that is central to quantum mechanics. It ensures that the eigenvalues of matrices and operators are real. In quantum mechanics, Hermiticity is enforced on the operators of observables (and their associated matrices) to ensure that all physical observables are real quantities, which is obviously desirable from a physical perspective. Hermiticity is also useful

when applied to Hamiltonians as it will ensure that total probabilities are conserved as the system evolves in time (a.k.a. unitarity). Mathematically, a Hermitian operator A is one that satisfies the property of self-adjointness:

$$\int \phi^*(A\psi) dx = \int (A\phi)^*\psi dx \quad (3.32)$$

In terms of matrices, this condition can be shown to be equivalent to that where the matrix is the same as its conjugate transpose: $[A] = ([A]^T)^* = [A]^\dagger$. In terms of our constitutive parameters, this implies that

$$[\epsilon] = [\epsilon]^\dagger, [\mu] = [\mu]^\dagger \text{ and } [\xi] = [\zeta]^\dagger \quad (3.33)$$

Any system obeying this will be Hermitian. The concept of unitarity in QM approximately translates into the conservation of power in electromagnetism, which can be expressed either in terms of the Poynting vector \mathbf{N} (where $\mathbf{N} = \mathbf{E} \times \mathbf{H}$) as $\int \nabla \cdot \mathbf{N} dV = 0$, or in terms of the scattering parameters: $\sum_i |S_{ij}|^2 = 1$. An additional consequence of Hermiticity on the scattering matrix is that the scattering matrix is unitary, meaning that its eigenvalues lie on the unit circle.

On a related note, the constitutive matrix is closely related to the electromagnetism Hamiltonian:

$$H = \int \left((\mathbf{E}^*, \mathbf{H}^*) \cdot [\mathcal{C}]^{-1} \cdot \begin{pmatrix} \mathbf{E} \\ \mathbf{H} \end{pmatrix} \right) dV \quad (3.34)$$

In fact, we can use this to derive the full condition of energy conservation of the system. Taking the total time derivative of the equation above and rearranging the terms using equations 3.1 and 3.2, we find that

$$\begin{aligned} \frac{d}{dt}H = \int \left((\mathbf{E}^*, \mathbf{H}^*) \cdot \begin{bmatrix} 0 & \nabla \times \\ -\nabla \times & 0 \end{bmatrix} (1 - [C]^\dagger \cdot [C]^{-1}) \right. \\ \left. - \frac{d}{dt}([C]^{-1}) \cdot [C]^\dagger \cdot [C]^{-1} \right) \cdot \begin{pmatrix} \mathbf{E} \\ \mathbf{H} \end{pmatrix} dV \end{aligned} \quad (3.35)$$

So, we can see that if our energy density is to be conserved over time, we require that $1 - [C]^\dagger \cdot [C]^{-1} = 0$ (i.e. $[C]^{-1}$ is Hermitian) and that $\frac{d}{dt}([C]^{-1}) = 0$. These are very similar to the conditions on the Hamiltonian in quantum mechanics, where Hermiticity guarantees a real eigenvalue spectrum and fixes the unitarity of the evolution operator ($|e^{-iHt/\hbar}| = 1$) and the time independence guarantees time translation invariance, which leads to energy conservation via Noether's theorem. In light of this correspondence, we can expect that enforcing conditions such as PT symmetry on the constitutive matrix will be the electromagnetism equivalent of enforcing them on the Hamiltonian in quantum mechanics.

3.4. Chapter Summary:

In this chapter, we have further expanded on the link between wave propagation and the constitutive parameters, where we have developed an extraction formula to relate the scattering parameters of a system to its effective $[C]^{-1}$ matrix and discussed various conventions for the $[S]$ and $[C]^{-1}$ matrices. We then showed how we can use this extraction formula to derive the effective medium of stacked slabs, which will assist us in designing a PT symmetric system later. We then discussed various symmetry operations, including the mirror reflection (parity) and time-reversal operations, and showed the conditions on the constitutive matrix when it is subject to these symmetries.

Now that we know more about the time-reversal and various parity operations and their effects on the $[C]^{-1}$ matrix (which, we showed, can be interpreted as the Hamiltonian of the system), we will move on to the subject of PT symmetry and show the effects of this symmetry on the constitutive matrix and scattering properties of a system for a variety of parity operators.

4. Parity-Time Symmetry and Parity Redefinition:

4.1. Early Developments and Background:

PT symmetry was proposed in 1998 by Carl Bender and Stefan Boettcher as an extension of the concept of Hermiticity in quantum mechanics [1,71]. They studied Hamiltonians of the form $H = p^2 - (ix)^N$ (where N is a real number) and found that most positive values of N (e.g. $N=3$) resulted in a totally real energy eigenvalue spectrum, even though the corresponding Hamiltonian is clearly not Hermitian (see Figure 18).

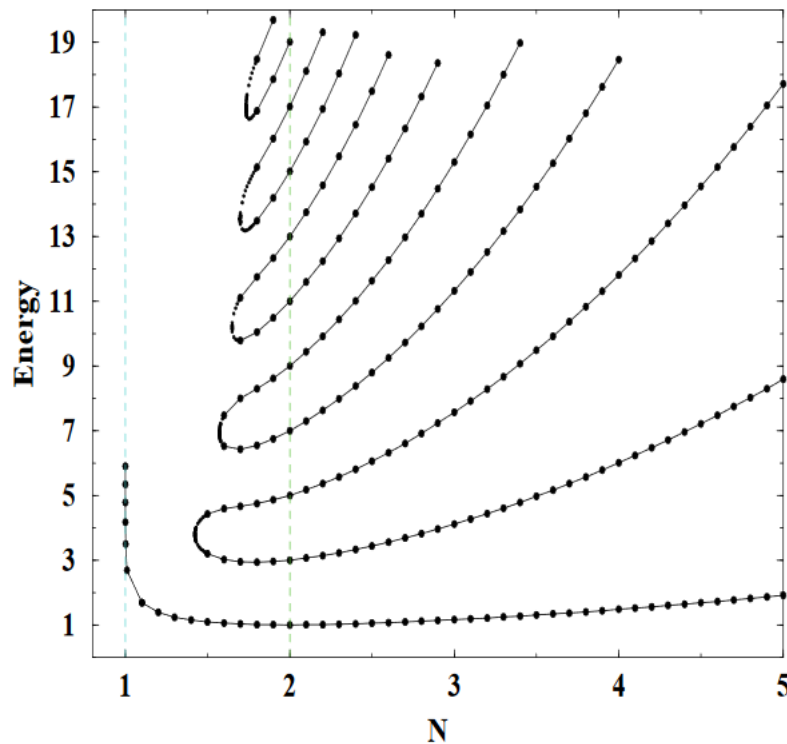


Figure 18: Real energy eigenvalues of the Hamiltonian $H = p^2 - (ix)^N$. For $N \geq 2$ there are an infinite number of real energies, with $N=2$ corresponding to the simple harmonic oscillator spectrum, whereas for $N < 2$ there are only a finite number. As N decreases, the number of real energies decreases until only the ground state remains, which itself diverges as $N \rightarrow 1$. [1]

What they found was that for $N \geq 2$, there were an infinite number of real energy eigenvalues for the system, i.e. it looked Hermitian. However, when $1 < N < 2$ they found that the number of real energies became finite and decreased as N was lowered until only the ground

state remained. The energy of the ground state then diverged as $N \rightarrow 1$. The fact that these rather bizarre potentials (such as $V(x) = ix^3$) could have real energy eigenvalues called the necessity of Hermiticity into question. They then realised that the strange Hamiltonians they had been studying all had the property that $H(x) = H^*(-x)$, or more famously: $V(x) = V^*(-x)$ (as the p^2 operator is already has this symmetry). This condition became the definition of what is known today as PT symmetry. The basic idea behind PT symmetry is that if any loss in the system is spatially balanced with an equivalent amount of gain, then the effect of the loss will be cancelled out and the system's energy eigenvalues will be real (at least some of time). Carl Bender argues that this is a more physical condition than the more abstract, mathematical condition of Hermiticity [72]. PT symmetric systems can have real eigenvalues but differ from Hermitian systems in several important ways; the most obvious is that PT symmetric systems have two distinct phases when an external parameter (e.g. frequency or gain/loss parameter) is tuned: an unbroken PT phase, where eigenvalues are real, and a broken PT phase, where some eigenvalues form complex conjugate pairs. We can see these two phases in Bender's $H = p^2 - (ix)^N$ system. For $N \geq 2$ we have all real energies so we are in the unbroken PT phase. As N decreases from two, the energies start becoming complex and at $N = 1$ the energies all complex with the exception of the diverged ground state, so the region of $N < 2$ is our PT broken phase.

These broken and unbroken phases are separated by an exceptional point; a special kind of mode degeneracy that cannot occur in Hermitian systems, where a pair of eigenvalues and their associated eigenvectors coalesce simultaneously. Exceptional points have been studied in many systems, such as quantum mechanics, where they can be linked to level repulsion and quantum chaos [73], semiconductor physics where exciton-polaritons (strongly interacting

photon/electron-hole pairs) can exhibit exceptional points in their spectra [74], microwave cavities, where an exceptional point in the energy eigenvalues can be seen when the coupling between two resonances and the level of one of the resonances is tuned [75] (this exceptional point was also shown to have a chiral property, where encircling the exceptional point in parameter space gave a non-zero phase shift between the eigenvectors, which has been confirmed in another experiment [76] and has received theoretical analysis [77]) and in laser physics where an exceptional point in the lasing modes for two lasers with unequal pump powers can lead to strange behaviour such as decreasing output intensity for increasing pump power and the suppression of lasing in one of the lasers, even though it has enough supplied power to lase [78] (this is somewhat similar to a time-reversed version of passive PT symmetry, which we will discuss later in this chapter). In the context of PT symmetry, exceptional points have been linked to a number of interesting phenomena, such as mode selection in ring lasers (see Figure 21) [79], mode coalescence in coupled, PT-symmetric waveguides [80], coalescence of polarization eigenstates [82], unidirectional zero reflection [83,84] and unidirectional invisibility [89]. Going back to Bender's previously discussed system, we see that this crossover point occurs when $N = 2$.

To clarify what we mean by an exceptional point: if we have an arbitrary 2x2 matrix $[A] = \begin{pmatrix} A_{11} & A_{12} \\ A_{21} & A_{22} \end{pmatrix}$ then its eigenvalues are $\frac{1}{2}(A_{11} + A_{22} \pm \sqrt{4A_{12}A_{21} + (A_{11} - A_{22})^2})$ with corresponding eigenvectors $\left(\frac{A_{11} - A_{22} \pm \sqrt{4A_{12}A_{21} + (A_{11} - A_{22})^2}}{2A_{21}}, 1 \right)^T$. So, we can see that when $\sqrt{4A_{12}A_{21} + (A_{11} - A_{22})^2} = 0$ we will have both degenerate eigenvalues and degenerate eigenvectors. This degeneracy of both eigenvalues *and* eigenvectors is what is known as an exceptional point. If $[A]$ is Hermitian, so that A_{11} and A_{22} are real numbers and A_{21} and A_{12}

are purely imaginary (and negatives of each other), then we clearly cannot have an exceptional point as the quantities $4A_{12}A_{21}$ and $(A_{11} - A_{22})^2$ will both be positive, real numbers. To take an appropriate example, if we look at a reciprocal scattering matrix for a single polarization (so we have $[S] = \begin{pmatrix} t & r_b \\ r_f & t \end{pmatrix}$), we can see that its eigenvalues are $t \pm \sqrt{r_f r_b}$ with eigenvectors $\left(\pm \frac{\sqrt{r_b}}{\sqrt{r_f}}, 1\right)^T$. This means that when either r_f or r_b is zero, both the eigenvalues and eigenvectors will coalesce and we will have an exceptional point. It is important to note that having either $r_f \rightarrow 0$ and $r_b \neq 0$ or $r_b \rightarrow 0$ and $r_f \neq 0$ is not the same as $r_f = r_b \rightarrow 0$ (i.e. impedance matching). If both reflections are the same, then the eigenvectors will always be $(\pm 1, 1)^T$, so there will be degeneracy in the eigenvalues but not the eigenvectors and so no exceptional point. It is important to note here that the link between unidirectional zero reflection and an exceptional point in the scattering matrix are reliant upon our choice of convention. If we had chosen the more standard convention for the scattering matrix, where $[S] = \begin{pmatrix} r_f & t_b \\ t_f & r_b \end{pmatrix}$, then an exceptional point would correspond to unidirectional zero transmission (i.e. $t_f = 0$ with $t_b \neq 0$ or $t_b = 0$ with $t_f \neq 0$). The benefit of choosing our current convention for the scattering matrix, aside from the link between unidirectional zero reflection and exceptional points, is that it allows us to make simple connection between it and our Hamiltonian (the $[C]^{-1}$ matrix).

Another consequence of replacing Hermiticity with PT symmetry is that the orthogonality condition for eigenvectors/modes in Hermitian systems (i.e. $\int \psi_i \psi_j d\mathbf{r} = \delta_{ij}$, where δ_{ij} is the Kronecker delta) is not applicable in PT symmetric systems, which can lead to interesting behaviour such as power oscillation (see Figure 19 (b)). PT symmetry is valuable in the context

of optics as it implies that if the losses inherent in many optical components can be balanced with an appropriate amount of the gain, then we should be able to have a system which is approximately Hermitian and also has the added bonus of an exceptional point.

4.2. PT Symmetry in Quantum Mechanics and the Link to Optics:

Enforcing PT symmetry on the Schrödinger equation means that we swap the wavefunction with its PT symmetric counterpart, then see what condition the Hamiltonian must satisfy in order for the wave equation to maintain the same form. To clarify, what we mean by a Hamiltonian is a function (or set of functions) which describe how one or more states evolve in time or along a propagation direction. For example, in quantum mechanics the Hamiltonian describes the evolution of a system over time, via the Schrödinger equation:

$$i\hbar \frac{\partial}{\partial t} \psi(\mathbf{r}, t) = H(\mathbf{r}, t) \psi(\mathbf{r}, t) \quad (4.1)$$

Where (in the non-relativistic case) the Hamiltonian is given by $H = -\frac{\hbar^2}{2m} \nabla^2 + V(\mathbf{r}, t)$. The parity will flip the sign of the del operator and change the sign of the argument in the potential (i.e. $\nabla \rightarrow -\nabla$ and $V(\mathbf{r}, t) \rightarrow V(-\mathbf{r}, t)$). Time reversal will also flip the sign of the del operator (as it is technically a momentum operator), change the sign of the time argument of the potential and complex conjugate everything (i.e. $\nabla \rightarrow -\nabla$, $V(\mathbf{r}, t) \rightarrow V(\mathbf{r}, -t)$ and $V(\mathbf{r}, t) \rightarrow V^*(\mathbf{r}, t)$). Combining these operations, we see that if we transform $\psi(\mathbf{r}, t)$ via PT symmetry then to have the wave equation look the same, we need the potential to satisfy $V(\mathbf{r}, t) = V^*(-\mathbf{r}, -t)$. For many systems, the potential will not vary in time, so the condition of PT symmetry is more commonly written as $V(\mathbf{r}) = V^*(-\mathbf{r})$. Although this condition is

mathematically simple, its realisation in quantum mechanics is not easy as perfectly matching the absorption (loss) and injection of particles into the system (gain) is difficult. The first attempts to realise PT symmetry in experiment were based on the idea that the Schrödinger equation has a very similar form to the paraxial approximation of the Helmholtz equation. For propagation in the z direction, this can be written as:

$$2ik_0 \frac{\partial E}{\partial z} = -\frac{\partial^2 E}{\partial x^2} - k_0^2(n^2 - 1)E \quad (4.2)$$

with the $\partial/\partial t$ replaced by a $\partial/\partial z$ and the potential $V(\mathbf{r}, t)$ replaced by $n(\mathbf{r})^2 - 1$. This equation assumes that only small angle scattering occurs and that the refractive index varies slowly on the scale of a wavelength. This lead to the idea that the 1D quantum mechanical condition of PT symmetry of $V(\mathbf{r}) = V^*(-\mathbf{r})$ could be translated into electromagnetism as $n(\mathbf{r}) = n^*(-\mathbf{r})$. This lead to observation of PT symmetry breaking in a two-waveguide system in 2009 [93] using a modified, passive potential (see 4.6 for discussion on this passive PT symmetry) and then in a fully PT symmetric system which included gain shortly after in 2010 [80].

Although most definitions of PT symmetric systems are based on conditions on the potential, it is also interesting to see what effect PT symmetry will have on the scattering matrix. By using the definition of the scattering matrix and transforming the ingoing/outgoing fields, we can derive a link between a scattering matrix and its PT symmetric counterpart:

$$\begin{pmatrix} c \\ b \end{pmatrix} = [S] \cdot \begin{pmatrix} a \\ d \end{pmatrix} \xrightarrow{PT} \begin{pmatrix} a^* \\ d^* \end{pmatrix} = [S] \cdot \begin{pmatrix} c^* \\ b^* \end{pmatrix} \quad (4.3)$$

So a PT symmetric scattering matrix will obey

$$[S] \cdot [S]^* = I \quad (4.4)$$

where I is the identity matrix. We can use this condition to relate the eigenvalues of the scattering matrix to each other by $\sigma_1 = 1/\sigma_2^*$, so they will have reciprocal magnitudes. A new conservation law based on the reflection and transmission coefficients can also be derived from this condition. In a Hermitian system, the sum of the energies of the output must be equal to the sum of the energies of the input (i.e. energy is conserved). This can be quantified as $|t|^2 + |r_f|^2 = |t|^2 + |r_b|^2 = 1$. In a PT symmetric system, however, this is no longer true.

Instead, there is a similar yet subtly different condition of $||t|^2 - 1| = \sqrt{|r_f|^2 |r_b|^2}$. This implies that when either (or both) of the reflections are zero, then the transmission coefficient must be one.

Now that we know a bit more about how to define a PT symmetric system, we will look at some of the ways in which PT symmetric systems are realised. In the following, the terms “perpendicular” and “tangential” refer to the orientation of the mirror plane normal with respect to the propagation direction.

4.3. Perpendicular PT Symmetry:

The early studies of PT symmetry in optics involved a parity operator whose mirror plane normal was perpendicular to the direction of propagation. This is what we call “perpendicular PT symmetry”. The simplest (and most studied) example of this kind of PT symmetry is that of two waveguides both with a real mode index of α where one is constructed with gain and one with loss (quantified by γ), and are coupled to each other by some constant, g . Our wave equation in this case has a Hamiltonian of the form

$$[H] = \begin{pmatrix} \alpha + i\gamma & g \\ g & \alpha - i\gamma \end{pmatrix} \quad (4.5)$$

Where the propagation of the fields inside the waveguide (a_1 and a_2) is described by

$$-i \frac{\partial}{\partial z} \begin{pmatrix} a_1 \\ a_2 \end{pmatrix} = k_0 [H] \cdot \begin{pmatrix} a_1 \\ a_2 \end{pmatrix} \quad (4.6)$$

It is interesting to note that the above equation is remarkably similar to the time-dependent Schrödinger equation we saw earlier. This is because when we are dealing with light we can make the transformation $z = ct$ which implies that we can set $\partial_z \rightarrow c\partial_t$. We can see that if we take our parity operator as being in-between the waveguides (say, in the x direction), then our condition of $n(x) = n^*(-x)$ is satisfied because $\alpha + i\gamma = (\alpha - i\gamma)^*$. Calculating the eigenvalues of this Hamiltonian (which can be interpreted as propagation constants) will give us $\alpha \pm \sqrt{g^2 - \gamma^2}$ with corresponding eigenvectors of $\left((i\gamma \pm \sqrt{g^2 - \gamma^2})/g, 1 \right)^T$. We see that if $g > \gamma$ then the eigenvalues are purely real, so we have lossless propagation and our system looks approximately Hermitian. We say approximately as the system can still display some odd behaviour, such as power oscillation due to the non-orthogonality of the waveguide modes. In a Hermitian system, we expect the power of the propagating beam to be conserved, more precisely, we say that for a 2D system described by a propagating direction z and transverse coordinate x , then the integrated power: $\int_{-\infty}^{\infty} |U(x, z)|^2 dx$ (where $U(x, z)$ is the field profile) is constant for any value of z . In a PT symmetric system this is no longer true as we have gain and loss to consider and so we must use a modified conserved quantity [81]: $\int_{-\infty}^{\infty} U(x, z) U^*(-x, z) dx$. This quantity is referred to as the “quasi-power” and allows the actual power in the waveguides to oscillate as the beam propagates. This can be seen in Figure 19 (b), which shows the simulated field pattern of a PT symmetric waveguide below the

threshold. The smearing of the field pattern compared to the conventional (Hermitian) system is due to this power oscillation.

If $g < \gamma$, however, then the eigenvalues are a pair of complex conjugates, so one of the waveguides will have a positive imaginary part in its index (loss) and one will have a negative imaginary part (gain). This means that one of the waveguides (the one with gain) will have an amplifying mode and the other (with loss) will have a decaying mode. We can see this in Figure 19 (c), where the field pattern for the broken PT system is dominated by the amplified mode, regardless of the input channel.

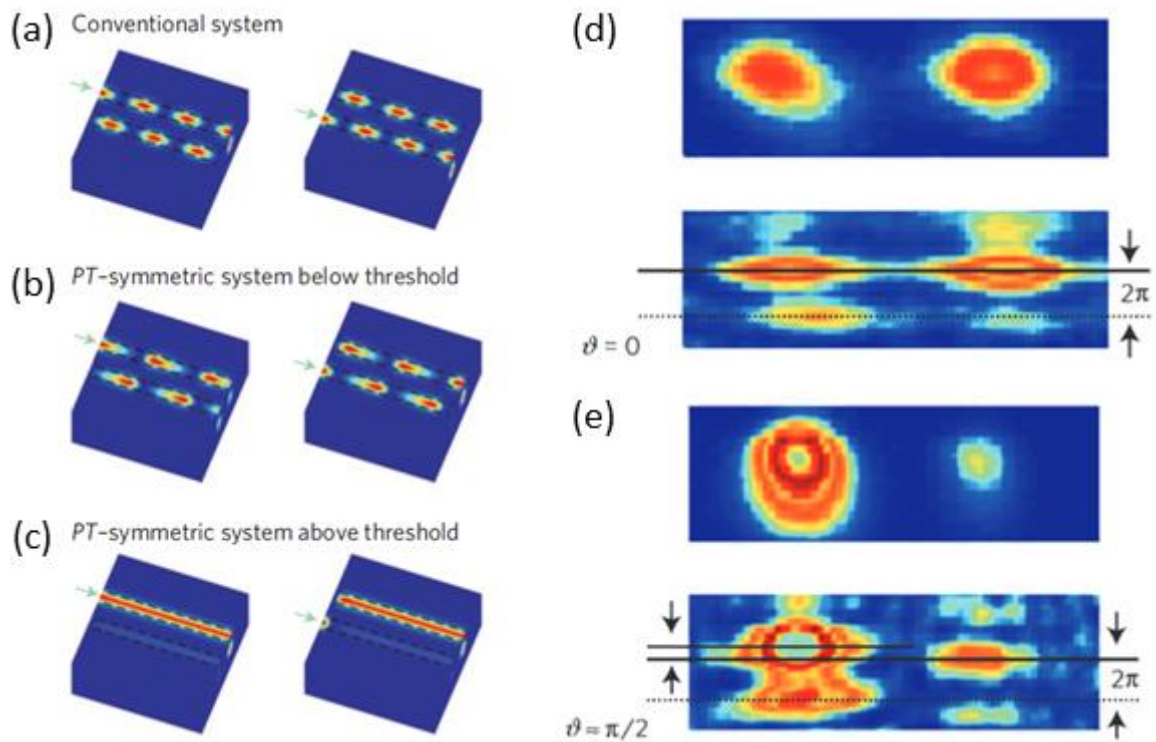


Figure 19: Modes in a coupled PT waveguide system. (a), (b) and (c) show simulated electric field patterns for the system at different operating regimes, with (a) being the Hermitian system with no gain or loss, (b) being where the system contains balanced gain and loss but is operated below the exceptional point and (c) is the PT symmetric system operating above the exceptional point. (d) and (e) show the intensity plot (upper panels) and phase profile (lower panel) of the eigenstates of the Hermitian system (d) and the PT symmetric system operated above the exceptional point in the broken phase. Images taken from [80].

The crossover point for these two behaviours ($g = \gamma$) is called an exceptional point. Here, the eigenvalues are both α , similar to the standard waveguide case of $\gamma = 0$ and $g = 0$ except that the eigenvectors are both $(i, 1)$, which means that propagating fields inside the waveguides are $\pi/2$ out of phase. This phase relation between the two channels also extends to the broken PT phase. This is because the two eigenvectors will take the form of $(i(\gamma \pm \sqrt{\gamma^2 - g^2}), 1)$ at and above the exceptional point, fixing the phase between the two channels at $\pi/2$. Experimental observation of this can be seen in Figure 19 (e), where the maxima of the phase of the two channels are shifted by $\pi/2$.

There are many examples of proposed devices that take advantage of the rich behaviour of this perpendicular PT symmetry, such as demultiplexing waveguides [85], plasmonic waveguides [86] and enhanced non-reciprocal couplers (using non-linearity) [87].

4.4. Tangential PT Symmetry:

Another example of PT symmetry which is more related to the type of propagation we are considering is where the parity reflection plane normal is tangential to the propagation direction. As an example, we will look at a subwavelength stacked slab system, which we can analyse using the effective medium mixing formula described in section 3.2. If we consider two, non-magnetic slabs (i.e. $\mu = 1$) of thickness d , we can make this system PT symmetric by choosing their permittivities to be $\alpha + i\gamma$ and $\alpha - i\gamma$, our effective medium tensor (via equation 3.19) is then $\begin{pmatrix} a & -k_0 d\gamma/4 \\ k_0 d\gamma/4 & 1 \end{pmatrix}$. Taking eigenvalues of this, we again see that the eigenvalues can be separated into two categories: when $2(a - 1) > k_0 d\gamma$, we have real

eigenvalues and our system looks Hermitian but when $2(\alpha - 1) < k_0 d \gamma$ we get a pair of complex conjugate eigenvalues. In this case, the exceptional point corresponds to a unidirectional zero reflection property (i.e. $r_f = 0$, $r_b \neq 0$). We can explore this further by looking at the eigenvalues of the scattering matrix and the constitutive matrix for the system when $k_0 d = 0.4$ and $\alpha = 2$. Figure 20 (a) and (b) show parametric plots of the scattering matrix (σ_j) and constitutive matrix (λ_j) as the gain/loss parameter (γ) is varied. For small γ , σ_j (red and blue lines in (a)) will lie on the unit circle (black line in (a)) and λ_j (red and blue lines in (b)) will be purely real, indicating that we have an approximately Hermitian system and that we are in the unbroken PT phase. Once the gain/loss parameter is increased to a certain point ($\gamma = 3.86$), the σ_j and λ_j coalesce to an exceptional point and then split. After this splitting, we can see that the σ_j form another circle with one side being within the unit circle (lossy mode) and one side being outside it (gain mode).

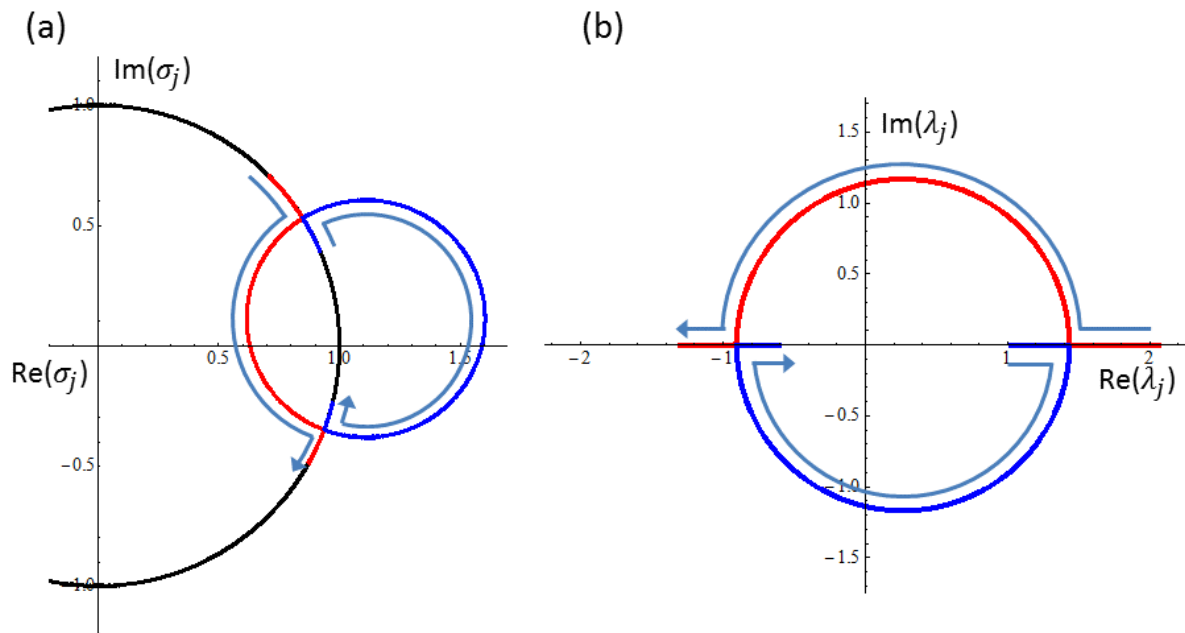


Figure 20: Eigenvalue plots for an example longitudinal PT symmetric system. Parametric plots of the scattering matrix (a) and constitutive matrix (b) eigenvalues (σ_j and λ_j , respectively) for a two-slab system where $\epsilon_1 = 2 + i\gamma$, $\mu_1 = 1$, $\epsilon_2 = 2 - i\gamma$, $\mu_2 = 1$ and $k_0 d = 0.4$, where γ is varied from 0 to 19 and the light blue arrow show the direction of increasing γ . The black circle in (a) is the unit circle and the red and blue lines represent the eigenvalues corresponding to the loss and gain modes of the system (respectively).

We can see similar behaviour in the λ_j , where complex conjugate pairs are formed after the exceptional point, one with positive imaginary part (lossy mode) and the other with negative imaginary part (gain mode). In this regime, we have an obviously non-Hermitian system and so we are in the broken PT phase. If we continue increasing γ then we find that there is actually a second exceptional point (at $\gamma = 18.8$) where the eigenvalues coalesce again and the system re-enters the unbroken PT phase. This multiple exceptional point property has also been observed in other tangential PT symmetric systems [88]. Although this system is not very subwavelength (and so we cannot view $[C]^{-1}$ as the effective medium of the system), we still see the real to complex conjugate splitting behaviour in the eigenvalues, further evidencing that we can treat $[C]^{-1}$ as a Hamiltonian.

This kind of PT symmetry can result in structures which have unidirectional invisibility [89, 90], tunnelling properties [91] and has been studied in the context of Bragg grating assisted directional couplers, which can be used in switching devices [92].

4.5. Azimuthal PT Symmetry:

In 2014, there was a paper published in Science [79], in which the researchers designed a structure based on another kind of PT symmetry to investigate how PT symmetry might be applicable to lasing systems. These structures were rings and the parity operator used was that of azimuthal parity in cylindrical coordinates. A schematic of the structure can be seen in Figure 21 a), where the light blue material is a InP substrate, the purple ring is an InGaAsP gain medium and the gold material is a Cr/Ge composite that acts as the loss modulator. When

they compared the spectrum of the gain+loss ring to that of the pure gain ring, they found that the multiple peaks in the spectrum of the pure gain ring (due to the multiple solutions corresponding to the boundary condition of $E(r, \phi) = E(r, \phi + 2\pi)$ that lie within the gain spectrum of InGaAsP) reduced to a single peak in the spectrum of the gain+loss ring. The wavelength of this peak was found to coincide with the lattice constant of the PT symmetry (i.e. the total circumference of the ring divided by number of gain/loss pairs in the ring). To confirm this, they fabricated two samples, one with order 53 and the other with order 55. They found that in both cases the lasing wavelength corresponds to the PT lattice length, showing that PT symmetry could have applications in lasing.

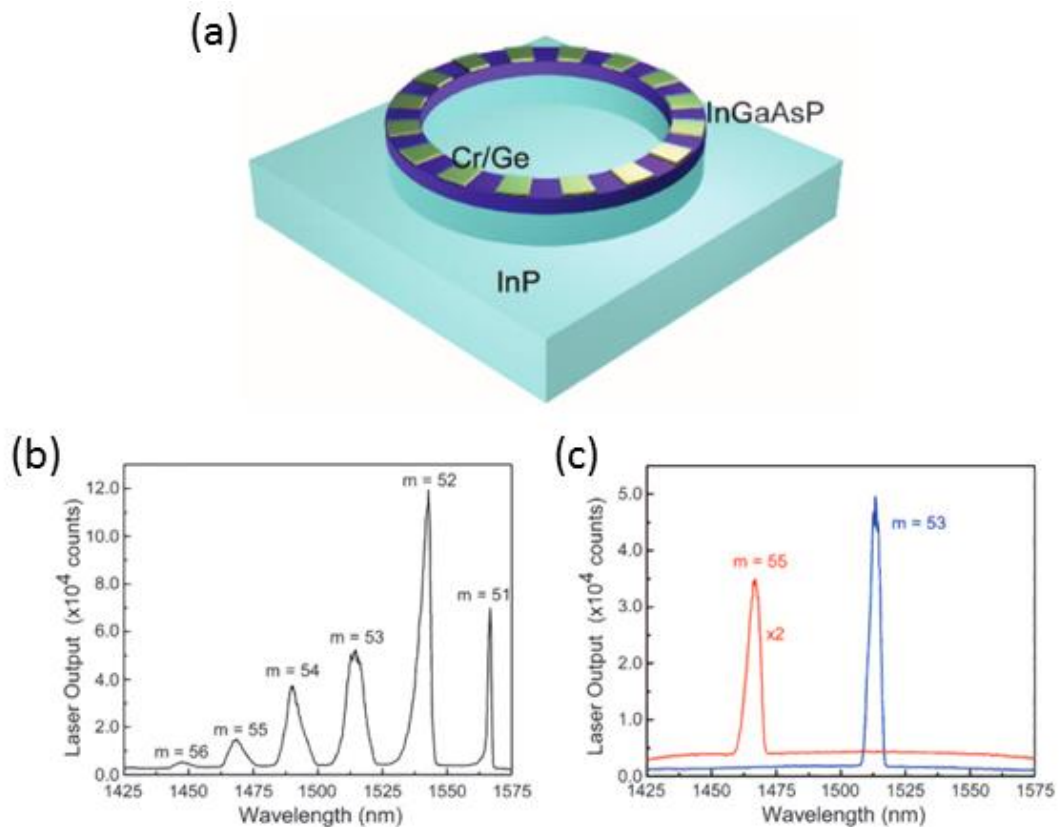


Figure 21: Schematic and spectrum of a microring laser. (a) shows a schematic of the ring structure. The light blue material is an InP substrate, the purple ring is the InGaAsP gain medium and the gold sections are Cr/Ge structures which introduce the modulated loss needed for PT symmetry. (b) and (c) show the output of the laser without the lossy Cr/Ge structures (b) and with them (c). The red and blue curves in c) are the spectra of two different ring lasers with different azimuthal orders.

4.6. PT Symmetry Without Gain:

So far, we have been looking at exact PT symmetry, where the amounts of gain and loss in the system are balanced. However, it is actually still possible to have an exceptional point when there is no gain in the system. To see why, we will revisit equation 4.5 and see what happens when we do not balance the loss with gain. This time we set up our coupled waveguide with two lossy terms:

$$-i \frac{\partial}{\partial z} \begin{pmatrix} a_1 \\ a_2 \end{pmatrix} = k_0 \begin{pmatrix} \alpha + i\gamma_1 & g \\ g & \alpha + i\gamma_2 \end{pmatrix} \begin{pmatrix} a_1 \\ a_2 \end{pmatrix} \quad (4.7)$$

where γ_1 and γ_2 are both positive. Taking the eigenvalues of this system, we can see that they are now given by $\alpha + \frac{i(\gamma_1 + \gamma_2)}{2} \pm \sqrt{g^2 - \frac{(\gamma_1 - \gamma_2)^2}{4}}$, so it appears that an exceptional point is still possible. Interestingly, if we make the transformation of $(\gamma_1 - \gamma_2)^2 = 4\gamma^2$, where γ can be interpreted as our original gain loss parameter, then the condition for an exceptional point is the same as in the ideal case with matched gain and loss. In fact, aside from an additional $i(\gamma + \gamma_2)$ loss term in the eigenvalues, the system's exceptional and eigenvalue behaviour will be the same.

In the case of the coupled waveguides, the link between the active and passive PT systems is a simple exponential factor in the electric fields. For example, if we look at the eigenvalues of the active system described in equation 4.4 and the passive system in equation 4.6, we see that if the correct transformation is made ($\gamma_2 \rightarrow 2\gamma + \gamma_1$) then the two sets of eigenvalues (or propagation constants), β_i , are related by a purely imaginary term: $\beta_{i \text{ passive}} = \beta_{i \text{ active}} + i(\gamma + \gamma_1)$. This implies that the electric fields in the two systems are related through an exponential factor: $a_{i \text{ passive}} = e^{-k_0(\gamma + \gamma_1)z} a_{i \text{ active}}$. In more complex systems where multiple

reflections have to be considered, there is no simple link between the active and passive systems. However, by assuming $k_0 d \ll 1$ and using the effective medium equations we can approximate a diagonal term bias in the constitutive matrix, $[C]^{-1} \rightarrow [C]^{-1} + i\gamma[I]$, via a multiplication of the scattering matrix by an exponential factor: $[S] \rightarrow e^{-k_0 d \gamma} [S]$.

This linkage means that we can use entirely passive structures to realise PT-like exceptional points, as long as we can appropriately tune the contrast between the lossy elements. This passive PT symmetry has proven to be very popular in experimental realisations of PT symmetry, as it allows exceptional points to be seen in the lab without needing to consider complex gain mechanisms. These realisations include transversely coupled waveguide systems (a lossy version of the system described in Figure 19) [93], a coherent perfect absorber with a PT phase transition [94], PT symmetric states in a microwave cavity [95] and a tangential, passive PT waveguide displaying unidirectional zero reflection [96].

4.7. Parity Redefinition via a Gauge Transformation:

The huge variety of potentials made possible by metamaterials can provide a way of exploring the effects of many kinds of symmetry. We have seen the effects of standard PT symmetry in the previous chapters but are there other choices of P that we can use to design a system? The modification of parity operators is something that has precedent in other fields, such as particle physics and quantum field theory, where a parity “redefinition” is used to model states that pick up a phase factor under a parity operation (e.g. [97] or [98]). This implies that, as long as our new parity operator satisfies all the usual requirements of a parity operator: that

it is Hermitian, unitary and involutory (i.e. it is its own inverse), then we can use it as a new symmetry operator.

In light of this, we seek a transformation on our effective medium parameters that corresponds to the shifting of the S parameter middle plane. If we define a shift in the positive z direction by a shift distance by L , then the shifted forwards/backwards propagating fields are given by

$$\begin{pmatrix} E_x^+ \\ E_y^+ \\ E_x^- \\ E_y^- \end{pmatrix} \rightarrow \begin{pmatrix} e^{i\phi_L} & 0 & 0 & 0 \\ 0 & e^{i\phi_L} & 0 & 0 \\ 0 & 0 & e^{-i\phi_L} & 0 \\ 0 & 0 & 0 & e^{-i\phi_L} \end{pmatrix} \cdot \begin{pmatrix} E_x^+ \\ E_y^+ \\ E_x^- \\ E_y^- \end{pmatrix} \quad (4.8)$$

Where $\phi_L = kL$. Using our $[B]$ matrix to convert to \mathbf{E}/\mathbf{H} basis, we can show that the above transformation is equivalent to

$$\begin{pmatrix} E_x \\ E_y \\ H_x \\ H_y \end{pmatrix} \rightarrow \begin{pmatrix} \cos(\phi_L) & 0 & 0 & i \sin(\phi_L) \\ 0 & \cos(\phi_L) & -i \sin(\phi_L) & 0 \\ 0 & -i \sin(\phi_L) & \cos(\phi_L) & 0 \\ i \sin(\phi_L) & 0 & 0 & \cos(\phi_L) \end{pmatrix} \cdot \begin{pmatrix} E_x \\ E_y \\ H_x \\ H_y \end{pmatrix} = [U] \cdot \begin{pmatrix} E_x \\ E_y \\ H_x \\ H_y \end{pmatrix} \quad (4.9)$$

And so our parity operator becomes

$$\begin{aligned} [P_z] &\rightarrow [U]^{-1} \cdot [P_z] \cdot [U] \\ &= \begin{pmatrix} \cos(2\phi_L) & 0 & 0 & i \sin(2\phi_L) \\ 0 & \cos(2\phi_L) & -i \sin(2\phi_L) & 0 \\ 0 & i \sin(2\phi_L) & -\cos(2\phi_L) & 0 \\ -i \sin(2\phi_L) & 0 & 0 & -\cos(2\phi_L) \end{pmatrix} \end{aligned} \quad (4.10)$$

As well as satisfying the conditions of Hermiticity and involutory, we observe that this new parity operator is a unitary matrix, so the eigenvalues of a matrix (e.g. $[C]^{-1}$) will not change under this transformation. This means that for some PT symmetric $[C]^{-1}$ containing an

exceptional point, we can apply this transformation and find another $[C]^{-1}$ which also has an exceptional point.

If we take a 2x2 reciprocal constitutive matrix (i.e. $\zeta = -\xi$) and insist that our system is symmetric with respect to the combination of this new parity operator and the time reversal operator, then our new conditions on the constitutive parameters are given by:

$$\begin{aligned}
\epsilon(z) &= \frac{1}{2}(\epsilon^*(-z) + \mu^*(-z)) \\
&\quad + (\epsilon^*(-z) - \mu^*(-z)) \cos(4\phi_L) - 2i\xi^*(-z) \sin(4\phi_L) \\
\mu(z) &= \frac{1}{2}(\epsilon^*(-z) + \mu^*(-z)) \\
&\quad + (\mu^*(-z) - \epsilon^*(-z)) \cos(4\phi_L) + 2i\xi^*(-z) \sin(4\phi_L) \\
\xi(z) &= \xi^*(-z) \cos(4\phi_L) + \frac{1}{2}i(\epsilon^*(-z) - \mu^*(-z)) \sin(4\phi_L)
\end{aligned} \tag{4.11}$$

One can get the equivalent condition on the effective medium parameters by simply removing the z -dependence. We now have a family of PT symmetry conditions lying in the ϕ_L range of 0 to $\pi/2$. In general, this is obviously a rather complicated condition but there is an interesting (and non-trivial) example of is when $kL = \pi/4$. In this case, acting the parity operator on our (E_x, H_y) basis is equivalent to setting $E_x \rightarrow iH_y$ and $H_y \rightarrow -iE_x$, similar to the electromagnetic dual symmetry. Indeed, when we set $kL = \pi/4$ in the above equations, we get that $\epsilon(z) = \mu^*(-z)$, $\xi(z) = -\xi^*(-z)$, which is again similar to the dual symmetry condition that a system is invariant if the electric and magnetic fields and the permittivity and permeability are swapped. If we enforce this condition on a constitutive matrix, then it should have the form

$$[C_{\pi/4}]^{-1} = \begin{pmatrix} a + i\gamma & i\kappa \\ -i\kappa & a - i\gamma \end{pmatrix} \quad (4.12)$$

Another example is taking $kL = \pi/8$, where enforcing invariance will result in a constitutive matrix of the form.

$$[C_{\pi/8}]^{-1} = \begin{pmatrix} a + b + i\gamma & -\gamma - ib \\ \gamma + ib & a - b - i\gamma \end{pmatrix} \quad (4.13)$$

The conditions in equation 4.10 are a continuous function of the shifting phase, so we technically have an infinite number of them.

It is important to note that the PT symmetry conditions we are deriving for $[C]^{-1}$ are only concerned with relating the \mathbf{E}/\mathbf{H} fields on either side of a medium. In the classical, continuous PT symmetric systems where we have, for example, $\epsilon(z) = \epsilon^*(-z)$, the fields will automatically be PT symmetric for all z . When we work with an effective medium, however, we do not require the internal potential to satisfy any kind of exact spatial profile. For example, we can take a simple stacked slab system and set the depth of the slabs to be unequal: $d_1 = fd$ and $d_2 = (1 - f)d$, where f is the filling fraction of the first slab and is confined to the range $0 < f < 1$. In this case, the effective medium of the two slabs is given by

$$[C_{eff}]^{-1} = \begin{pmatrix} f\epsilon_1 + (1 - f)\epsilon_2 & \frac{ik_0df(1 - f)}{2}(\epsilon_1\mu_2 - \epsilon_2\mu_1) \\ -\frac{ik_0df(1 - f)}{2}(\epsilon_1\mu_2 - \epsilon_2\mu_1) & f\mu_1 + (1 - f)\mu_2 \end{pmatrix}. \quad (4.14)$$

This means that, in some cases, we can break from exact spatial gain/loss symmetry in the slabs but still have a PT-symmetric $[C]^{-1}$. To give a specific example, we can take the $\epsilon_1 = \epsilon_2^*$ system we looked at earlier and set $d_1 = 3d/4$ and $d_2 = d/4$. Using the old parameters of

$\epsilon_1 = a + i\gamma, \epsilon_2 = a - i\gamma$ and $\mu_1 = \mu_2 = 1$ will no longer yield a PT symmetric constitutive matrix or an exceptional point. However, we can use the above effective medium equation to see that we will have a PT symmetric $[C]^{-1}$ if we set $\epsilon_1 = a + i\gamma, \mu_1 = 1, \epsilon_2 = 3(a - i\gamma)$ and $\mu_2 = 3$. This implies that it is actually the integrated constitutive parameters of individual elements that are important (i.e. their $[Y]$ matrix components), not just the constitutive parameters themselves.

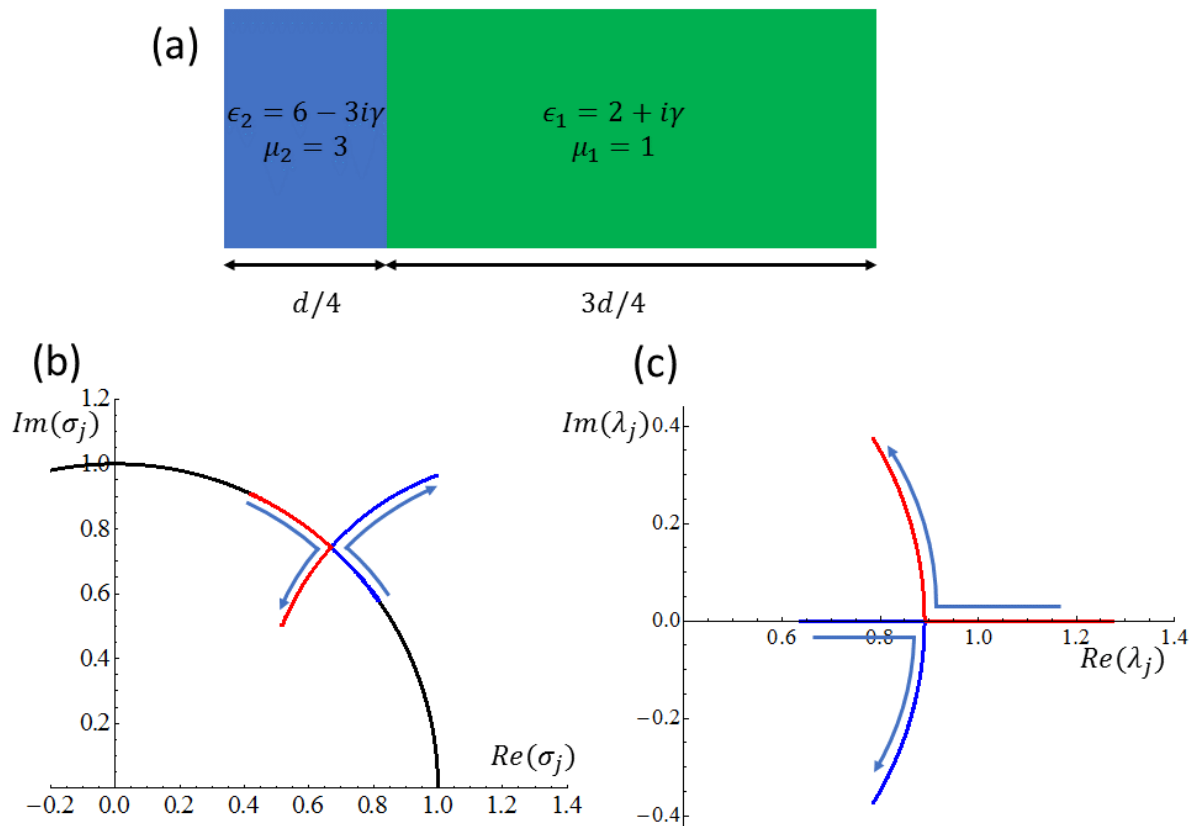


Figure 22: PT exceptional point in system with non-symmetric but matched gain/loss profile. (a) shows an illustration of the non-symmetric system. The constitutive parameters of the second slab have been multiplied by 3 to account for its smaller size and so balance out the gain and loss. Eigenvalues of the $[S]$ matrix (σ_j) and $[Y]$ matrix (λ_j) are plotted in figures (b) and (c) (respectively), where we have set $a = 2$ and $k_0 d = 0.4$ and we have varied γ from 0 to 4. The σ_j show the unit circle to reciprocal splitting behaviour we have seen in previous PT symmetric systems. The λ_j also show similar real to complex conjugate splitting behaviour to that which we have seen previously.

We confirm this numerically by looking at the $[S]$ matrix and $[Y]$ matrix eigenvalues, using the parameters described above, when we set $a = 2$ and $k_0 d = 0.4$ and vary γ . Figure 22 (a)

shows an illustration of the system. The $[S]$ matrix eigenvalues (σ_j) are shown in Figure 22 (b) when we vary γ from 0 to 4. We can see that the σ_j initially trace out a unit circle until a critical value of γ is reached ($\gamma \sim 2.5$), then the σ_j split off and form another circle where two points for a certain γ will have reciprocal moduli. The $[Y]$ matrix eigenvalues (λ_j) also show familiar behaviour as γ is tuned, which can be seen in Figure 22 (c). The λ_j start off as two real numbers then come together and coalesce at the exceptional point, after which they split off to form complex conjugates. Based on this, can see that even if we don't have a system with the classical condition $\epsilon(x) = \epsilon^*(-x)$, we can still get a PT symmetric $[C]^{-1}$ and an EP if we appropriately tune the gain/loss potential. So, it would appear that when we treat a system as a black box, we lose the need for any specific spatial gain/loss profile to achieve ideal PT symmetry. We only require the average of the gain and loss to be zero.

4.8. Unidirectional Zero Reflection and the Link to PT Symmetry:

We have seen that tangentially PT symmetric systems contain exceptional points which result in unidirectional zero reflection but can we make the converse statement: that systems with unidirectional zero reflection are PT symmetric? To do this, we must examine the constitutive parameters which can give rise to an exceptional point. The condition for an exceptional point in a reciprocal system, in terms of the constitutive matrix, is given by $\epsilon - \mu = \pm 2\xi$. This is not particularly useful on its own but we can combine it with our gauging operation to uncover the symmetry in $[C]^{-1}$. If we can gauge the constitutive matrix, by setting $[C]^{-1} \rightarrow [U].[C]^{-1}.[U]^{-1}$, to have $\text{Re}(\epsilon) = \text{Re}(\mu)$, this means that at the exceptional point we also

have $\text{Re}(\xi) = 0$, as $\epsilon - \mu$ must be a purely imaginary number. This is remarkably similar to the shifted PT symmetry condition when $kL = \pi/4$ (equation 4.11). We also know that unidirectional zero reflection (UZR) can occur in passive systems as well and that an ideal PT symmetric system can be biased into a passive one while retaining its exceptional point. This means that for a system with UZR, we can write that

$$[U] \cdot [C]^{-1} \cdot [U]^{-1} = [C_{PT}]^{-1} + i\gamma_{bias}[I] \quad (4.15)$$

where the $i\gamma_{bias}[I]$ term is the diagonal bias discussed previously. This means that if we can prove that a system can simultaneously have $\text{Re}(\epsilon) = \text{Re}(\mu)$ and $\text{Re}(\xi) = -\text{Re}(\zeta) = 0$ then it is at least passively PT symmetric. We can enforce $\text{Re}(\epsilon) = \text{Re}(\mu)$ by choosing the gauge $kL = \frac{1}{2} \tan^{-1} \left(\frac{\text{Re}(\epsilon) - \text{Re}(\mu)}{2\text{Im}(\xi)} \right)$, so then all we need to do is see where $\text{Re}(\xi) = 0$ is satisfied in the parameter space of the gauged medium. We can also do this with the $[Y]$ matrix as the exceptional point connection with the $[S]$ matrix is the same as with $[C]^{-1}$. For the condition on the $[Y]$ matrix, one simply needs to replace ϵ with χ_e and μ with χ_m . The fact that we can always find a gauge such that $\text{Re}(\epsilon) = \text{Re}(\mu)$, or $\text{Re}(\chi_e) = \text{Re}(\chi_m)$, means that we can always relate UZR to PT symmetry in some region.

To illustrate this process, we will look at an example of the highly non-Hermitian continuous intensity systems studied by Stefan Rotter *et al.* [99]. They showed that for some real-valued function $W(x)$, having the boundary conditions $W(-d/2) = W(d/2) = 1$, a permittivity can be generated (over the region $-d/2 \leq x \leq d/2$) by a generating function,

$$\epsilon(x) = W^2(x) - \frac{i}{k_0} \partial_x W(x), \quad (4.16)$$

which will have UZR (i.e. an exceptional point) for all values of k_0 and d . This potential is clearly non-Hermitian and only has obvious PT symmetry when the function $W(x)$ is symmetric. However, the function $W(x)$ does not need to have any kind of symmetry to observe an exceptional point. Our example $\epsilon(x)$ can be seen in Figure 23 (a), which uses

$$W(x) = 1 + (\sin[\pi x/d]^2 + \exp[-(x - 0.2)^2/w] - \exp[-(x + 0.3)^2/w] + \exp[-(x - 0.6)^2/w])/10,$$

where $w = 0.01$. We can try to turn this profile into a more usual PT symmetric potential by adding a gain/loss parameter to the permittivity generating function in equation 4.16: $\epsilon(x) = W^2(x) - i\gamma\partial_x W(x)$, where we should have exceptional points wherever we have $\gamma = 1/k_0$. This modified potential is not PT symmetric in general but in some regions of the k_0, γ phase space it can have very similar behaviour to a PT symmetric system.

We can see this from the magnitude of the $[S]$ matrix eigenvalues when we set $k_0 = 1.9$ (plotted in Figure 23 (b)), where we have an unbroken phase ($|\sigma_j| = 1$) which leads to an exceptional point at $\gamma \sim 0.53$, followed by a broken phase (with $|\sigma_1| = 1/|\sigma_2|$). To see the PT symmetry in this system, we gauge the extracted $[Y]$ matrix as stated above and see where we have $Re(\xi) = 0$. This is shown in Figure 23 (b), where we have plotted a colour map of a UZR merit function, defined by $(|r_f| - |r_b|)/(|r_f| + |r_b|)$, which is equal to ± 1 for UZR.

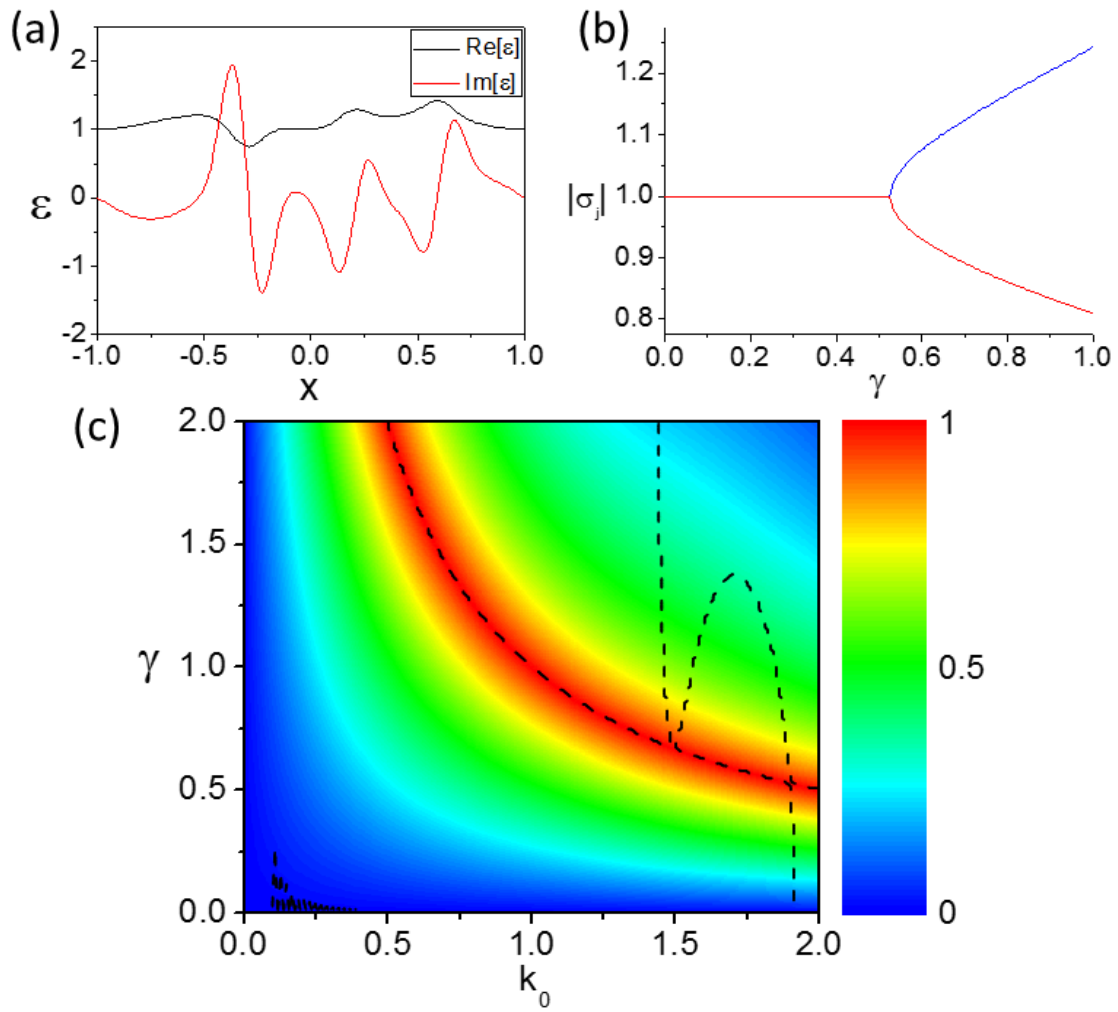


Figure 23: PT symmetry in an adjusted constant intensity system. (a) shows the real (black line) and imaginary (red line) parts of the inhomogeneous $\epsilon(x)$ as a function of position when $\gamma = 1$. We can see that there is no obvious PT symmetry in the potential. (b) shows the magnitude of the $[S]$ matrix eigenvalues when $k_0 = 1.9$, where we can see unbroken and broken phases separated by an exceptional point. (c) shows the UZR merit function, which reaches 1 when $\gamma = 1/k_0$. Also shown is the PT condition where the $Re(\xi) = 0$ for the gauged $[Y]$ matrix.

Also plotted are the contours where $Re(\xi) = 0$ represented by the black, dashed lines. We can see that all along the UZR contour, we have $Re(\xi) = 0$, which is not surprising. However, we have additional $Re(\xi) = 0$ contours which pass through the UZR contour. Along these extra contours, we have an unbroken phase and a broken phase, separated by an exceptional point. So, we can say that although this system is not PT symmetric in general, it can be seen to have PT symmetry along these contours and the exceptional points on these contours can be seen as due to PT symmetry.

4.9. Chapter Summary:

We have looked at the history of PT symmetry in quantum mechanics and its link to optics, with some examples of the effects of the unbroken and broken phases and their associated exceptional points. We have looked at some examples of PT symmetric systems using different types of parity operator. We also showed that we can achieve PT-like exceptional points in systems without gain if we apply a suitable loss bias to $[C]^{-1}$. Finally, we have discussed a new parity operator which uses a shifted mirror plane and we have linked the phenomenon of UZR to PT symmetric contours in a system's phase space.

Now that we have covered the theory of PT symmetry, we will analyse some PT symmetric metamaterial systems (defined using our new parity operator) to see what behaviour they exhibit.

5. Properties of PT Symmetric Metamaterials:

5.1. PT Symmetric Effective Medium:

We have seen that we can use the redefined parity operator to find new PT symmetry conditions on $[C]^{-1}$ that differ in form to the more usual $\epsilon = \epsilon^*$ and $\mu = \mu^*$ symmetry but which still contain an exceptional point. We will now use a specific case of this new parity operator (where $\phi_L = \pi/4$) to show the functionality which can be achieved by this new PT symmetry. If we at first assume that our material potential is diagonal (i.e. non-bianisotropic), enforcing $[\mathcal{P}_z \mathcal{T}, [C]^{-1}] = 0$ with $\phi_L = \pi/4$ will give us the condition that

$$\begin{pmatrix} \epsilon(z) & 0 \\ 0 & \mu(z) \end{pmatrix} = \begin{pmatrix} \mu^*(-z) & 0 \\ 0 & \epsilon^*(-z) \end{pmatrix}. \quad (5.1)$$

It is interesting to note that although the refractive index of this medium obeys the usual PT symmetry condition of $n(z) = n^*(-z)$, the condition for the intrinsic impedance is modified to $\eta(z) = 1/\eta^*(-z)$ (in contrast to the usual condition of $\eta(z) = \eta^*(-z)$). We can also use the constitutive matrix to relate the fields at two interfaces by discretising Maxwell's equations as in equation 3.11:

$$\begin{pmatrix} H_{y2} - H_{y1} \\ E_{x2} - E_{x1} \end{pmatrix} = \frac{ik_0 a}{2} [C]^{-1} \cdot \begin{pmatrix} E_{x2} + E_{x1} \\ H_{y2} + H_{y1} \end{pmatrix} \quad (5.2)$$

By considering the PT operation on this averaged constitutive matrix, we can derive the form of $[C]^{-1}$ to be

$$[C]^{-1} = \begin{pmatrix} \epsilon_{eff} & i\kappa_{eff} \\ -i\kappa_{eff} & \mu_{eff} \end{pmatrix} \quad (5.3)$$

with

$$\epsilon_{eff} = \mu_{eff}^* \text{ and } \kappa_{eff} = \kappa_{eff}^* \quad (5.4)$$

We can achieve this effective medium via stacking slabs with alternating gain and loss in their permittivity and permeability. If we form our unit cell from two slabs; one with loss in the permittivity and no magnetic response: $\epsilon_1 = b + i\gamma$ and $\mu_1 = 1$, and one with gain in the permeability but no electric response: $\epsilon_2 = 1$ and $\mu_2 = b - i\gamma$, then the effective medium of such a composite of total thickness a at a frequency k_0 (assuming that $k_0 a \ll 1$) is given by

$$[C]^{-1} = \begin{pmatrix} \frac{b + i\gamma + 1}{2} & \frac{ik_0 a(b^2 + \gamma^2 - 1)}{8} \\ -\frac{ik_0 a(b^2 + \gamma^2 - 1)}{8} & \frac{b - i\gamma + 1}{2} \end{pmatrix} \quad (5.5)$$

which fulfils our requirements. One interesting aspect of this constitutive tensor is that the non-Hermitian nature of this $[C]^{-1}$ is evident even at very low frequencies. As can be seen from the combining media formula (equation 3.19), in the effective medium descriptions of systems with the usual $\epsilon - \epsilon$ matching PT symmetry, the imaginary terms in the diagonal components average out to zero and the bianisotropic terms become very small at low frequency. This means that the exceptional points associated with $\epsilon - \epsilon$ matching systems can only be accessed at high frequencies. For $\epsilon - \mu$ matching PT symmetry, however, the imaginary parts of the diagonal terms do not average out in the effective medium limit and the bianisotropy terms (although still proportional to the frequency) are larger. This means that exceptional points in these systems can occur at much lower frequencies than in the standard PT symmetric systems.

5.2. Bandstructure of the PT Symmetric Medium:

We will start our analysis by considering propagation through a photonic crystal comprised of the composite unit cells discussed above. The equation relating the E and H fields either side of a unit cell can be written as

$$\begin{pmatrix} E_{x2} - E_{x1} \\ H_{y2} - H_{y1} \end{pmatrix} = \frac{ia}{2} [K] \cdot \begin{pmatrix} E_{x2} + E_{x1} \\ H_{y2} + H_{y1} \end{pmatrix} \quad (5.6)$$

where we have defined $[K]$ here as

$$[K] = k_0 \begin{pmatrix} 0 & 1 \\ 1 & 0 \end{pmatrix} \cdot [C]^{-1} \quad (5.7)$$

By insisting that the fields at interface 1 and 2 must be related by a Bloch phase e^{ika} , where k is the Bloch wavenumber, we can rewrite this as an eigenvalue problem for $[K]$:

$$[K] \cdot \begin{pmatrix} E_x \\ H_y \end{pmatrix} = \frac{2}{a} \tan\left(\frac{ka}{2}\right) \begin{pmatrix} E_x \\ H_y \end{pmatrix} \quad (5.8)$$

Using the definition of $[C]^{-1}$ in equation 5.2 and 5.3, we can derive the dispersion relation for the medium:

$$\pm \frac{2}{k_0 a} \tan\left(\frac{ka}{2}\right) = \sqrt{|\epsilon_{eff}|^2 - \kappa_{eff}^2}. \quad (5.9)$$

Here we can see the two phases of the wavenumber k : when $|\epsilon_{eff}|^2 > \kappa_{eff}^2$, the solutions for k will be a pair of real numbers with opposite signs but when $|\epsilon_{eff}|^2 < \kappa_{eff}^2$, the solutions for k will be a pair of purely imaginary numbers. The right-hand side of equation 5.9 can be a useful predictor of the band structure as the real, zero and imaginary phases of it correspond to the propagation band, exceptional point and band gap, respectively.

As a specific example, we will study the band structure of a photonic crystal with unit cells described by the constitutive matrix in equation 5.5 with b set to 2.25. A schematic of the layered system is shown in Figure 24 (a). The band structure of this system can be seen in Figure 24 (b), where the real part of the Bloch wavenumber is plotted against the normalised frequency (the ratio of a/λ) and the gain loss parameter γ . The lossless case ($\gamma = 0$) is highlighted by a black line and shows a conventional band structure with propagating bands from $k = 0$ to $k = \pi/a$ at the Brillouin zone edge, where a bandgap forms due to the mismatch of the permittivities and permeabilities of the unit cell's component slabs. It should be noted that the band structure for the negative k solution is just the mirror image of the positive k band structure.

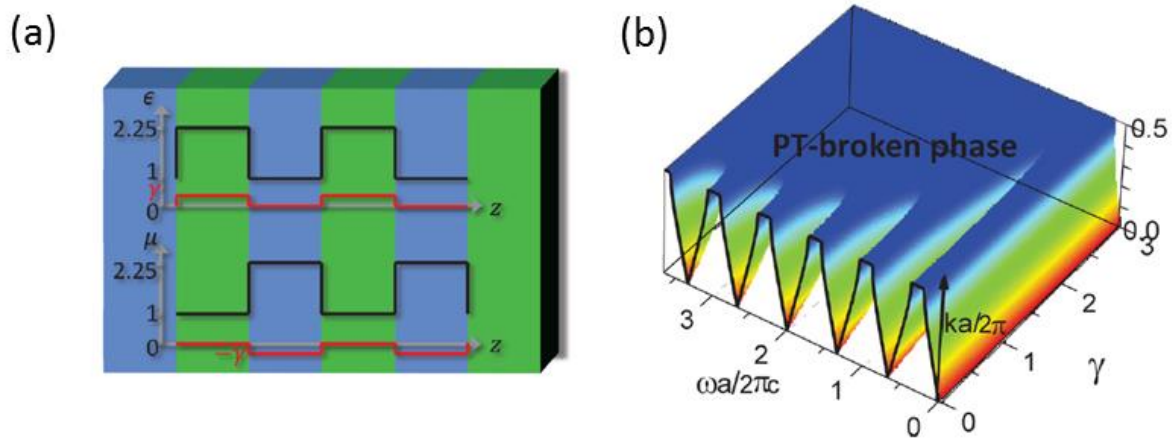


Figure 24: Material profile and bandstructure of the $P_{\pi/4}T$ symmetric system. (a) schematic of the material profile of the photonic crystal. (b) band structure as a function of the normalised frequency ($\omega a/2\pi c$) and the gain loss parameter (γ). The top surface indicates the PT broken phase and the black line shows the band structure for the lossless system.

As γ increases, the propagating bands with two real k solutions gradually close as they

approach the exceptional point. Beyond the exceptional point, the bands have a non-zero

$Im[k]$ and $Re[k] = \pi/a$. This region is the flat, blue area in Figure 24 (b). The existence of

two phases is also evident in the reflection characteristics of the structure. Figure 25 (a) and

(b) show the forwards and backwards reflection (respectively) of four unit cells with PT symmetry when $\phi_L = 0$, where $\epsilon_1 = 2.25 + i\gamma$, $\epsilon_2 = 2.25 - i\gamma$ and $\mu_1 = \mu_2 = 1$, in a natural log scale. (c) and (d) show the corresponding reflection characteristics for four units cells with PT symmetry when $\phi_L = \pi/4$, with $\epsilon_1 = 2.25 + i\gamma$, $\mu_2 = 2.25 - i\gamma$ and $\epsilon_2 = \mu_1 = 1$, also in a natural log scale.

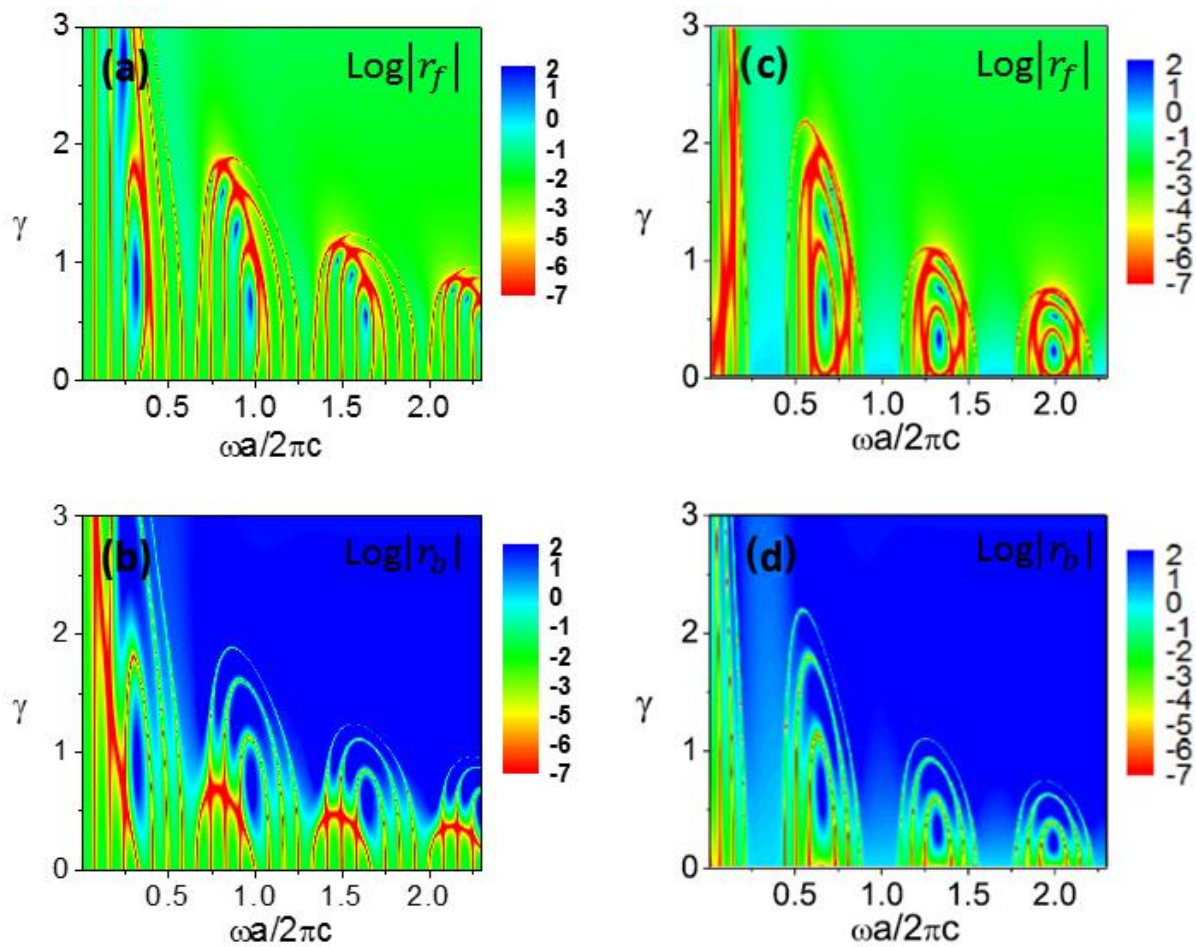


Figure 25: forwards and backwards reflectance for four, PT symmetric unit cells. (a) and (b) show the reflection for positive- z and negative- z incidence (respectively) of four PT symmetric unit cells with $\epsilon - \epsilon$ matching PT symmetry. (c) and (d) show the corresponding reflection characteristics of four stacked unit cells with $\epsilon - \mu$ matching PT symmetry. The UZR points can be seen as the additional red rings and lines.

For small γ , the reflections are approximately the same, with the dips and peaks due to the Fabry-Perot resonances and bandgaps respectively. However, as γ and the frequency

increase, the reflections become dramatically different, with the backwards reflection becoming much larger than the forwards reflectance.

5.3. Exceptional Points and Unidirectional Zero Reflection:

We can also see from Figure 25 (c) that there is an additional ring of very low reflectance in the forwards reflectance spectrum. This is due to exceptional points in the system, which we will explore in the long wavelength limit. In this limit, we can accurately describe the unit cell with the effective medium tensor in equation 5.5. Taking eigenvalues of this, we can see that there will be an exceptional point when

$$(k_0 a(b^2 + \gamma^2 - 1))^2 - 16\gamma^2 = 0 \quad (5.10)$$

Due to the correspondence between exceptional points in $[C]^{-1}$ and exceptional points in the scattering matrix, we would expect to see UZR when this condition is satisfied. To quantify UZR, we will define a merit function:

$$\rho = \frac{|r_f| - |r_b|}{|r_b| + |r_f|}. \quad (5.11)$$

This will be equal to 1 or -1 for UZR (with $r_b = 0$ and $r_f = 0$, respectively) and equal to zero when $r_b = r_f$. The solutions for equation 5.10 and the value of ρ are shown in Figure 26, where the black lines show the exceptional points in the constitutive matrix and the colour map is the value of ρ . Figure 26 (a) shows these quantities for a system with standard PT symmetry, with $\epsilon_1 = 2.25 + i\gamma$, $\epsilon_2 = 2.25 - i\gamma$ and $\mu_1 = \mu_2 = 1$, and Figure 26 (b) shows them for our current system. As we can see, the exceptional points and maxima/minima of the merit

function match quite well. Another fact we can observe in Figure 26 is that the $\epsilon - \mu$ mixing PT symmetry we have derived can give UZR for small gain/loss contrast even at very low frequencies, much lower than that in the $\epsilon - \epsilon$ matching case. This agrees with our previous discussion about the averaging of gain and loss in the effective medium limit. This could be useful in experimental realisations as more easily achievable gain/loss values can be used to give exceptional points simply by lowering the frequency.

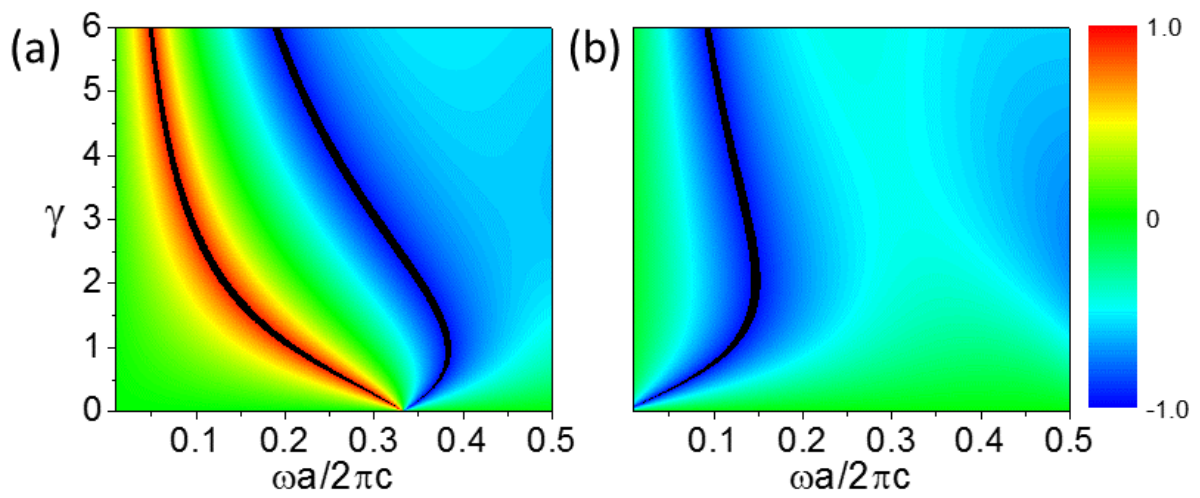


Figure 26: A comparison of UZR merit ρ (colour map) and exceptional points (black lines) in the effective medium matrix. (a) shows the merit and exceptional points for a unit cell with $\epsilon_1 = 2.25 + i\gamma$, $\epsilon_2 = 2.25 - i\gamma$ and $\mu_1 = \mu_2 = 1$. (b) show the same quantities but for our current system, with $\epsilon_1 = 2.25 + i\gamma$, $\mu_2 = 2.25 - i\gamma$ and $\epsilon_1 = \mu_2 = 1$.

To examine the behaviour of the eigenvalues of $[C]^{-1}$ more closely, we will next consider the system at a fixed free-space wavelength of 4.8 (dimensionless units) and with $a = 0.08$. Figure 27 a) shows the real (black) and imaginary (red) parts of the eigenvalues of $[C]^{-1}$ (labelled as c_i^{-1}) as γ is varied, where the solid lines are analytical results from equation 5.5 and the circles are numerical results obtained from simulation (using COMSOL Multiphysics). As γ is increased, the real parts of c_i^{-1} converge until a threshold value, $\gamma_{ex} = 0.107$, is reached, where they coincide at an exceptional point. Beyond this point, c_i^{-1} split into a complex conjugate pair. Figure 27 (b) shows a parametric plot of c_i^{-1} , with the arrows showing the

direction of increasing γ . Here, the exceptional point is marked by the point in the middle where the two eigenvalues meet and suddenly change direction.

So far, we have considered an ideally PT symmetric system, where we have balanced loss with an equal amount of gain. In order to make experimental realisation easier, we will also examine a passive PT symmetric system. To do this, we will use a system with no loss in the first slab ($Im[\epsilon_1] = 0$) and loss in the second slab ($Im[\mu_2] = 2\gamma > 0$). Using the effective medium matrix, we can see that we can still have an exceptional point for this system if the real part of μ_2 is adjusted slightly. By considering the eigenvalues of $[C]^{-1}$, we can show that the system will have an exceptional point at a frequency k_0 and thickness a if the real part of μ_2 is given by

$$Re[\mu_2] = Re[\epsilon_1] \frac{4 + k_0^2 a^2}{4 + Re[\epsilon_1]^2 k_0^2 a^2} \quad (5.12)$$

With our current parameters, this corresponds to $\epsilon_1 = 2.25$, $\mu_2 = 2.22528 + 2i\gamma$ (we have used 2γ so that the exceptional point will occur at approximately the same value of γ). This may seem like it is breaking the $Re(\epsilon_{eff}) = Re(\mu_{eff})$ condition but as we have seen, we can always gauge the constitutive matrix back to this condition when the system contains an exceptional point. The eigenvalue behaviour of this passive PT symmetric system can be seen in Figure 27 (c), with a parametric plot in Figure 27 (d). The eigenvalues (c_i^{-1}) show similar behaviour around the exceptional points but there is an additional γ term in the imaginary parts due to the biasing we discussed previously.

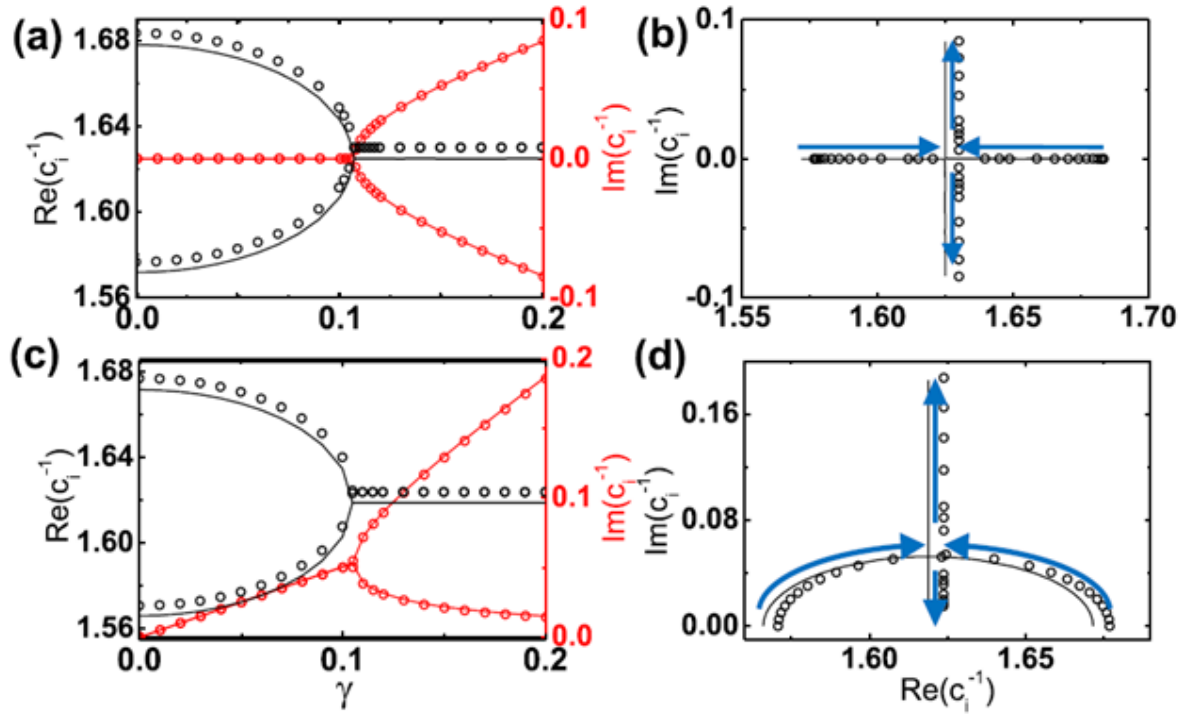


Figure 27: Plots of the real and imaginary parts of the eigenvalues of C^{-1} (labelled as c_i^{-1}) as a function of the gain/loss parameter γ . The solid lines are the analytic formula and the circles are numerical results. (a) shows the real (black) and imaginary (red) parts of c_i^{-1} for the ideal ($\epsilon_1 = \mu_2^*$) case and (b) is a parametric plot, with the arrows showing the direction of increasing γ . (c) and (d) show equivalent plots for the lossy case (where the loss is only in μ_2).

To prove that this exceptional point is due to PT symmetry and not some accidental degeneracy, we can check to see if this $[C]^{-1}$ matrix can be written as in equation 4.15. To do this, we first gauge the extracted $[C]^{-1}$ so that $\text{Re}[\epsilon_{eff}] = \text{Re}[\mu_{eff}]$, which can be done by choosing $kL = \frac{1}{2} \tan^{-1} \left(\frac{\text{Re}(\epsilon) - \text{Re}(\mu)}{2\text{Im}(\xi)} \right)$. In Figure 28 we plot the UZR merit function for this passive system (to the seventh power to make the EP more visible) and we can see that the EP occurs when $\omega a / 2\pi c = 0.105$ and $\gamma = 0.105$. The dashed line shows where $\text{Re}[\xi_{eff}] = 0$ after the gauging process. This line passes straight through the EP, confirming that it is due to passive PT symmetry in the system.

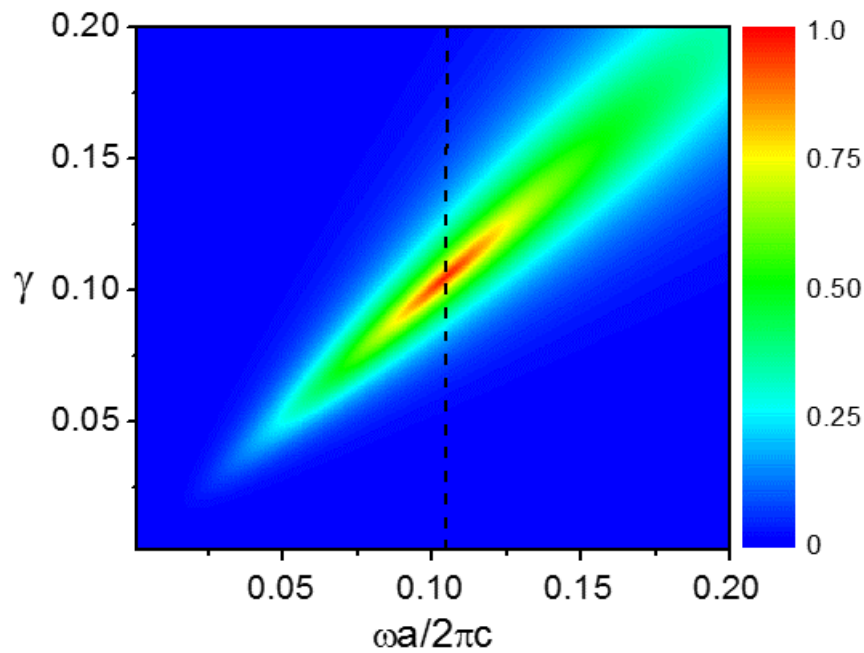


Figure 28: Confirming PT symmetry for the passive system. A colour map of χ plotted to the seventh power (to make the EP more visible) and the passive PT condition of $Re[\xi] = 0$ after gauging is shown as the dashed line. The EP lies on the PT symmetric contour, showing the correspondence between EPs (and so UZR) and PT symmetry.

We will seek experimental confirmation of this UZR – PT symmetry link in chapter 6.1.

5.4. Lasing and Coherent Perfect Absorption:

We have looked at some examples of gauged PT symmetric system that contain exceptional points/UZR but there are other ways in which we can use this new kind of PT symmetry. In the following sections, we will seek to develop an understanding of the phenomena of lasing and absorption from an effective medium perspective and how the two effects can be related through gauged PT symmetry. There has been some discussion in the literature on the subject of simultaneous lasing and coherent perfect absorption (CPA) [100-103] (the latter sometimes being referred to as anti-lasing) and its link to PT symmetry. However, these systems are all based on grating structures (with the potential varying in the direction of propagation), where the incident wave length is on the order of the lattice length. Here, we will develop the concept

of lasing and CPA in an effective medium setting and show that such effects can occur for subwavelength systems if a suitable amount of gain and loss can be achieved. We will start by studying a homogenous metamaterial slab of thickness L with incident/outgoing field amplitudes on either side described by a_i and b_i , respectively, with subscript i denoting the interface number (as in Figure 29 (a)). If we first take the case where we have no bianisotropy ($\xi = \zeta = 0$), we can get an analytic solution for b_i when $a_1 = a_2 = 1$ (symmetric incidence):

$$b_i = \frac{\sqrt{\mu} \cos[\sqrt{\epsilon}\sqrt{\mu}\phi_0/2] + i\sqrt{\epsilon} \sin[\sqrt{\epsilon}\sqrt{\mu}\phi_0/2]}{\sqrt{\mu} \cos[\sqrt{\epsilon}\sqrt{\mu}\phi_0/2] - i\sqrt{\epsilon} \sin[\sqrt{\epsilon}\sqrt{\mu}\phi_0/2]}. \quad (5.13)$$

The definition of coherent lasing and absorbing states can then be seen to be where $b_i \rightarrow \infty$ (lasing) and where $b_i \rightarrow 0$ (absorption) for a certain a_i . This implies that the conditions for lasing and CPA can then be seen as when the denominator goes to zero and the when the numerator goes to zero (respectively). Due to the trigonometric function, there is not an analytic solution for these conditions but we can approximate them by taking a series in ϕ_0 . Doing so, setting the denominator/numerator to zero and solving for ϵ gives us a solution of $\epsilon = -2i/\phi_0$ for lasing and $\epsilon = 2i/\phi_0$ for CPA (both with arbitrary μ). A similar analysis of b_i when $a_1 = 1$ and $a_2 = -1$ (antisymmetric incidence) will give $\mu = -2i/\phi_0$ for lasing and $\mu = 2i/\phi_0$ for CPA (both with arbitrary ϵ). We can include bianisotropy by considering the link between the $[S]$ and $[C]^{-1}$ matrices. As we have seen before, we can relate the S parameters of the slab to an effective constitutive matrix, $[C]^{-1}$:

$$[C]^{-1} = \frac{2}{i\phi_0} [B] \cdot \frac{[S] - [I]}{[S] + [I]} \cdot [B]^{-1} \text{ with } [B] = \begin{pmatrix} 1 & 1 \\ 1 & -1 \end{pmatrix}, \quad (5.14)$$

Where $\phi_0 = k_0 L$ (k_0 is the freespace wavenumber) and the $[S]$ matrix is defined by $(b_2, b_1) = [S] \cdot (a_1, a_2)$. To find the condition on $[C]^{-1}$ for these situations to occur, we can turn equation

5.14 into an eigenvalue problem. As the $[B]$ matrices are unitary (and so do not affect the eigenvalues) we can relate the eigenvalues of $[S]$ and $[C]^{-1}$ (denoted as s_i and c_i^{-1} , respectively) by

$$c_i^{-1} = \frac{2}{i\phi_0} \frac{s_i - 1}{s_i + 1} \quad (5.15)$$

Then, restating our lasing and absorbing conditions as $s_i \rightarrow \infty$ and $s_i \rightarrow 0$ (respectively) where i can be 1 or 2, we can see that lasing corresponds to one of the c_i^{-1} s being $-2i/\phi_0$ and absorption corresponds to one of the c_i^{-1} s being $2i/\phi_0$. If we assume that our system response has the form

$$[C]^{-1} = \begin{pmatrix} \epsilon & i\kappa \\ -i\kappa & \mu \end{pmatrix}. \quad (5.16)$$

Then we can state the condition of coherent lasing or absorption as

$$\kappa^2 - \epsilon\mu = m \frac{2i}{\phi_0} \left(m \frac{2i}{\phi_0} - (\epsilon + \mu) \right) \quad (5.17)$$

where m is +1 for absorption and -1 for lasing.

It is interesting to note that the condition on the middle plane $[Y]$ matrix is actually the same as on $[C]^{-1}$. The middle plane collapsing process adds a $e^{-i\phi_0}$ factor to the S matrix eigenvalues and using the $[Y]$ matrix adds a ϕ_0 factor to the extraction formula, which means that our equivalent condition for coherent lasing/absorption on the middle plane $[Y]$ matrix is actually the very similar to equation 5.17 (but with $\epsilon \rightarrow \chi_e$ and $\mu \rightarrow \chi_m$ and ϕ_0 set to one). This may seem counterintuitive, as we expect that $\chi_e = \epsilon - 1$ and $\chi_m = \mu - 1$. This apparent

contradiction is due to the fact that we are working with effective material parameters, which do not always correspond to the microscopic material parameters of the system.

5.5. Parity and Time Reversal Transformations on Lasing and Absorbing States:

It is interesting to note that the lasing and absorbing states can be related through a time reversal operation. If we start from a coherent absorption state with inputs $a_1(a_2)$ from the left (right) side (as in Figure 29 (b)), then time-reversal means taking a complex conjugate of the $[C]^{-1}$ matrix and wave amplitudes, and swapping the incident and outgoing waves. This is equivalent to changing the sign of m in equation 5.17. This means that we can transform a lasing/absorbing mode into an absorbing/lasing mode by time reversing the system parameters. This process is illustrated in Figure 29 (b) and (c). Next, we shall look at the role of the parity operator on these states. Our 2x2 constitutive matrix has two eigenvalues and eigenvectors associated with it, meaning that we can have more than one way of achieving a coherent lasing or absorbing state. Interestingly, we can switch between these two eigenstates by using the redefined parity operator developed previously (with kL set to $\pi/4$). Using this operator on the C^{-1} matrix will swap the permittivity and permeability due to the interchange of electric and magnetic fields. In terms of the input amplitudes (a_i), the action of this parity operator can be quantified as $\begin{pmatrix} a_1 \\ a_2 \end{pmatrix} \rightarrow \begin{pmatrix} a_2 \\ -a_1 \end{pmatrix}$. This operation is depicted in Figure 29 (b) and (d). An interesting observation of this is that if we want to have coherent lasing or absorption for both of these modes, then we must have $\epsilon = \mu$, similar to the condition of impedance matching in other absorbing metamaterial systems.

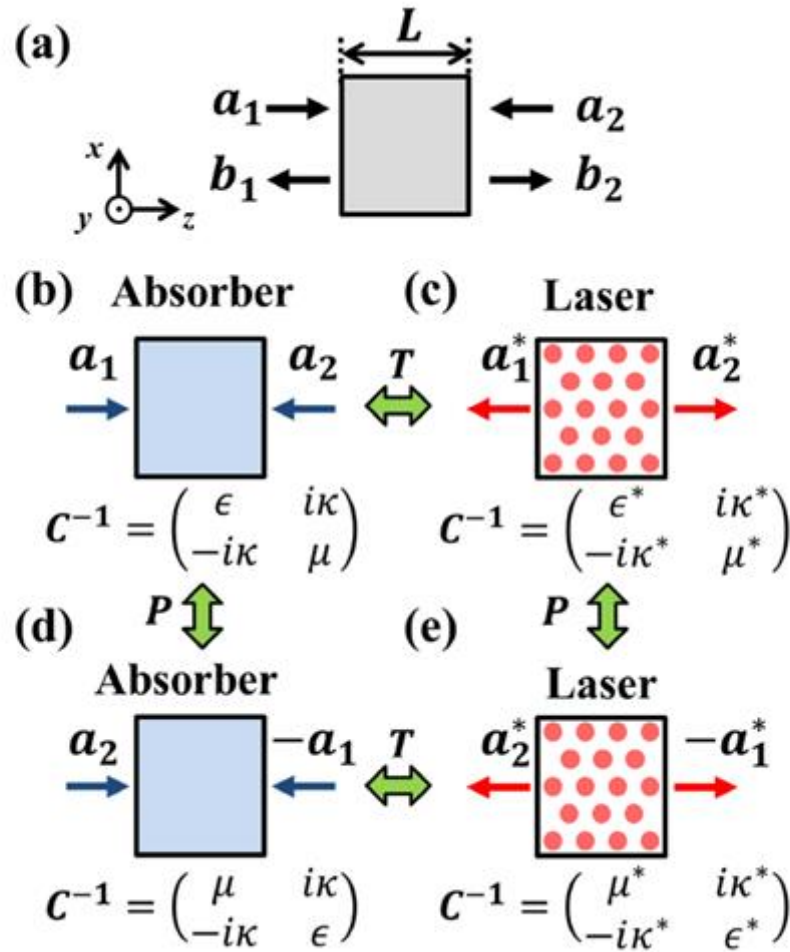


Figure 29: Illustration of a scattering system and the effects of the P and T operators on inputs. (a) is a schematic of the metamaterial slab, showing coordinate and incident/outgoing (a_i/b_i) field labelling conventions. (b)-(e) show how different coherent lasing/absorbing states can be linked via the parity and time-reversal operations, where the transformed response matrix is also shown.

Now we will examine the combined effects of the parity and time reversal operators. As the P and T operators commute, we can use the diagram in Figure 29 (b)-(e) as a guide. For example, if we start off with an absorbing state in (a) (i.e. one of the eigenvalues of $[C]^{-1}$ is $2i/\phi_0$), then applying the parity operator (d) would swap the mode which is being coherently absorbed. A further application of the time reversal operator would swap this absorbing mode to a lasing mode. As the two input modes being interchanged are linearly independent (as are

the output modes), then we have the possibility to realise a system which can simultaneously display coherent lasing and absorption (which we will term a laser-absorber). If we assume that our constitutive matrix is of the same form as equation 5.16, then our condition for invariance under this combined transformation is $\epsilon = \mu^*$ and $\kappa = \kappa^*$. If we also demand that equation 5.17 be satisfied, then we can obtain a general form of the constitutive matrix for a laser absorber:

$$[C]^{-1} = \begin{pmatrix} \pm i \sqrt{4/\phi_0^2 + \kappa^2} & i\kappa \\ -i\kappa & \mp i \sqrt{4/\phi_0^2 + \kappa^2} \end{pmatrix} \quad (5.18)$$

Where the upper and lower signs dictate which mode will lase or absorb. If we at first take the case of a symmetric structure where $\kappa = 0$ and choose the lower sign, the eigenvalues (i.e. ϵ and μ) will be $-2i/\phi_0$ and $2i/\phi_0$ (as intended) with corresponding eigenvectors (1,0) and (0,1). These eigenvectors are currently in the E/H basis which means that our lasing state should have a purely electric incident field and the absorbing state should have a purely magnetic incident field. We can find out what this means in terms of our incident waves by considering the constructive and destructive interference which occurs when counter-propagating waves are mixed. When the direction of a propagating EM plane wave is flipped, its electric field remains the same but its magnetic field changes sign (essentially a parity transformation). This means that if we superimpose two counter-propagating EM waves which are in phase, then the electric fields will constructively interfere but the magnetic fields will destructively interfere, giving us the ‘purely electric’ incident field we need. For the purely magnetic incident field associated with the absorbing state, all we need to do is shift the phase of one of the waves by π , which will swap the constructive/destructive interference of the

fields. So, we can see that for the $[C]^{-1}$ matrix we have chosen, we will have a lasing state when $\begin{pmatrix} a_1 \\ a_2 \end{pmatrix} = \begin{pmatrix} 1 \\ 1 \end{pmatrix}$ (symmetric incidence) and an absorbing state when $\begin{pmatrix} a_1 \\ a_2 \end{pmatrix} = \begin{pmatrix} 1 \\ -1 \end{pmatrix}$ (antisymmetric incidence). The effect of non-zero κ is that the lasing/absorbing states can be understood through the eigenvalues. The full eigenvectors of the constitutive matrix in equation 5.18 with non-zero κ are $\left(\left(\pm 2 + \sqrt{\kappa^2 \phi_0^2 + 4} \right) / \kappa \phi_0, 1 \right)^T$, which, in our a_i basis, corresponds to an eigenstate of the form $\begin{pmatrix} x + 1 \\ x - 1 \end{pmatrix}$. What this means is that if we have a very strongly bianisotropic laser-absorber, then we could control the reflectance of our structure by only using a very small control beam (small compared to the other, fixed beam). While this certainly could have interesting applications, we will stick to the non-bianisotropic case for the following discussions.

5.6. Lasing and Absorption on PEC and PMC substrates:

This constructive and destructive interference can also be imitated by PEC and PMC boundary conditions. If we place a PMC or PEC boundary at the centre of the structure, then it can imitate the $H_{||} = 0$ and $E_{||} = 0$ conditions associated with the symmetric and anti-symmetric modes (respectively). This is depicted in Figure 30 (a). This means that we can still see the lasing and absorbing states in a one port system (i.e. a surface). If we now introduce the impedance and index of the metasurface as $Z_M = \sqrt{\mu_M} / \sqrt{\epsilon_M}$ and $n_M = \sqrt{\epsilon_M} \sqrt{\mu_M}$ we can see that the index is essentially our gain/loss parameter (i.e. our laser-absorber condition is that $n_M = 2/\phi_0$). Figure 30 (b) and (c) show the reflectance of a halved laser-absorber, with $\kappa = 0$ and with the same sign convention as used above, attached to a PMC surface (Figure 30 (b))

and a PEC surface (Figure 30 (c)) to imitate the antisymmetric and symmetric incident modes. The colour map shows the analytically calculated reflectance of the surfaces as a function of the phase thickness ϕ_0 and the gain/loss parameter n_M and the dashed line shows the analytical CPA-laser condition (equation 5.17). We can see that there is a definite correspondence between the choice of boundary and the state of the laser absorber, in agreement with our discussion above.

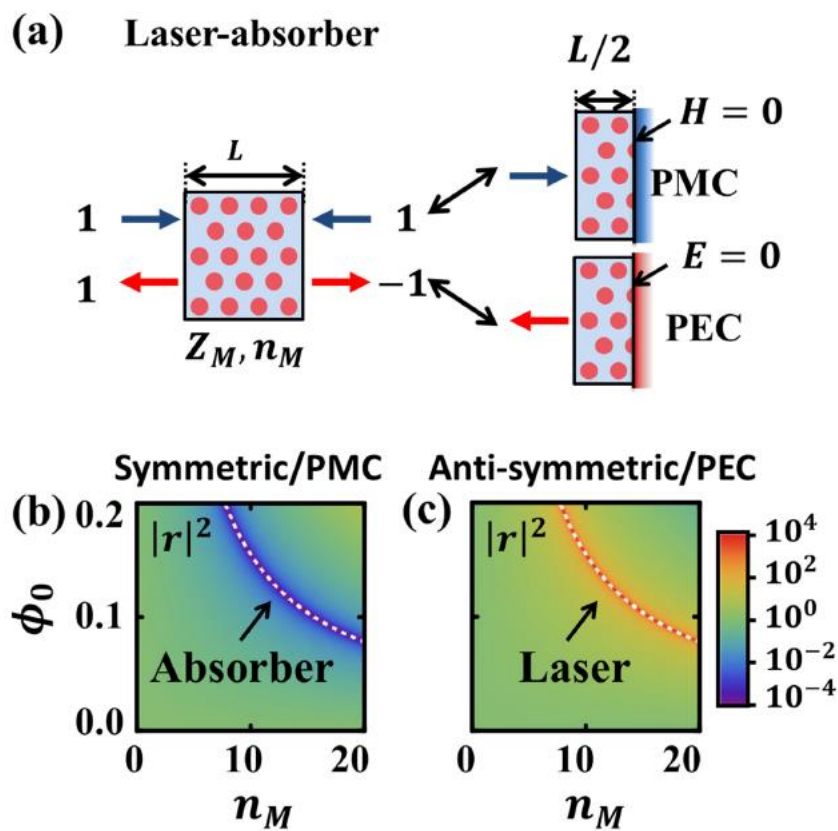


Figure 30: Illustration of the correspondence between symm./asymm. inputs and PMC/PEC boundary conditions. (a) Imitation of lasing and absorbing modes in a non-bianisotropic laser-absorber by PEC and PMC surfaces. (b) and (c) are the reflection coefficients of the halved laser absorber on a PMC and PEC surface as a function of ϕ_0 and the gain/loss parameter n_M . The colour map shows the magnitude of the reflection and the dashed line is the CPA-laser condition.

5.7. Amplified sensing:

Recently, there has been some study of the use of non-Hermitian systems for sensing applications [104,105]. Researchers found that introducing gain into lossy ring resonators

could yield a highly sensitive exceptional point. When a small particle was placed in the vicinity of the rings, they disturbed the near fields of the structure, changing the coupling between the cavity modes and so destroying the exceptional point. The destruction of the exceptional point resulted in frequency splitting of the resonances, which can be measured and quantified and so used to detect the particles. In light of the amplification/absorption properties of the surface configuration of our laser/CPA system, we will examine its possible use as a sensor.

While there are already surfaces which use impedance matching and loss to maximise absorption in a surface [106-108], the addition of gain could amplify the incoming signal and so boost the amount of energy absorbed, meaning that we could end up absorbing more energy than is incident on the sensor (similar, in principle, to a photomultiplier tube). There has already been an experiment with acoustic waves that shows a PT symmetric bulk modulus profile (realised with a speaker linked to an active element and a passive speaker acting as an absorber) can increase the amount of energy absorbed up to two times the incident energy while also suppressing reflection in one direction [83]. If we operate the slab near the lasing threshold but include loss in the slab, we should be able to see enhanced absorption. Ideally, we would like to include loss and gain in the same slab but this could be difficult to achieve in practice. What we propose instead is a two-layer system with an effective medium tensor which fulfils the laser-absorber condition. If we label the two slabs as A and B, where the outer slab is A and the inner slab is B (as depicted in Figure 31 (a), left-hand side), then a combination which fits the laser absorber condition is $\epsilon_A = 2i\gamma$, $\mu_A = 0$, $\epsilon_B = 0$, $\mu_B = -i\gamma$. To retrieve the $[C]^{-1}$ of this system, we must consider the structure plus its mirror image (Figure 31 (a), right-hand side). Using our effect medium formula (equation 3.22) and putting in the S parameters of the mirrored structure, the retrieved C^{-1} is

$$[C]^{-1} = \begin{pmatrix} i\gamma & 0 \\ 0 & 4i\gamma/(\gamma^2\phi_0^2 - 8) \end{pmatrix} \quad (5.19)$$

Which will fulfil the laser-absorber condition when $\gamma = 2/\phi_0$. A plot of the real (solid black line) and imaginary (solid red line) parts of the extracted ϵ and μ when ϕ_0 is set at 0.2 can be seen in Figure 31 (b), showing that our effective medium condition is achieved when $\gamma = 10$. We can check the lasing behaviour by looking at the reflectance of the metasurface.

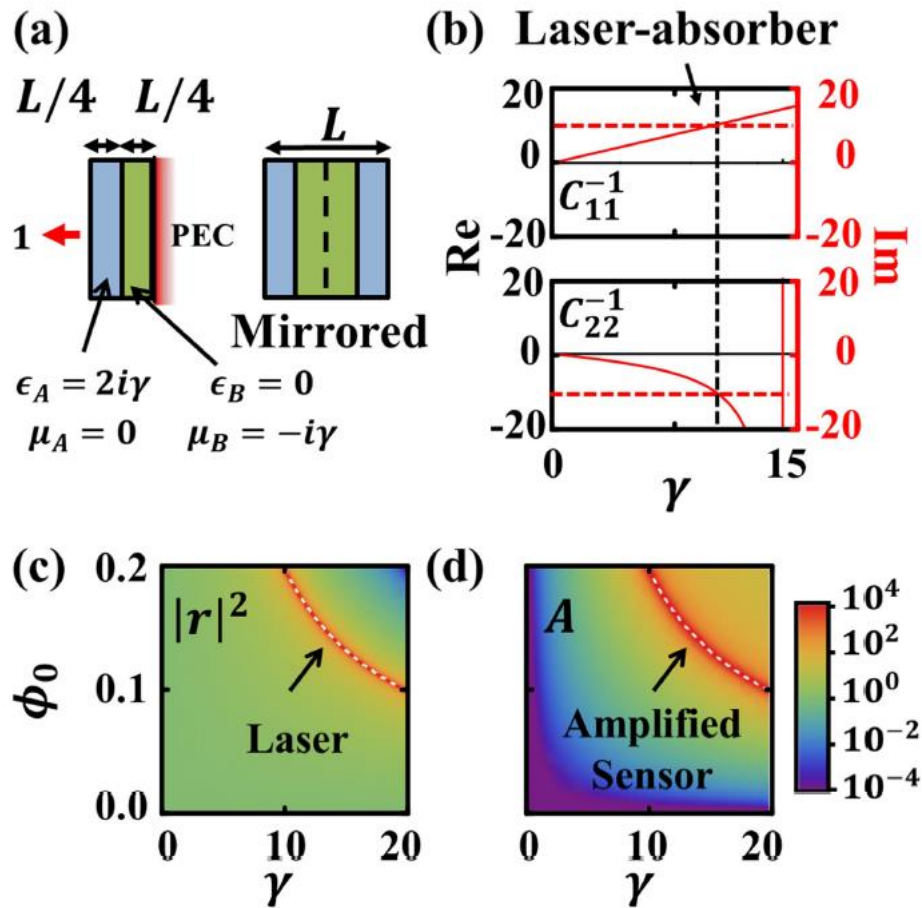


Figure 31: Effective medium extraction and absorption properties of the amplified sensing surface. (a) shows the labelling convention and material parameters of the amplified sensor and next to it is the mirrored structure used to extract the effective medium. (b) is the real (solid black lines) and imaginary (solid red lines) parts of 1,1 and 2,2 components of the $[C]^{-1}$ matrix extracted from the mirrored structure in (a). (c) is a colour map plot of the reflectance of the surface as a function of ϕ_0 and γ , with the CPA-laser condition shown as the dashed line. (d) is a colour map of the absorption in the outer (subscript A) layer as a function of ϕ_0 and γ , with the CPA laser condition shown again as a dashed line.

Figure 31 (c) shows the reflectance as a function of ϕ_0 and γ , where the colour map is the reflectance and the dashed line is the CPA-laser condition. To find the total absorption of the inner slab, we can take the real part of the time derivative of equation 3.34. In our time-harmonic, non-bianisotropic, non-dispersive case, this reduces to:

$$A = k_0 \int (\text{Im}(\epsilon_r)|E|^2/Z_0 + \text{Im}(\mu_r)|H|^2Z_0) dV \quad (5.20)$$

where Z_0 is the impedance of vacuum. Performing this integral on the outer (A) slab and dividing by the incident power will give us the normalised absorption, which is plotted in Figure 31 (d). As expected, we see a huge increase in absorption near the lasing condition. This could have obvious applications in sensing but the parameters for the slabs here would be difficult to realise in practise as having constitutive parameters with precisely zero real and imaginary parts is quite difficult.

5.8. Chapter Summary:

In this chapter, we have looked at the bandstructure, scattering and effective medium properties of a composite PT symmetric metamaterial with our new gauged PT symmetry.

We have numerically confirmed the link between UZR and exceptional points in the constitutive matrix. We have also seen (numerically) that we can introduce a bias in the system to make it passive but still retain an exceptional point, we did require a small change in the real part of the permittivity but this can be understood as a gauging process. We then examined lasing and absorbing states, how they (and their input states) can be related through our gauged PT symmetry and how they can be obtained simultaneously. Finally, we showed that this setup could have an application in sensing, where the amplifying properties

of the system allows it to absorb more power than is incident on it. In the next section, we will seek some experimental verification of these ideas. We will start by attempting to prove our assertion that UZR can be related to PT symmetry by designing a tuneable bianisotropic transmission line system containing an exceptional point and examining its material parameters. We will then show some analysis of a tunnel diode for use as an amplifier in a laser-absorber, then design a laser-absorber and measure its properties.

6. Realising PT Symmetric Metamaterials with Transmission Line Structures:

6.1. Bianisotropic PT symmetric Transmission Line:

We have previously seen that our new shifted PT symmetry can produce systems with UZR.

Now we seek to analyse a system with UZR to see if it can be explained by this shifted PT symmetry.

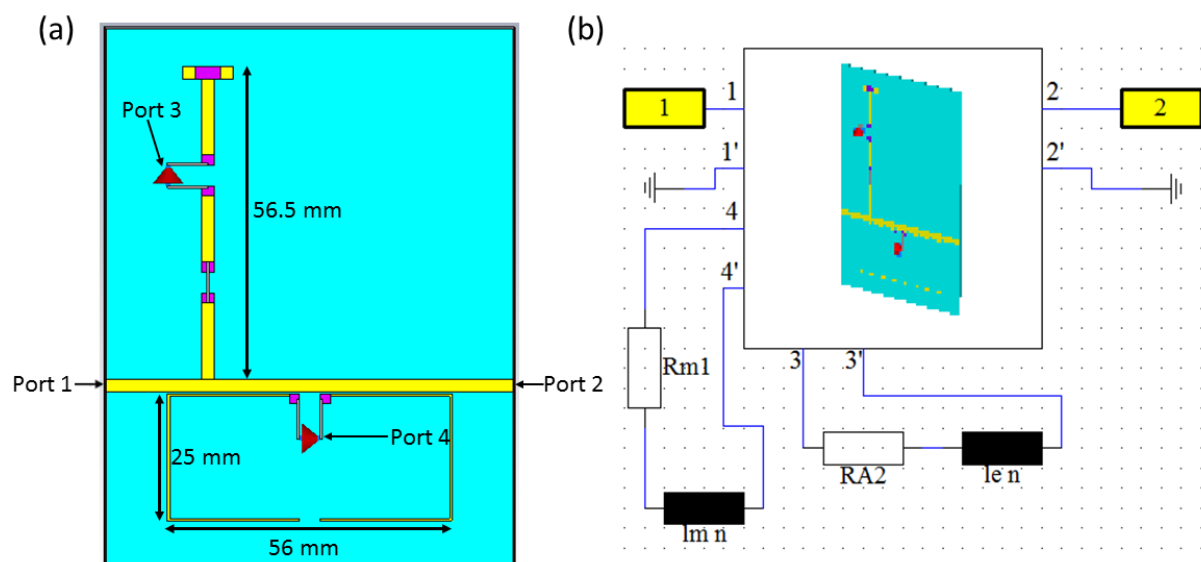


Figure 32: Diagram and simulation schematic of the bianisotropic transmission line structure. (a) shows the structure and port setup for the simulation, where the yellow, purple and blue areas represent copper, lead (solder) and Roger's 5880 dielectric, respectively. (b) is the simulation schematic, where ports 3 and 4 are used to attach variable resistors to the simulation.

To do this, we will use a structure with an electric resonator coupled to a magnetic resonator, but with the electric resonator shifted away from the central axis by 20mm, as depicted in Figure 32 (a) and (b). This shifting will generate bianisotropy, which, when combined with a suitable loss contrast between the electric and magnetic resonators, will give us UZR. We could have also used two electric resonators shifted with respect to each other but, as we saw in the previous sections, the exceptional points generally require a higher frequency to be

realised and this makes effective medium analysis more difficult. As we are using a transmission line system for this realisation, we will be using the Y matrix, extracted with collapsed (middle) plane S-parameters, for our analysis.

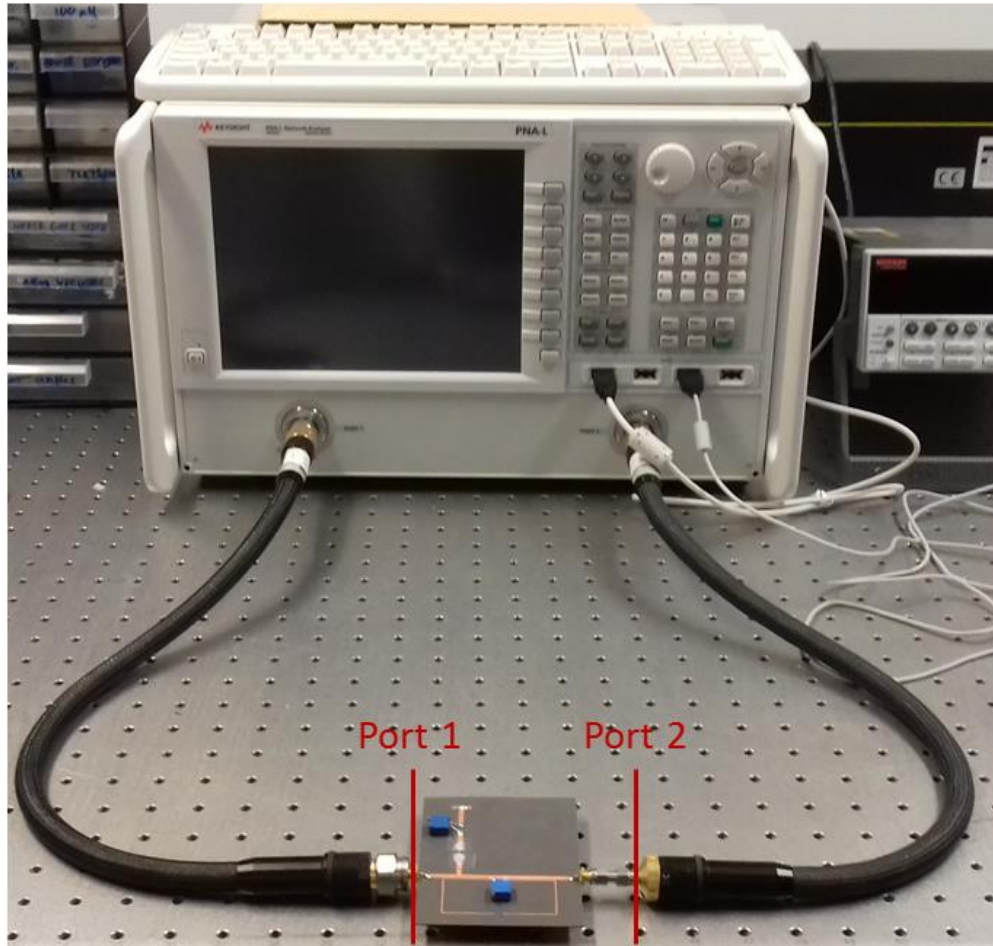


Figure 33: Experimental setup for the bianisotropic transmission line. The Agilent N5232A vector network analyser (centre) is connected to the sample (bottom middle) via two 50 Ohm cables. The analyser is calibrated so that the measured S parameters have their reference planes at the end of the cables, indicated by the red lines.

The experimental setup for the system is shown in Figure 33. An Agilent N5232A vector network analyser (grey box) is connected to the sample with 50 Ohm cables so that the S parameters of the system can be measured. The analyser is calibrated so that the reference planes of the S parameters are at the ends of the cables (red lines). We then convert to middle reference planes in post-processing.

The fabricated structures are shown in Figure 34 (a) and (b), where (a) shows the symmetric structure and (b) shows the same structure but with the electric resonator shifted backwards by a phase factor $k\delta$, where δ is -20mm. The four graphs in (c) show the extracted $[Y]$ matrix elements of the shifted structure when the variable resistor in the electric resonator is set to its minimum and the variable resistor in the magnetic resonator set to 20 Ω .

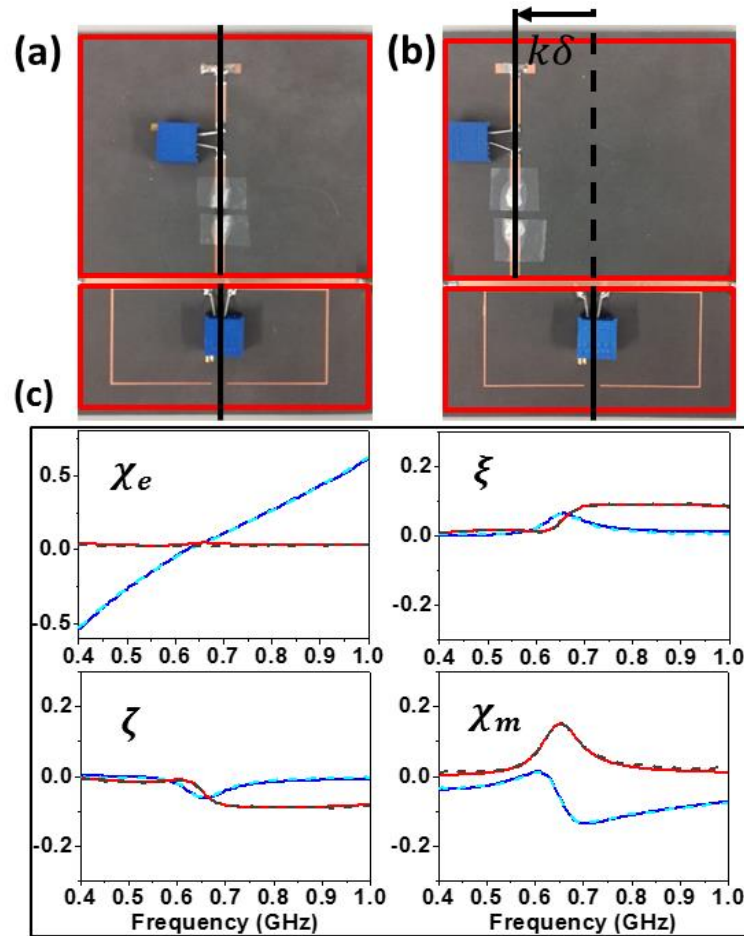


Figure 34: Photos of the unshifted and shifted transmission line structures and the extracted constitutive parameters of the shifted structure. (a) Photo of a symmetric structure where the reference planes of the electric (upper red box) and magnetic (lower red box) resonators are aligned to the same position. (b) Photo of the structure with bianisotropy with variable resistance at the electric (magnetic) atom being set as 0 (20) Ω . (c) Y-matrix elements with reference plane at the electric atom. The solid blue and red lines denote the real and imaginary parts of the matrix elements extracted from measurements, respectively. The light blue and dark red dashed lines are the real and imaginary parts of the corresponding matrix elements from theoretical dipolar model, respectively.

In this system (where we will be referring to the resonators as “atoms”), we set the resistance of the magnetic atom at a constant ($20\ \Omega$) and vary the electric atom resistor (with a resistance R) to tune the electric response of the atom and, to a lesser extent, the bianisotropy.

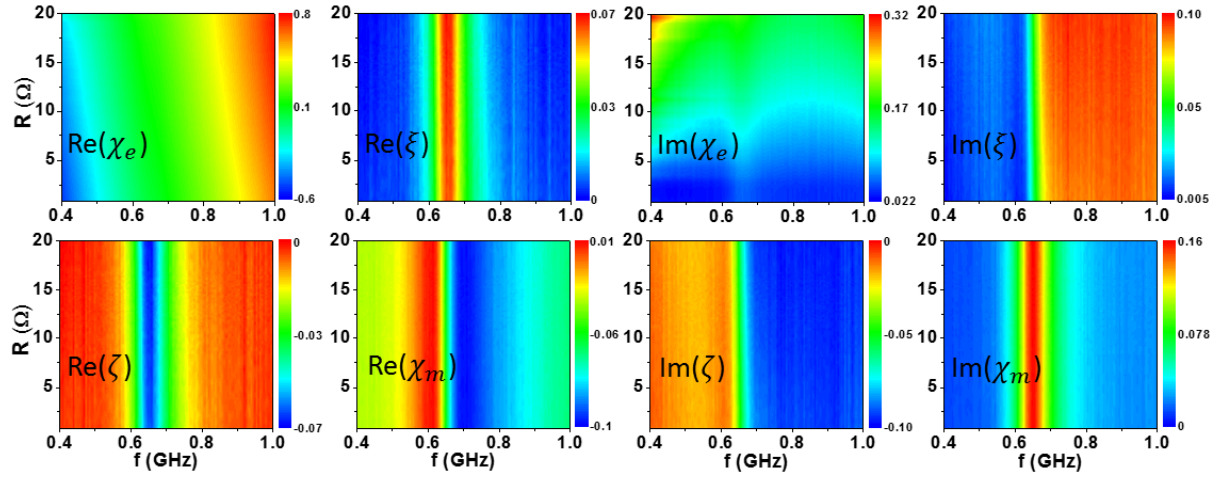


Figure 35: The real (left four panels) and imaginary (right four panels) of the constitutive matrix elements as a function of the electric atom resistance (R) and the frequency in GHz (f), before gauging. Reference plane is chosen to be at the electric atom.

We can see this in Figure 35, where the real parts (left-hand side) and imaginary parts (right-hand side) of χ_e , χ_m , ξ and ζ are plotted from experimental measurements. The reference plane for the extracted $[Y]$ matrix is chosen here to be at the electric atom, which confirms that varying the resistance of the electric atom mainly affects χ_e and does not significantly affect χ_m . We can see this system as one similar to the passive PT slab system in section 5.4, except, we are now varying the loss in the electric response rather than the magnetic response. The shift in the electric atom introduces the bianisotropy necessary for UZR. The effect of this shifting can be quantified using a dipolar model. We take the $[Y]$ matrix components of the individual electric and magnetic resonators (measured separately) and combine them via:

$$[S] = [A]^\dagger \cdot \begin{pmatrix} -\frac{2i}{\chi_{eA}} - 1 & -e^{ik\delta} & e^{ik\delta} \\ -e^{ik\delta} & -\frac{2i}{\chi_{eB}} - 1 & 0 \\ -e^{ik\delta} & 0 & -\frac{2i}{\chi_{mB}} - 1 \end{pmatrix}^{-1} \cdot [A] + [I], \quad (6.1)$$

$$\text{with } [A] = \begin{pmatrix} e^{-ik\delta} & e^{ik\delta} \\ 1 & 1 \\ 1 & -1 \end{pmatrix}.$$

Where χ_{eA} is the electric response of the electric resonator and χ_{eB} and χ_{mB} are the electric and magnetic responses of the magnetic resonator. The χ terms here are the electric and magnetic susceptibilities, which can be defined for a transmission line via equation 3.17. The matrix A converts the incident fields into the local fields at the resonators, so $[A] \cdot (a_1, a_2)^T = (E_A, E_B, H_B)^T$. The central matrix then converts these local fields into the generated dipole moments and the $[A]^\dagger$ matrix then converts these moments into the scattered fields. The total fields are then given by the sum of the scattered and incident fields, hence the addition of the identity matrix. The $e^{ik\delta}$ terms are the radiation coupling terms, with k being the wavenumber in the waveguide and δ being the distance between the resonators (in this case, -20mm). This model assumes that the dipoles are infinitesimal and so it will produce a scattering matrix with middle plane convention. Using the numerically fitted χ_{eA} , χ_{eB} and χ_{mB} from measurements to the individual atoms, we can see a good correspondence between the dipolar model and the measured data (Figure 34 (c)).

In order to prove PT symmetry, we must prove that the susceptibilities (i.e. the $[Y]$ matrix) have the form $[Y] = [Y_{PT}] + i\gamma_{bias}[I]$. We will do this in the same manner as we did in the previous section, by first choose a shifting gauge to set $\text{Re}(\chi_e) = \text{Re}(\chi_m)$, which can be done by setting $kL = \frac{1}{2} \tan^{-1} \left(\frac{\text{Re}(\epsilon) - \text{Re}(\mu)}{2\text{Im}(\xi)} \right)$, and then checking the parameter space to see where

$\text{Re}(\xi) = 0$. Any regions which satisfy this after the gauging can be automatically identified as being PT symmetric.

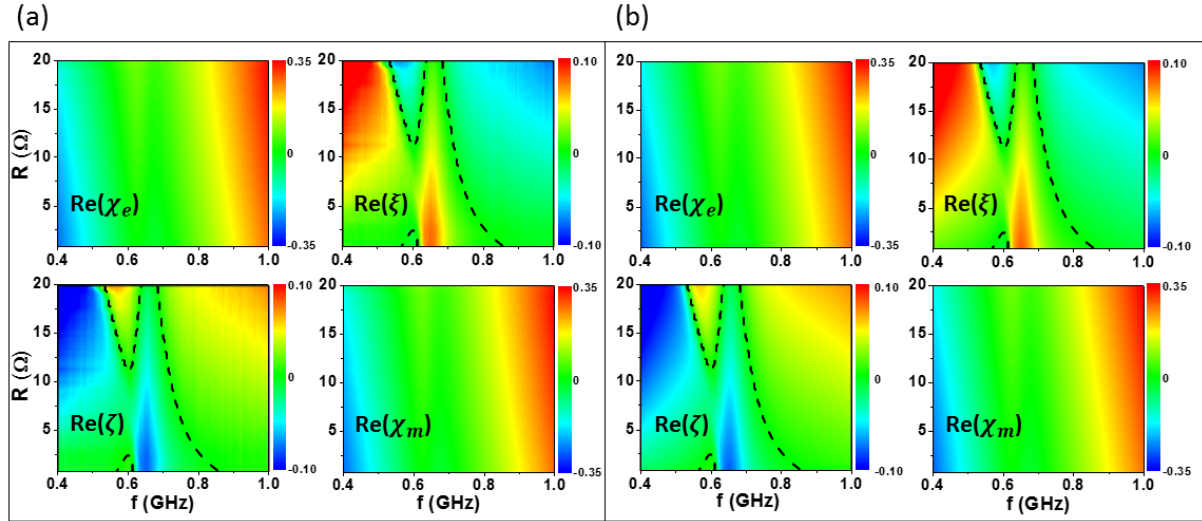


Figure 36: The constitutive matrix after choosing a gauge to have $\text{Re}(\chi_e) = \text{Re}(\chi_m)$, as a function of the electric atom resistance and the frequency in GHz (f). The four panels in (a) show the real part of Y-matrix elements extracted from experimental results. The four panels in (b) show the corresponding model results. The passive PT symmetry condition is indicated by the dashed line where $\text{Re}(\xi) = \text{Re}(\zeta) = 0$.

Results of this identification process can be seen in Figure 36 (a) and (b), where the colour maps show the real parts of the $[Y]$ matrix as a function of excitation frequency in GHz (f) and the resistance of the variable resistor in the electric atom (R). The four panels in (a) represent the measured experimental data and the four panels in (b) represent the fitted dipolar model. The dashed, black lines superimposed on the plots shows where the condition of $\text{Re}(\xi) = 0$ is satisfied, so we can say that the system is passively PT symmetric along these lines.

Now we need to confirm that this passive PT condition coincides with an exceptional point. Luckily, there are two exceptional points in this system, the first occurs at $(f_{Ex1}, R_{Ex1}) = (0.6 \text{ GHz}, 3 \text{ } \Omega)$ with $r_b = 0$ and the second occurs at $(f_{Ex2}, R_{Ex2}) = (0.62 \text{ GHz}, 13.9 \text{ } \Omega)$ with $r_f = 0$. To depict this, we will use the previously defined figure of merit: $(|r_f| - |r_b|) / (|r_f| +$

$|r_b|)$ which is equal to +1 for $r_b = 0$ with $r_f \neq 0$ and -1 for $r_f = 0$ with $r_b \neq 0$. This merit is plotted in Figure 37 (a), where the two exceptional points are labelled as Ex1 and Ex2.

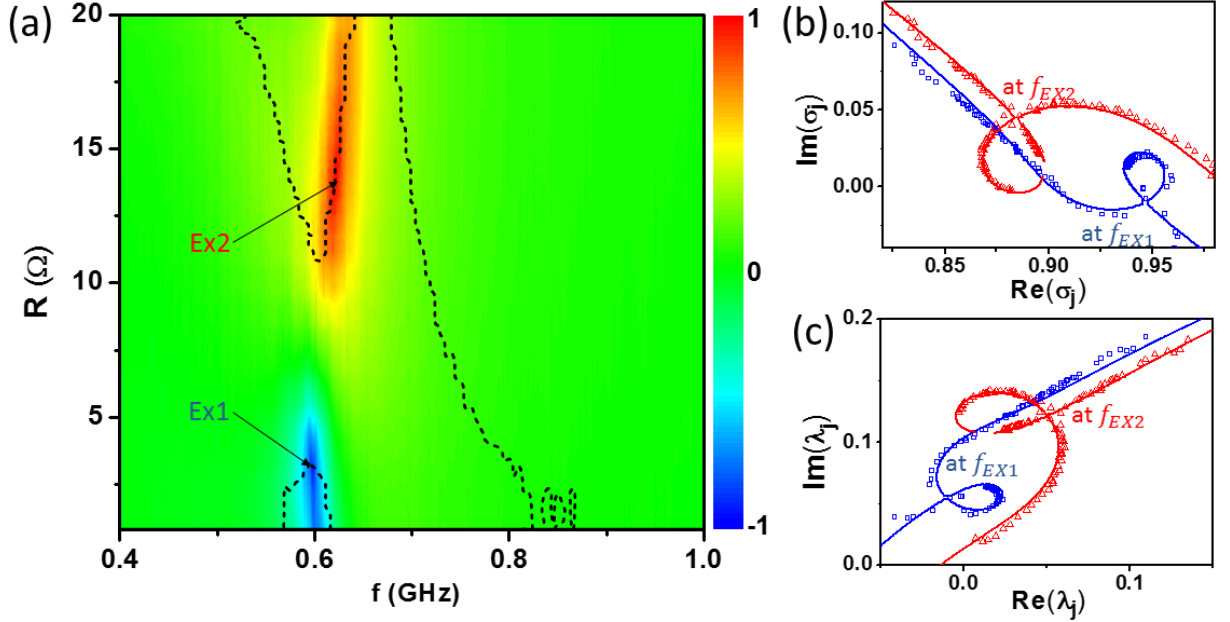


Figure 37: Unidirectional zero reflection merit and eigenvalue plots. (a) Shows the UZR merit, defined by $(|r_f| - |r_b|)/(|r_f| + |r_b|)$, extracted from experimental data. The dotted line shows where our passive PT asymmetry condition can be satisfied. (b) Eigenvalues of S at the frequency of exceptional point 1 (blue) and exceptional point 2 (red) by varying tunable resistance R . (c) Eigenvalues of Y at the frequency of exceptional point 1 (blue) and exceptional point 2 (red) by varying tunable resistance R .

Superimposed on this is a dashed line showing where the passive PT symmetry condition is satisfied. As we can see, both of the exceptional points lie on these lines. This confirms that these exceptional points correspond to a passive PT symmetry of the system. To further explore the system, we also parametrically plot the real and imaginary parts of the eigenvalues of the scattering matrix (σ_j) and the $[Y]$ matrix (λ_j) as a function of the electric atom resistance and at their exceptional point frequencies (Figure 37 (b) and (c), respectively).

The symbols in the plots represent the experimentally measured data and the solid lines are the dipolar model results. In both cases, we can see splitting behaviour similar to what we saw in the theory section, though in this case the paths are more complex due to dispersion in the

system. To summarise, we have seen that a transmission line which can be tuned to have UZR can be shown to have passive PT symmetry along certain contours in its phase space and the exceptional points lie in along these contours. We therefore state that a two-port system displaying UZR can be seen as having passive PT symmetry.

6.2. Using Tunnel Diodes to Produce Gain:

Tunnel diodes have been used in other microwave metamaterials to counteract inherent losses ([58,59]). These diodes consist of a very thin (about 10 nm) and heavily doped p-n junction. This heavy doping creates a large bandgap such that the energy of conducting electron states in the n-doped side is approximately equal to that of the energy of the valence hole states in the p-doped side. This approximate equivalence allows for an additional phenomenon not seen in standard diodes: quantum tunnelling. This tunnel current has the curious property that, as the bias voltage is increased (in the forward bias direction), it increases to a peak and then decreases to zero for large voltages. This can be explained by considering the energy levels of two bands: when a small bias voltage is applied, the energy of the conduction band electrons in the n-doped side increases relative to that of the valence holes in the p-doped side. This allows a small current to tunnel through the junction and form a “tunnel current”. As the bias voltage increases, the current reaches a maximum (at voltage V_p) as the number of electron states in the n-doped side matches the number of valence holes in the p-doped side. After this maximum, the energy levels start to become more mismatched and so the tunnel current starts to decrease. Eventually the bands become so mismatched that the tunnel current becomes negligible, this is marked by a minimum in the current going

through the diode (at voltage V_p). After this point, the main source of current becomes diffusion through the depletion region and the diode resumes normal operation. A depiction of this can be seen in Figure 38 (a), where the black line represents an ideal tunnel diode I-V curve.

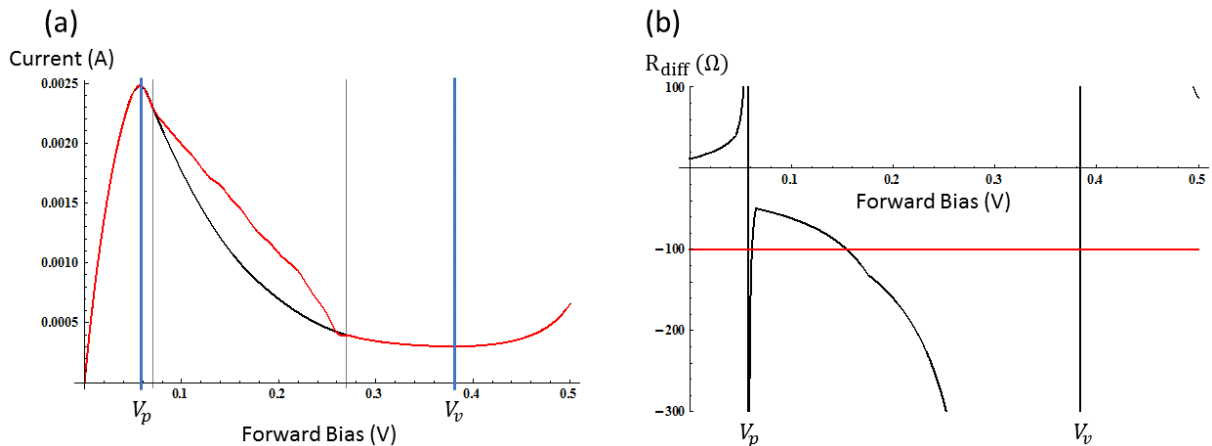


Figure 38: properties of a TD261 tunnel diode. (a) shows the measured (red) and idealised (black) I-V curves for a TD261 American Microsemiconductor tunnel diode. The idealisation was done by removing the unstable values (in between the thin, grey lines) and performing a second-order interpolation of the resulting data. The maximum of the tunnel current is marked by V_p and the valley is marked as V_v . (b) shows the differential resistance (dV/dI) of the idealised TD261 diode as a function of the forward bias voltage (black line) with reference line at -100 Ohms (red line). The peak and valley currents (V_p and V_v) can be seen where the differential resistance goes to infinity due to the conductance becoming zero.

The principle of operation for these diodes involves biasing them with a voltage between V_p and V_v . In this region, any small incoming AC voltage signals will induce oscillations about the bias point. Looking at Figure 38, we can see that these oscillations will experience an increasing current for decreasing voltage and a decreasing current for increasing voltage. This is what is known as negative differential resistance and this allows the tunnel diode to act as an amplifier when it is biased suitably.

This negative differential resistance (NDR), however, has some unwelcome side effects when the diode is used in a circuit. In Figure 38 (a), the red line shows the measured data for a TD261

(from American Microsemiconductor Inc.) attached to a voltage source via connecting leads. We can see that there is noisy behaviour in the current when the diode is operating in a certain part of its NDR region, between the grey lines. This behaviour has been observed by others ([109,110]) and results from so-called parasitic oscillations produced by the combination of the capacitance of the junction, the inductance of the connecting leads, and the negative resistance of the biased diode. In order to remove these oscillations, one must carefully design a measurement circuit to stabilise the system (e.g. putting the diode in parallel with a resistor). Unfortunately, a stable configuration was not found for the tunnel diodes we used, so instead a second order interpolation was used to smooth out the curve and give a more idealised, approximate I-V curve.

The differential resistance of the diode can be found by differentiating the I-V curve to give the conductance, and then inverting it to obtain the resistance. Based on other structures which use tunnel diodes in the low GHz range [58,59] and some numerical tests, the operating value of the NDR should be between -100 and -250 Ohms. Figure 38 (b) shows the differential resistance of the TD261 diode, with a red bar at -100 to show the minimum magnitude of R_{diff} we would like to achieve. We can see that the region between 80 mV and 250 mV should provide us with a range of NDR values within our -100 to -250 Ohm target region.

6.3. A Transmission Line Laser-Absorber:

For an experimental realisation of a laser-absorber, we require the real parts of both the χ_e and χ_m to be zero, meaning that we need to employ Lorentzian resonances. The easiest way to do this would be to design an electric and magnetic resonator with the same resonant

frequency. For our constitutive matrix, we will be using the lower-sign version of equation 5.18 with $\kappa = 0$, so that we will have a laser state for symmetric incidence and an absorbing state for antisymmetric incidence. This means that we will need to add gain into the electric resonator. Based on previous attempts at adding gain to microwave metamaterials, we will use a biased tunnel diode as our gain mechanism. To add the diode into our structure, we will need to make a gap in our resonating bar structure (similar to [59]). We will also add a second gap so that we can add a resistor for additional tunability. A detailed schematic of this structure can be seen in Figure 39, where the gaps for adding the variable resistors and diode are marked. The pads in the zoomed in section of the magnetic resonator were added to facilitate the addition of the variable resistor.

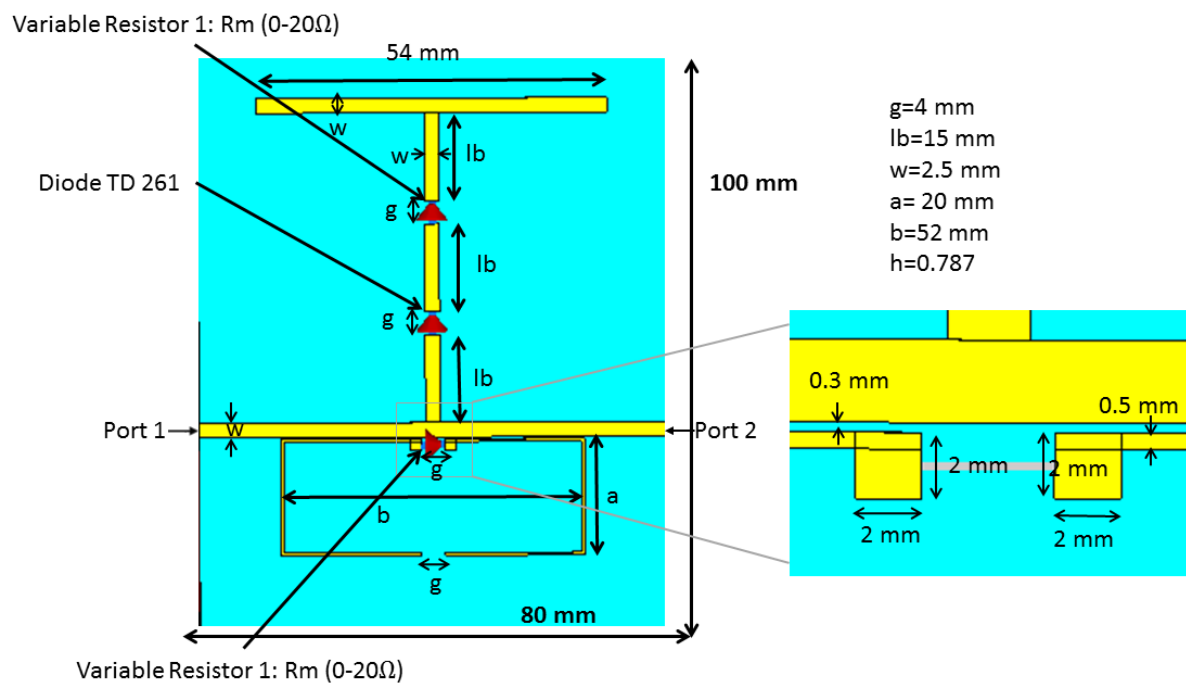


Figure 39: Detailed schematic of the original laser-absorber design. The dimensions of the structures are shown, along with the port configuration (connected via SMA connectors) and the arrangement of the resistors and diode. The quantity h is the distance between the waveguide strip and the ground plane (i.e. the thickness of the substrate).

The simulation setup of the structure can be seen in Figure 40 (a). The magnetic resonator is a relatively simple structure comprising of a split ring resonator with a variable resistor added to increase tunability.

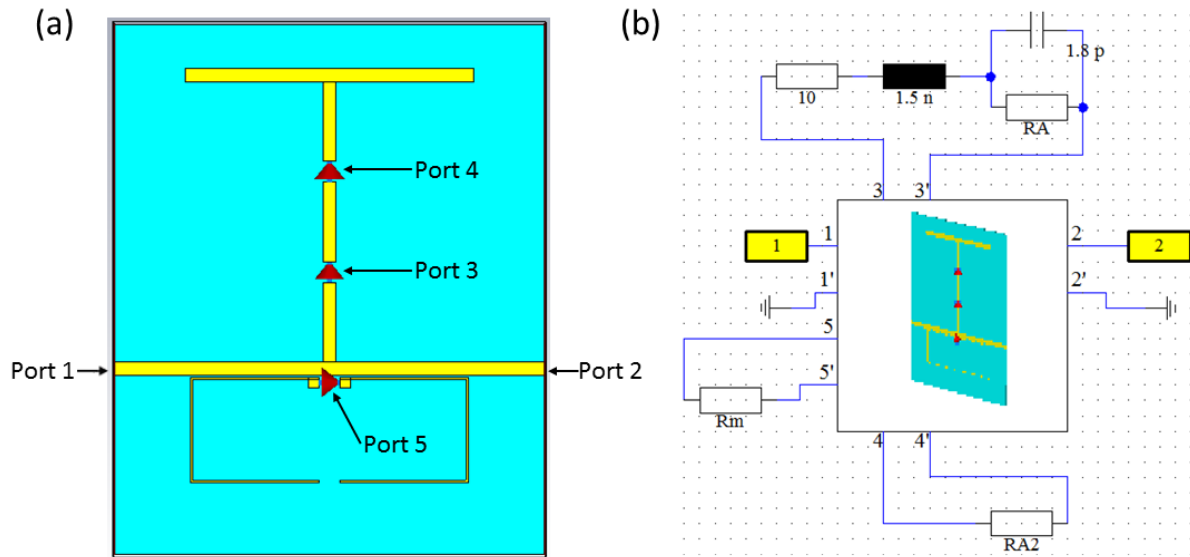


Figure 40: Initial laser-absorber design and ideal simulation setup. (a) shows the initial design of the laser-absorber, ports 1 and 2 are the measurement ports and ports 3, 4 and 5 are for modelling the diode and two variable resistors, respectively. (b) shows the solver blocks for the extra circuits, where the upper circuit connected to port 3 is the tunnel diode and the circuits connected to ports 4 and 5 are the variable resistors.

To model the tunnel diode in CST, we need an equivalent circuit model so that its S parameters can be calculated and fed into the simulation. The ideal gain device would simply be a negative value resistor. However, due to finite size and the materials involved, there is always some additional resistance, capacitance and inductance in the diode (these are often called “parasitic” parameters, due to their ability to degrade performance in circuits). The most commonly used model that takes these additional parameters into account is one similar to a capacitor with a gain dielectric: a resistor and inductor in series with a parallel capacitor and (negative) resistor (see the upper circuit in Figure 40 (b)). The values of the additional parameters are given by manufacturers and for the diode we will use (American Microsemiconductor TD261), the values are $C_p \sim 1.8$ pF, $R_p \sim 10$ Ω , $L_p \sim 1.5$ nH (approximate

signs are used as there can be significant variation due to manufacturing).

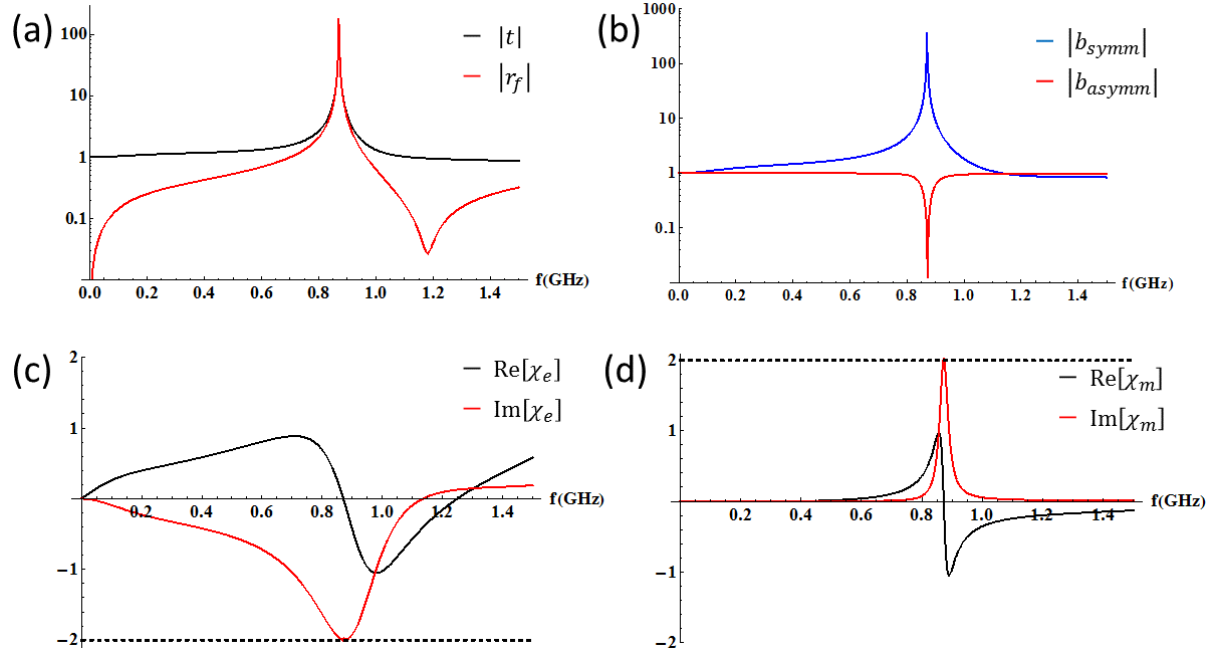


Figure 41: Simulated properties of the Initial laser-absorber design. (a) shows a log plot of the magnitude of the transmission (black line) and reflection (red line) coefficients. (b) shows a log plot of b under symmetric (blue) and antisymmetric (red) incidence. (c) and (d) are the electric and magnetic components of the $[Y]$ matrix, with black lines showing the real parts and the red lines showing the imaginary parts.

Figure 41 shows the simulated properties of this initial design when the parasitic diode properties are set to those above, RA (the negative resistance) is set to -110Ω and the variable resistors in the electric and magnetic atoms are set to 11.5Ω and 5Ω respectively. (a) shows the transmission and reflection coefficients in a log scale as a function of the frequency, where we can see significant amplification around the resonating frequency of 0.87 GHz, (b) shows the magnitude of b_2 under symmetric and antisymmetric incidence, confirming that we have amplification and absorption for these two states. (c) and (d) show the electric and magnetic components of the $[Y]$ matrix, where the black lines are the real parts and the red lines are the imaginary parts. The dotted lines at $+2$ and -2 are to show that we have reached our condition of $\chi_e = -2i$ and $\chi_m = 2i$.

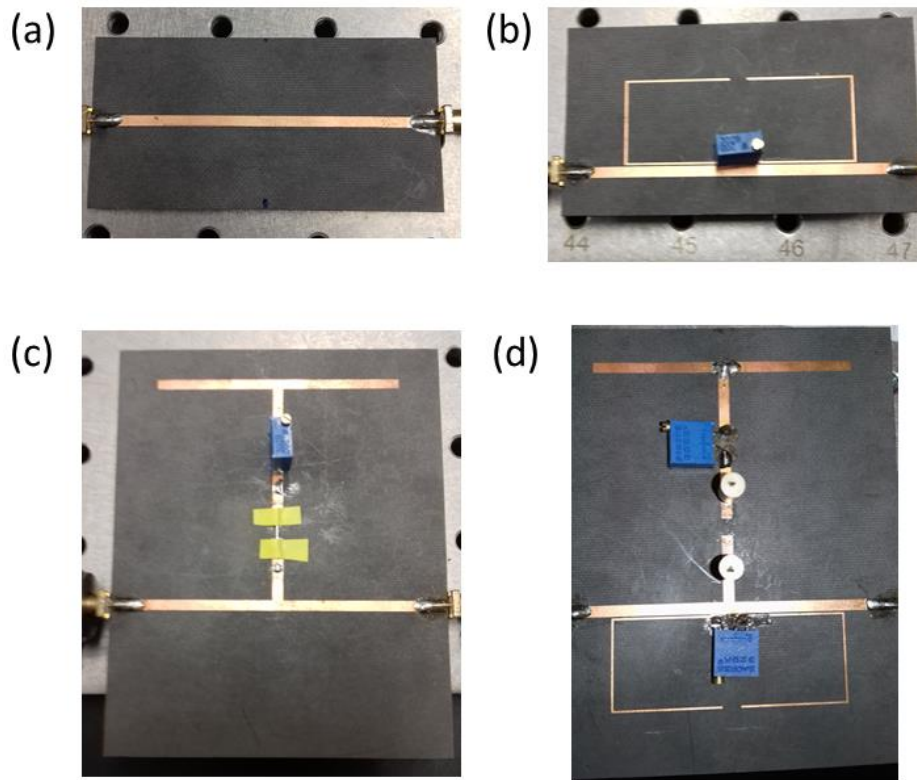


Figure 42: Pictures of the initial samples. (a) is a bare transmission line, (b) is the magnetic atom, (c) is the electric atom with a bar taped across the diode gap and (d) is the composite structure with an additional ground plane connection at the top of the electric resonator. The cylinders in (d) are inductors that were used to try to filter out the additional noise from the biasing cables.

The initial designs without the diode (Figure 42 (a), (b), (c)) showed a reasonable correspondence to simulations after some fitting, as can be seen in from the comparison of the S parameters in Figure 43, but it was beset by unforeseen problems. The variable resistors used in simulation did not take into account the substantial inductance generated by the solenoid structure inside the actual resistor. This inductance produced a shift in the resonating frequency of the magnetic atom by approximately 100MHz. Adding an inductance of 4nH to the resistor in the simulation produced a good fit between the resonant frequency of the measured and simulated S parameters of the magnetic atom (Figure 43 (a)).

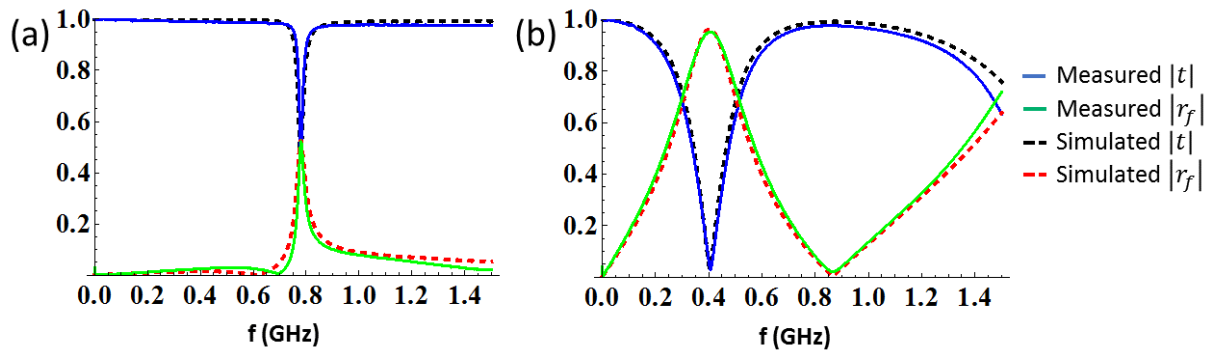


Figure 43: Comparison of the scattering parameters of the initial laser-absorber for experiment and simulation. A) shows the measured transmission (blue, solid line), measured reflectance (solid, green line), simulated transmission (dashed, black line) and simulated reflectance (dashed, red line) for the magnetic atom when its resistance is tuned to 3Ω and an inductance of $4nH$ is included in the simulation of the variable resistor. (b) shows the same parameters for the electric atom when a bar is placed across the diode gap and the resistor is tuned to its minimum.

We can explain this shift by representing the system as a circuit. The electric and magnetic resonators can be represented as a shunt and series impedance, labelled as Z_e and Z_m , which are shown in Figure 44.

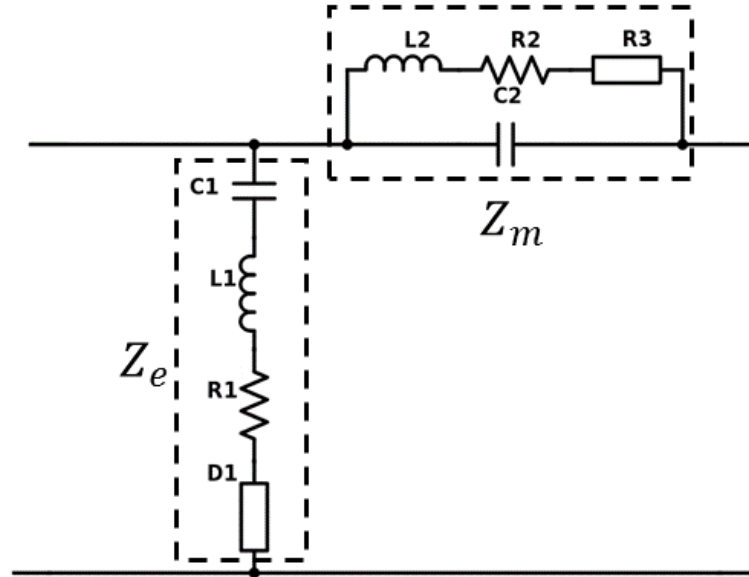


Figure 44: Equivalent circuit diagram for the laser-absorber system. The electric and magnetic resonators are represented by a shunt and series impedance (Z_e and Z_m , respectively) which are themselves described by the intrinsic resistance (R), capacitance (C) and inductance (L) of the structures. The additional components are the diode in the electric resonator (D1) and the variable resistor in the magnetic resonator (R3). We can model the diode with a circuit shown in Figure 40 (b) and the variable resistor can be modelled by a resistance in series with an inductor.

To model the extra inductance of the variable resistors, we simply need to replace R3 in the diagram with a resistor and inductor in series. As the resonant frequency of the magnetic resonator is approximately equal to $1/\sqrt{L_2 C_2}$, an additional inductance in R3 will effectively increase L_2 , which will decrease the resonant frequency. To calculate the scattering parameters of the system in terms of the impedances, we can use the ABCD matrix (equation 3.16) as our transfer matrix and follow the procedure in section 3.1.

Additionally, although the structures are almost exactly symmetric, the vector network analyser's male and female cable endings necessitated the use of a short male-male adapter. This adapter creates a small amount of bianisotropy in the transmission line, generating asymmetric reflections and meaning that the middle plane of the measured data is no longer in the centre of the atom. The diode was also found to be highly unstable in this configuration, generating a barely noticeable reduction in loss and also a great deal of noise (see Figure 45).

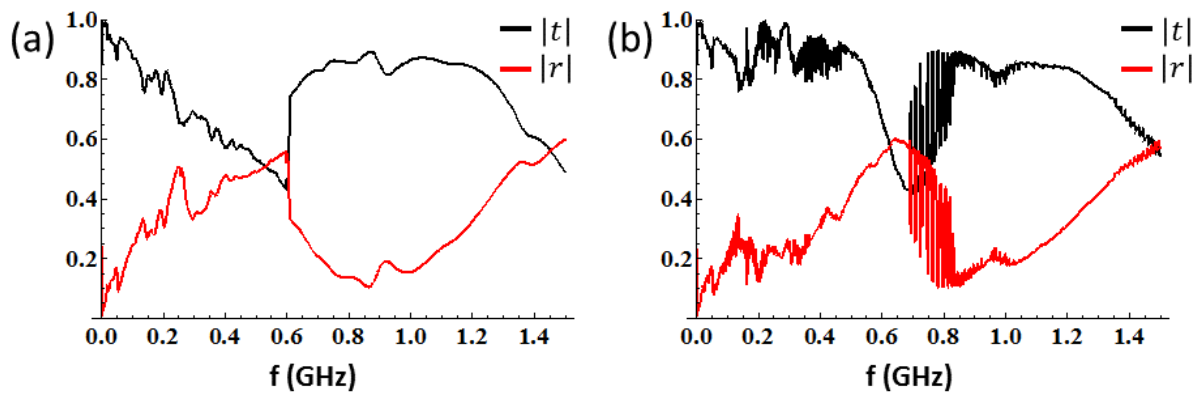


Figure 45: S parameters for the laser-absorber (with the diode) for different diode bias voltages. (a) shows the magnitude of the transmission and reflection coefficients for the structure for zero bias voltage. (b) shows the S parameters for a bias voltage of 200mV (i.e. within the NDR region). The S parameters for this case had to be time-averaged (100 times) due to fluctuations in the spectrum.

Taking inspiration from Xin *et al.* [58], we introduced a ground connection at the top of the electric atom (shown in Figure 42 (d)) and found that the diode was not only stable but also producing amplification. This amplification point was found to be close to a new zero in the

real part of χ_e with lower $\text{Im}(\chi_e)$, created via the zero-frequency Drude resonance of the ground plane connected resonator (similar to Figure 46 (b)).

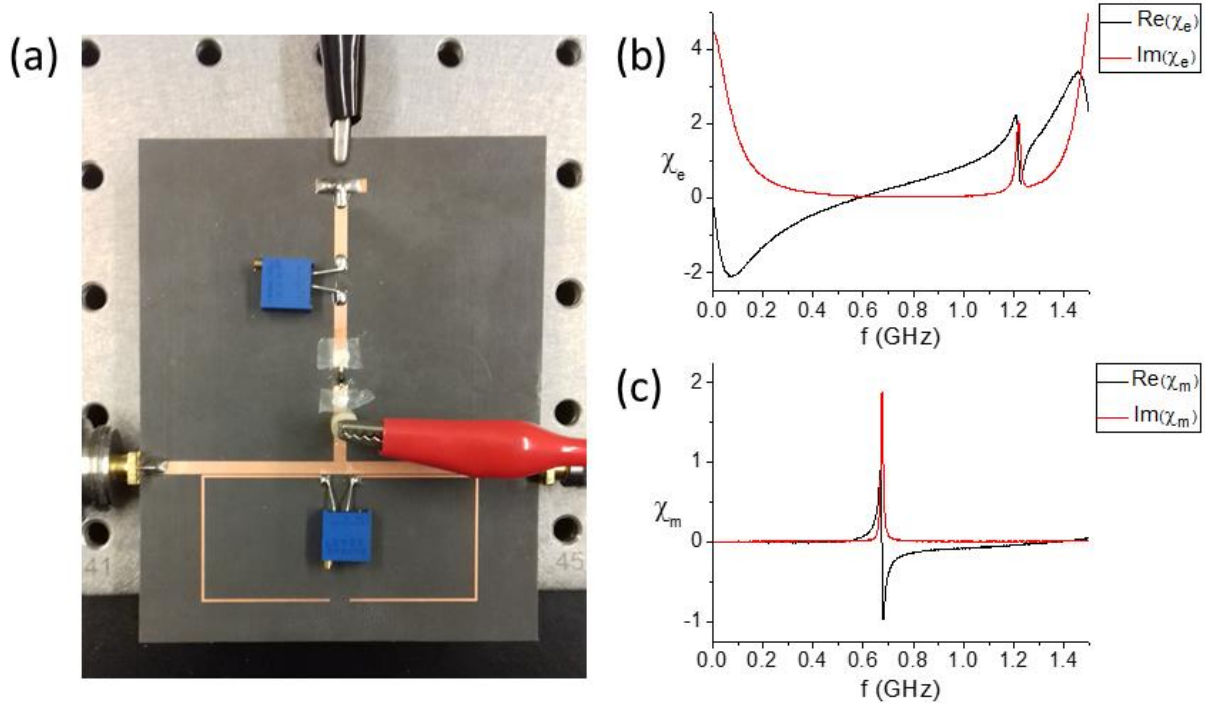


Figure 46: Redesigned laser-absorber. The structure, with the diode, inductor and bias connectors is shown in (a). (b) and (c) are the real (black) and imaginary (red) parts of χ_e and χ_m respectively. Both are measured without the biasing cables. We can see a zero in the real part of χ_e at 0.58 GHz.

We then redesigned the laser absorber, assuming that the amplification was due to this new, lower loss zero point in the susceptibility. We also changed the biasing setup to try and reduce the interference from the inductors/cables, removing one of the inductors and attaching the low port to the ground plane instead. This redesign can be seen in Figure 46 (a), where the red and black connectors are the high and low ports of the bias voltage supply. Figure 46 (b) shows χ_e vs. frequency, we can see that the real part (black line) has a zero at 0.58 GHz, so we expect the amplification to be strongest around this point. We have also tuned the resistance of the magnetic atom to satisfy the CPA condition (shown in Figure 46 (c)).

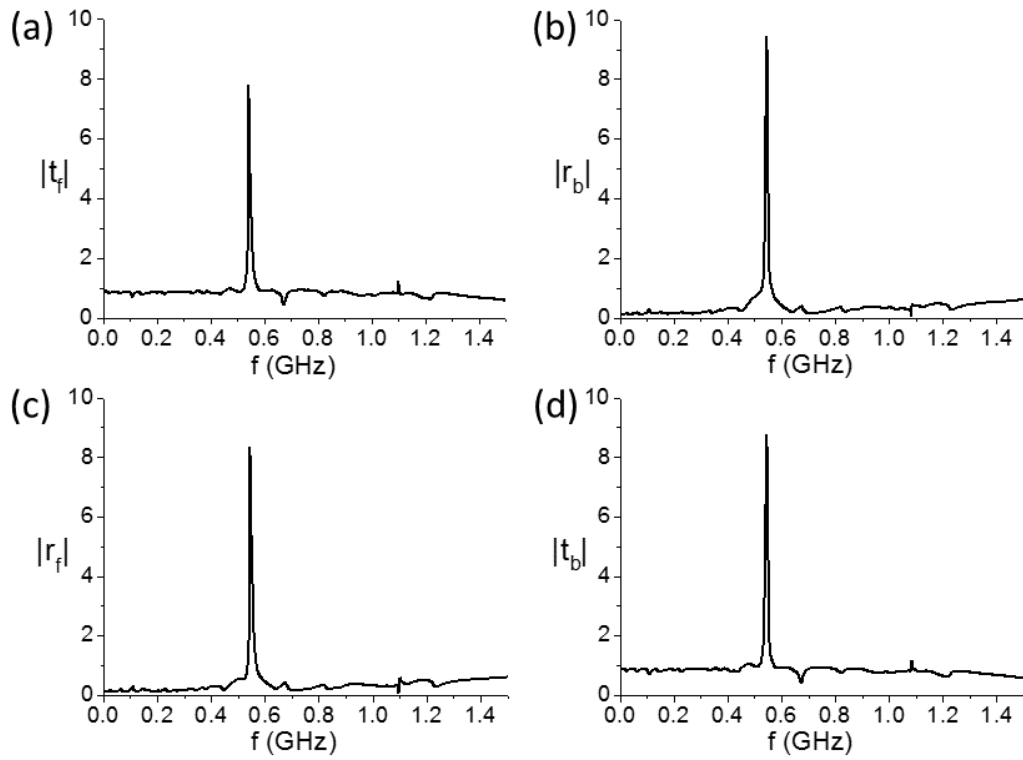


Figure 47: Magnitude of the $[S]$ matrix components of the adjusted laser-absorber with a TD261 tunnel diode biased to 280mV. (a) – (d) show the 4 components of the $[S]$ matrix, t_f, r_b, r_f and t_b , where maximum amplification occurs at $f = 0.543$.

The S parameters of this new structure are shown in Figure 47, where a TD261 tunnel diode was biased to 280 mV with the electric atom resistor set to its minimum ($\sim 0.8 \Omega$) and the magnetic atom resistor set to 3Ω . We can see significant amplification around $f = 0.543$ GHz, close to the $Re(\chi_e) = 0$ point of the unbiased structure.

Although the lasing and CPA points do not overlap for this design, we can still get quite close to our conditions on χ_e and χ_m at separate frequencies. The natural logarithms of the forwards and backwards scattered field amplitudes are shown in Figure 48 (a) and (b). Maximum amplification occurs at $f = 0.543$ GHz, where we have significant amplification of the transmission and reflection power for symmetric incidence (black lines in (a) and (b)). At this frequency point we have $\chi_e = 0.147 - 2.2i$ (Figure 48 (c)), which is close to our derived lasing condition.

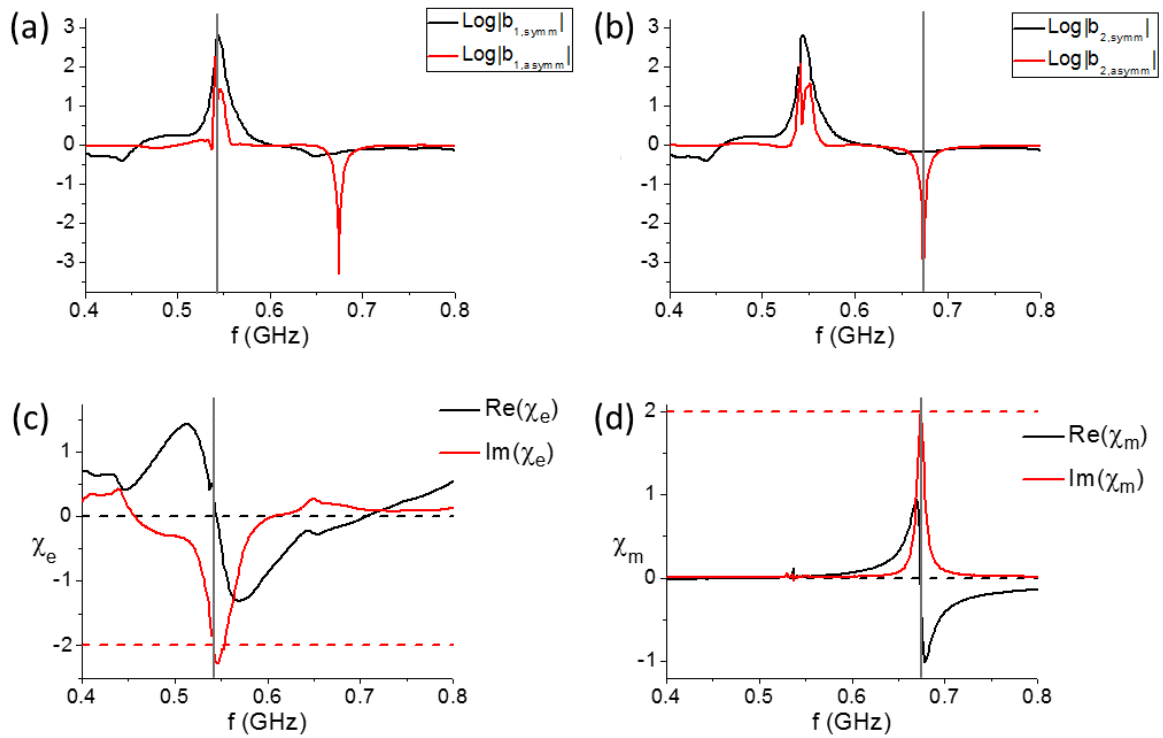


Figure 48: Scattered field magnitudes and constitutive parameters of the new LA design. (a) and (b) show the natural logarithm of the forwards and backwards scattered field magnitudes (respectively) for symmetric (black line) and antisymmetric (red line) incidence. We can see the lasing point at $f = 0.543$ GHz and the CPA point at $f = 0.543$ GHz. (c) and (d) shows the real (black solid lines) and imaginary (red solid lines) of χ_e and χ_m , where we have $\chi_e = 0.147 - 2.2i$ at the lasing point and $\chi_m = -0.08 + 1.97i$ and the CPA point. Then grey lines in (a) and (c) show the frequency of maximum amplification for comparison and those in (b) and (d) show the frequency of maximum absorption.

Further up the frequency spectrum at $f = 0.674$ GHz we also have our CPA point. Here we see a large reduction in the scattered fields for asymmetric incidence (red lines in (a) and (b)) and we have $\chi_m = -0.08 + 1.97i$ (Figure 48 (d)), which is again very close to our derived value.

We have assumed that the zero point in the real part of χ_e was important for amplification but the correspondence is still unclear. To investigate further, we designed three electric resonators of different sizes to see where maximum amplification occurs. The three resonators are shown in Figure 49 (a)-(c), where the design parameter, lb , is set to 13mm, 15mm and 17mm respectively.

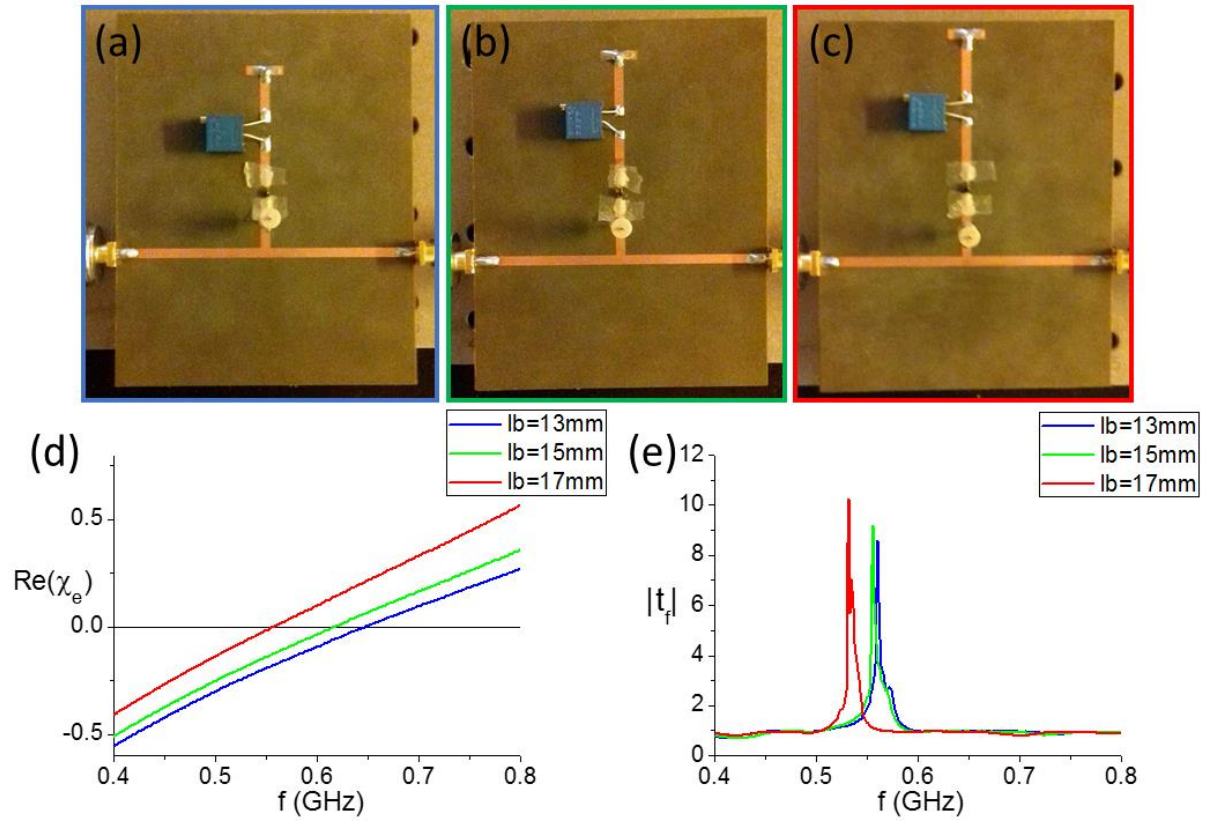


Figure 49: Three electric resonators of different sizes and their properties. (a)-(c) are pictures of the resonators, the parameter lb is set to 13mm, 15mm and 17mm respectively. The real parts of χ_e of the structures are shown in (d). The blue, green and red lines correspond to the structures where $lb=13\text{mm}$, 15mm and 17mm respectively. We see zeroes in the real parts of χ_e at 0.65 GHz (blue), 0.62 GHz (green) and 0.56 GHz (red). (e) shows the forwards transmittance for the structures when the diode is biased to 280mV, maximum amplification points are at 0.561 GHz (blue), 0.556 GHz (green) and 0.532 GHz (red).

The total height of these resonators is 47mm, 53mm and 59mm. The value of lb does not affect the Drude resonance much but it does affect the resonant frequency of the next highest resonance of the atom, blue shifting it for smaller lb and red shifting it for larger lb . This in turn affects the zero point of $\text{Re}(\chi_e)$ by changing the contribution of this higher order resonance in the frequency range we are interested in. We can see this in the real parts of χ_e in Figure 49 (d), where the zero point is red/blue shifted due to the shifting of the higher resonance. The χ_e here were measured without the biasing cables attached. The zeroes in this case are located at 0.65 GHz (blue), 0.62 GHz (green) and 0.56 GHz (red). We then attached the biasing cables to the structures, applied a bias of 280 mV, and measured the S parameters.

The magnitude of the forward transmittance ($|t_f|$) can be seen in Figure 49 (e), where the maximum amplification occurs at 0.561 GHz (blue), 0.556 GHz (green) and 0.532 GHz (red). The other scattering parameters (t_b , r_f and r_b) also have similar peaks at these frequencies. These peaks do seem to follow the trend of the χ_e zeroes in that a lower frequency zero point corresponds to a lower peak amplification frequency. However, the amplification peaks are all red shifted by about 100 MHz from the zero points, likely due to the additional DC resistance generated by the diode when it is biased. In addition to the shifting, the amplification points are more compressed in their spacing than the χ_e zero points, suggesting that the additional capacitance of the biased diode is also affecting the position of the amplification peaks.

6.4. Chapter Summary:

In this chapter, we have observed UZR experimentally in a tuneable transmission line system with mixed electric and magnetic responses. We then used the gauging process to confirm that the UZR points are associated with PT symmetric contours in a medium's frequency-gain/loss phase space. We then showed that by combining a magnetic CPA with a electric resonant amplifier, it is possible in principle to achieve two, PT-transformed lasing and absorbing states simultaneously in a subwavelength system. However, a very careful design process is necessary to match the zero points of $Re(\chi_e)$ and $Re(\chi_m)$ and ensure that the reflection and transmission coefficients are matched. We showed that the amplification peaks for the tunnel diode resonator are related to the zero points of $Re(\chi_e)$ but that care must be taken to include the properties of the biased diode, not just the manufacturing parameters. For anyone else attempting to design such a structure, we suggest first experimentally

confirming the position of the amplification peak and then designing the magnetic resonance to match it.

7. Conclusions and Outlook:

We have studied PT symmetry in electromagnetism for plane wave propagation and found that these systems can contain exceptional points. In the context of tangential PT symmetry, with the potential varying in the direction of propagation, these exceptional points correspond to unidirectional zero reflection (UZR). We then formulated a link between the effective constitutive matrix of a system and its scattering matrix, showing that an exceptional point in the scattering matrix (UZR) could be linked to one in the effective constitutive matrix. By analysing the form of the constitutive matrix at an exceptional point, we found that it can be described as having passive PT symmetry. Furthermore, we showed that exceptional points can be related to PT symmetric contours in the phase space of a medium, even when the system did not have obvious PT symmetry (e.g. the constant intensity potentials or transmission line system). We confirmed this with a transmission line system, where we found that the UZR points lay on PT symmetric contours in the frequency-resistance space.

We have also looked at the concept of lasing and coherent absorption from an effective medium perspective, deriving conditions for the two behaviours in a variety of situations. We showed that a system could exhibit lasing and absorption at the same frequency (known as a laser-absorber) if the effective constitutive matrix has a certain form. We also found that by separating the gain and loss into two stacked slabs, we could significantly increase the energy absorbed by the lossy slab, highlighting possible applications in sensing technologies. An attempt at designing a laser-absorber was then made using a tunnel diode to produce the necessary gain. We managed to observe situations close to lasing and coherent absorption but they were separated in frequency space due to design oversights. We then designed

several lasing “atoms” of differing sizes to determine the lasing condition. We found that the point of maximum amplification seems to correspond to the low loss $Re(\chi_e) = 0$ points in the structures, though additional effects such as the varying resistance and capacitance of the diode also played a part.

Looking to the future, I hope to see more research into PT symmetry which takes advantage of our new parity operator. In particular, the mixing of electric and magnetic responses to achieve exceptional points would enable more work on PT symmetry in the subwavelength regime. This could also lead to more applications utilizing UZR, as the exceptional points can be accessed at lower frequencies and gain/loss values, making integration into technologies easier. In a similar vein, I hope that the work on the laser absorber stimulates research into the possibility of using such systems to enhance sensors. We showed that this amplification can occur in subwavelength systems (given suitably large gain/loss parameters), which should make technological integration easier.

Appendix A: Resonance Shifting via Coupling

Putting resonators in the vicinity of each other will allow them to couple through their scattered fields. This can either increase or decrease the resonant frequency depending on the strength of the resonance, the frequency and the distance between the resonators. The dipolar model works by considering the local fields at the resonators and converting them into scattered fields which we can then add to the incident fields to get the scattering parameters. In one dimension, the dipolar model can be used to calculate the scattering matrix for two coupled, coplanar, electric resonances (described by χ_{e1} and χ_{e2}) via

$$[S] = [A]^\dagger \cdot \begin{pmatrix} \frac{-2i}{\chi_{e1}} - 1 & -e^{ik\delta} \\ -e^{ik\delta} & \frac{-2i}{\chi_{e2}} - 1 \end{pmatrix}^{-1} \cdot [A] + [I],$$

with $[A] = \begin{pmatrix} 1 & 1 \\ 1 & 1 \end{pmatrix}$

To illustrate the shifting effect, we will set the two resonators equal to each other ($\chi_{e1} = \chi_{e2} = \chi$) and work with a coupling scenario similar to the bar resonance example in section 2.4, where $\delta \sim 1.5\lambda$ at the resonating frequency. We set $\chi = \omega \left(\frac{\omega_p^2}{\omega^2 - \omega_r^2 - i\gamma\omega} \right)$ with $\omega_p = 2 \times 10^4$, $\omega_r = 1.57 \times 10^{10}$ (2.5 GHz) and $\gamma = 7 \times 10^8$. The resulting χ_e extracted from the $[S]$ matrix can be seen in Figure 50, where the black lines show the real (solid) and imaginary (dashed) parts of χ_e when we set $\delta = 0.18$ (which is $\sim 1.5\lambda$ at 2.5 GHz). At this separation, we see no shifting of the resonant frequency. However, when we change the coupling distance to 0.16 (blue line) or 0.2 (red line), we see a shifting of the resonant frequency to 2.515 GHz or 2.485 GHz (respectively).

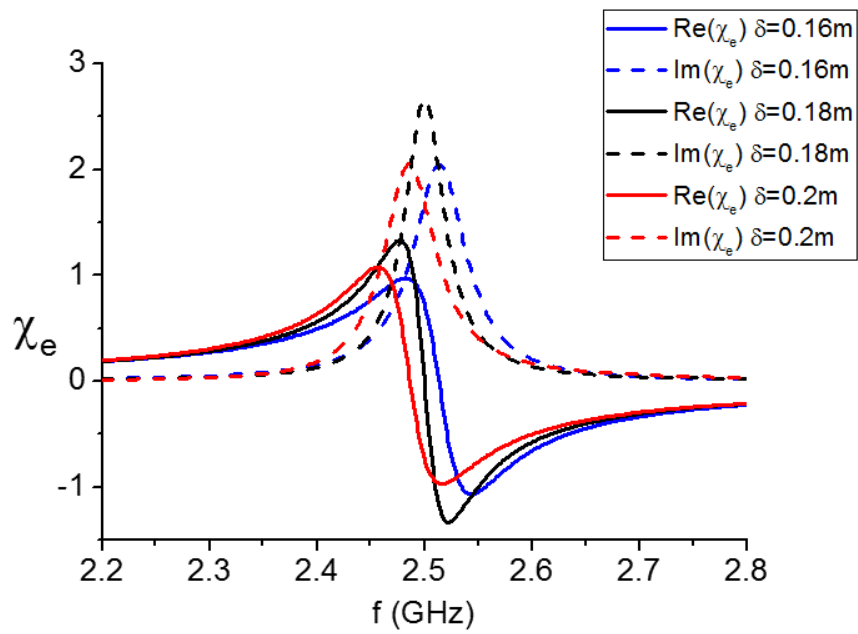


Figure 50: Resonance shifting in the dipolar model. This graph shows the real (solid lines) and imaginary (dashed lines) parts of the extracted χ_e for two, coupled electric resonators when the coupling length is varied. The black line corresponds to $\delta = 0.18$ where we have minimal shifting. The blue and red lines correspond to a decrease and increase (respectively) of the coupling length. We can see the blue/redshifting of the resonant frequency of the medium, similar to what we saw with the bar metasurface.

References:

1. C. M. Bender and S. Boettcher, "Real Spectra in Non-Hermitian Hamiltonians Having PT Symmetry", *Phys. Rev. Lett.* 80, 5243 (1998).
2. V. A. Fedotov, P.L. Mladyonov, S. L. Prosvirnin, A. V. Rogacheva, Y. Chen and N. I. Zheludev, "Asymmetric Propagation of Electromagnetic Waves through a Planar Chiral Structure", *Phys. Rev. Lett.* 97, 167401 (2006).
3. D. Schurig, J. J. Mock, B. J. Justice, S. A. Cummer, J. B. Pendry, A. F. Starr and D. R. Smith, "Metamaterial Electromagnetic Cloak at Microwave Frequencies", *Science*, Vol. 314, Issue 5801, pp. 977-980 (2006).
4. R. A. Shelby, D. R. Smith and S. Schultz, "Experimental verification of a negative index of refraction", *Science* 292, 5514, 77-79 (2001).
5. H. D. Young, "University Physics", 7th Ed., p.887, Addison Wesley, 1992.
6. H. D. Young, "University Physics", 7th Ed., p.1043, Addison Wesley, 1992.
7. B. Wood and J. B. Pendry, "Metamaterials at zero frequency", *J. Phys.: Condens. Matter*, 19, 076208 (2007).
8. Metglas technical bulletin, <http://www.metglas.com/assets/pdf/2714a.pdf>
9. J. Kröll, J. Darmo and K. Unterrainer, "Terahertz optical activity of sucrose single-crystals", *Vibrational Spectroscopy*, Vol. 43, 2, p324-329 (2007).
10. J. B. Pendry, A. J. Holden, D. J. Robbins, and W. J. Stewart, "Magnetism from conductors and enhanced nonlinear phenomena", *IEEE Transactions on Microwave Theory and Techniques*, Vol. 47, No. 11, (1999).
11. I. Freestone, N. Meeks, M. Sax and C. Higgit, "The Lycurgus Cup – A Roman Nanotechnology", *Gold Bulletin*, vol. 40, 4, p.270-277 (2007).
12. M. I. Stockman, "Nanoplasmonics: The physics behind the applications", *Physics Today* (2011).
13. O. Benson, "Assembly of hybrid photonic architectures from nanophotonic constituents", *Nature* 480, 193-199 (2011).
14. R. Liu, C. Ji, J.J. Mock, J.Y. Chin, T.J. Cui and D.R. Smith, "Broadband Ground-Plane Cloak", *Science* 323, 5912, 366-369 (2009).
15. M. Yin, X. Y. Tian, H. X. Han and D. C. Li, "Free-space carpet-cloak based on gradient index photonic crystals in metamaterial regime", *Appl. Phys. Lett.* 100, 124101 (2012).
16. L. La Spada, T. M. McManus, A. Dyke, S. Haq, L. Zhang, Q. Cheng and Y. Hao, "Surface Wave Cloak from Graded Refractive Index Nanocomposites", *Scientific Reports* 6, 29363 (2016).
17. J. Neu, B. Krolla, O. Paul, B. Reinhard, R. Beigang, and M. Rahm, "Metamaterial-based gradient index lens with strong focusing in the THz frequency range", *Optics Express* Vol. 18, Issue 26, pp. 27748-27757 (2010).
18. N. Kundtz and D. R. Smith, "Extreme-angle broadband metamaterial lens", *Nature Materials* 9, 129–132 (2010).

19. F. Gauffillet, S. Marcellin and E. Akmansoy, "Dielectric Metamaterial-Based Gradient Index Lens in the Terahertz Frequency Range", *IEEE Journal of selected topics in quantum electronics* 23, 4 (2017).
20. D. R. Smith, J.B. Pendry and M. C. K. Wiltshire, "Metamaterials and negative refractive index", *Science* 305, 788-792 (2004).
21. J. Valentine, S. Zhang, T. Zentgraf, E. Ulin-Avila, D. A. Genov, G. Bartal and X. Zhang, "Three-dimensional optical metamaterial with a negative refractive index", *Nature* 455, 376-379 (2008).
22. S. P. Burgos, R. de Waele, A. Polman and H. A. Atwater, "A single-layer wide-angle negative-index metamaterial at visible frequencies", *Nature Materials* 9, 407-412 (2010).
23. C. Rockstuhl and F. Lederer, "Negative-index metamaterials from nanoapertures", *Phys. Rev. B* 76, 125426 (2007).
24. G. Dolling, C. Enkrich, M. Wegener, C. M. Soukoulis and S. Linden, "Low-loss negative-index metamaterial at telecommunication wavelengths", *Optics Letters* 31, 12 p. 1800-1802 (2006)
25. G. Dolling, M. Wegener, C. M. Soukoulis and S. Linden, "Negative-index metamaterial at 780 nm wavelength", *Optics Letters* 32, 1 (2007).
26. R. A. Depine and A. Lakhtakia, "A new condition to identify isotropic dielectric-magnetic materials displaying negative phase velocity", *Microw. and Opt. tech. lett.*, vol. 41, 4, p315-316 (2004).
27. J. B. Pendry, "Negative Refraction Makes a Perfect Lens", *Phys. Rev. Lett.* 85, 3966 (2000).
28. J. B. Pendry and S. A. Ramakrishna, "Focusing light using negative refraction", *J. Phys.: Condens. Matter* 15, 6345-6364 (2003).
29. X. Zhang and Z. Liu, "Superlenses to overcome the diffraction limit", *Nature Materials* 7, 435-41 (2008).
30. D. Schurig and D. R. Smith, "Negative index lens aberrations" *Phys. Rev. E* 70, 065601 (2004).
31. C. G. Parazzoli, R. B. Greegor, J. A. Nielsen, M. A. Thompson, K. Li, A. M. Vetter and M. H. Tanielian, "Performance of a negative index of refraction lens" *Appl. Phys. Lett.* 84, 3232 (2004).
32. J. B. Pendry, "Perfect cylindrical lenses" *Opt. Expr.* 11, 7, 755-760 (2003).
33. A. Grbic and G. V. Eleftheriades, "Overcoming the Diffraction Limit with a Planar Left-Handed Transmission-Line Lens" *Phys. Rev. Lett.* 92, 117403 (2004).
34. T. Yang, H. Chen, X. Luo and H. Ma, "Superscatterer: Enhancement of scattering with complementary media" *Opt. Expr.* 16, 22, 18545 (2008).
35. Y. Lai, J. Ng, H. Y. Chen, D. Han, J. Xiao, Z. Zhang and C. T. Chan, "Illusion Optics: The Optical Transformation of an Object into Another Object" *Phys. Rev. Lett.* 102, 253902 (2009).
36. Y. Lai, H. Chen, Z. Zhang and C. T. Chan, "Complementary Media Invisibility Cloak that Cloaks Objects at a Distance Outside the Cloaking Shell" *Phys. Rev. Lett.* 102, 093901 (2009).

37. H. Chen, X. Zhang, X. Luo, H. Ma and C. T. Chen, "Reshaping the perfect electrical conductor cylinder arbitrarily" *N. J. Phys.* 10, 113016 (2008).
38. C. Li, X. Meng, X. Liu, F. Li, G. Fang, H. Chen, C. T. Chen, "Experimental realization of a broadband illusion optics device", *Phys. Rev. Lett.* 105, 233906 (2010).
39. S. Zhang, F. Liu, T. Zentgraf and J. Li, "Interference-induced asymmetric transmission through a monolayer of anisotropic chiral metamolecules", *Phys. Rev. A* 88, 023823 (2013).
40. R. Singh, E. Plum, C. Menzel, C. Rockstuhl, A. K. Azad, R. A. Cheville, F. Lederer, W. Zhang and N. I. Zheludev, "Terahertz metamaterial with asymmetric transmission", *Phys. Rev. B* 80, 153104 (2009).
41. S. V. Zhukovsky, A. V. Novitsky and V. M. Galynsky, "Elliptical dichroism: operating principle of planar chiral metamaterials", *Opt. Lett.* 34, 13, 1988 (2009).
42. A. Drezet, C. Genet, J.-Y. Laluet and T. W. Ebbesen, "Optical chirality without optical activity: How surface plasmons give a twist to light", *Opt. Expr.* 16, 17, 12559 (2008).
43. C. Menzel, C. Helgert, C. Rockstuhl, E.-B. Kley, A. Tünnermann, T. Pertsch and F. Lederer, "Asymmetric Transmission of Linearly Polarized Light at Optical Metamaterials", *Phys. Rev. Lett.* 104, 253902 (2010).
44. M. Kang, J. Chen, H.-X. Cui, Y. Li and H.-T. Wang, "Asymmetric transmission for linearly polarized electromagnetic radiation", *Opt. Expr.* 19, 9, 8347-8356(2011).
45. C. E. Kreigler, M. S. Rill, S. Linden and M. Wagner, "Bianisotropic Photonic Metamaterials", *IEEE Journal of Selected Topics in Quantum Electronics*, Vol. 16, No. 2 (2010).
46. V. S. Asadchy, Y. Ra'di, J. Vehmas, and S. A. Tretyakov, "Functional Metamirrors Using Bianisotropic Elements", *Phys. Rev. Lett.* 114, 095503 (2015).
47. M. S. Rill, C. E. Kriegler, M. Thiel, G. von Freymann, S. Linden, and M. Wegener, "Negative-index bianisotropic photonic metamaterial fabricated by direct laser writing and silver shadow evaporation", *Optics Letters*, 34, 1, p.19.
48. S. A. Tretyakov, C. R. Simovski, and M. Hudlička, "Bianisotropic route to the realization and matching of backward-wave metamaterial slabs", *Phys. Rev. B* 75, 153104 (2007).
49. J. Skaar and K. Seip, "Bounds for the refractive indices of metamaterials", *J. Phys. D: Appl. Phys.* 39, 6 (2006) p. 1226–1229.
50. H. S. Lee, C. Awada, S. Boutami, F. Charra, L. Douillard and R. E. de Lamaestre, "Loss mechanisms of surface plasmon polaritons propagating on a smooth polycrystalline Cu surface", *Optics Express*, vol. 20, 8, 8974-8981 (2012).
51. M. Kuttge, E. J. R. Vesseur, J. Verhoeven, H. J. Lezec, H. A. Atwater and A. Polman, "Loss mechanisms of surface plasmon polaritons on gold probed by cathodoluminescence imaging spectroscopy", *Appl. Phys. Lett.* 93, 113110 (2008).
52. F. Monticone and A. Alu, "Invisibility exposed: physical bounds on passive cloaking", *Optica*, 3, 7, 718-724 (2016).
53. R. M. Fano, "Theoretical Limitations on the Broadband Matching of Arbitrary Impedances," R.L.E. Technical Report No. 41 (1948).

54. O. Hess, S. Wuestner, A. Pusch, K. L. Tsakmakidis, and J. M. Hamm, "Gain and plasmon dynamics in active negative-index metamaterials", *Phil. Trans. Royal Soc. A* 369, 3525–3550 (2011).
55. O. Hess, J. B. Pendry, S. A. Maier, R. F. Oulton, J. M. Hamm and K. L. Tsakmakidis, "Active nanoplasmonic metamaterials", *Nature Materials* 11, 573-584 (2012).
56. S. Wuestner, A. Pusch, K. L. Tsakmakidis, J. M. Hamm and O. Hess, "Overcoming losses with gain in a negative refractive index metamaterial", *Phys. Rev. Lett.* 105, 127401 (2010).
57. K. H. Krishna, K. V. Sreekanth and G. Strangi, "Dye-embedded and nanopatterned hyperbolic metamaterials for spontaneous emission rate enhancement", *J. Opt. Soc. Am. B* 33, 6, 1038-1043 (2016).
58. T. Jiang, K. Chang, L.-M. Si, L. Ran and H. Xin, "Active Microwave Negative-Index Metamaterial Transmission Line with Gain", *Phys. Rev. Lett.* 107, 205503 (2011).
59. D. Ye, K. Chang, L. Ran and H. Xin, "Microwave gain medium with negative refractive index", *Nat. Comms.* 5, 5841 (2014).
60. Y. Yuan, B.-I. Popa and S. A. Cummer, "Zero loss magnetic metamaterials using powered active unit cells", *Optics Express*, vol. 17, 18, 16135 (2009).
61. T. J. Cui, D. Smith and R. Liu, "Metamaterials: Theory, Design, and Applications", Springer Science & Business Media, (2009) p.65.
62. O. B. Vorobyev, "Energy Density of Macroscopic Electric and Magnetic Fields in Dispersive Medium with Losses", *Progress In Electromagnetics Research B*, Vol. 40, 343–360, (2012).
63. A. Zangwill, "Modern electrodynamics", p.641, Cambridge University Press (2013)
64. N. Engheta and R. W. Ziolkowski, "Metamaterials: Physics and Engineering Explorations", John Wiley & Sons, (2006).
65. K. E. Oughston, "Electromagnetic and Optical Pulse Propagation 1: Spectral Representations in Temporally Dispersive Media", p.215, Springer (2007).
66. M. Shamonin, E. Shamonina, V. Kalinin and L. Solymar, "Resonant frequencies of a split-ring resonator: Analytical solutions and numerical simulations", *Microwave and optical technology letters*, 44, 2 (2005) p. 133-136.
67. A. Radovskaya, M. Shamonin, C. J. Stevens, G. Faulkner, D. J. Edwards, E. Shamonina and L. Solymar, "Resonant frequencies of a combination of split rings: Experimental, analytical and numerical study", *Microwave and optical technology letters*, 46, 5 (2005) p. 472-476.
68. D. R. Smith, S. Schultz, P. Markos and C. M. Soukoulis, "Determination of effective permittivity and permeability of metamaterials from reflection and transmission coefficients", *Phys. Rev. B* 65, 195104 (2002).
69. S. Zhang, Y.-S. Park, J. Li, X. Lu, W. Zhang and X. Xiang, "Negative Refractive Index in Chiral Metamaterials", *Phys. Rev. Lett.* 102, 023901 (2009).
70. T. Feng, F. Liu, W. Y. Tam and J. Li, "Effective parameters retrieval for complex metamaterials with low symmetries", *EPL* 102, 1, 18003 (2013).

71. C. M. Bender, S. Boettcher and P. Meisinger, "PT-Symmetric Quantum Mechanics", J. Math. Phys. 40, 5 (1999) p.2201-2229.
72. C. M. Bender, "Introduction to \mathcal{PT} -symmetric quantum theory", Contemporary Physics, 46, 4, 277-292 (2005).
73. W.D. Heiss and S. Radu, "Quantum chaos, degeneracies, and exceptional points", Phys. Rev. E 52, 4762 (1995).
74. T. Gao, E. Estrecho, K. Y. Bliokh, T. C. H. Liew, M. D. Fraser, S. Brodbeck, M. Kamp, C. Schneider, S. Höfling, Y. Yamamoto, F. Nori, Y. S. Kivshar, A. G. Truscott, R. G. Dall and E. A. Ostrovskaya, "Observation of non-Hermitian degeneracies in a chaotic exciton-polariton billiard", Nature 526, 554-558 (2015).
75. C. Dembowski, H.-D. Gräf, H. L. Harney, A. Heine, W. D. Heiss, H. Rehfeld and A. Richter, "Experimental observation of the topological structure of exceptional points", Phys. Rev. Lett. 86, 787 (2001).
76. C. Dembowski, B. Dietz, H.-D. Gräf, H. L. Harney, A. Heine, W. D. Heiss and A. Richter, "Encircling an exceptional point", Phys. Rev. E 69, 056216 (2004).
77. T. J. Milburn, J. Doppler, C. A. Holmes, S. Portolan, S. Rotter and P. Rabl, "General description of quasiadiabatic dynamical phenomena near exceptional points", Phys. Rev. A 92, 052124 (2015).
78. M. Liertzer, L. Ge, A. Cerjan, A. D. Stone, H. E. Türeci, and S. Rotter, "Pump-Induced Exceptional Points in Lasers", Phys. Rev. Lett. 108, 173901 (2012).
79. L. Feng, Z. J. Wong, R.-M. Ma, Y. Wang and X. Zhang, "Single-mode laser by parity-time symmetry breaking", Science 346, 972-975 (2014).
80. C. E. Rüter, K. G. Makris, R. El-Ganainy, D. N. Christodoulides, M. Segev and D. Kip, "Observation of parity-time symmetry in optics", Nat. Phys. 6, 192-195 (2010).
81. B. Bagchi, C. Quesne, and M. Znojil, "Generalized Continuity Equation and Modified Normalization in PT-Symmetric Quantum Mechanics", Mod. Phys. Lett. A 16, 2047 (2001).
82. M. Lawrence, N. Xu, X. Zhang, L. Cong, J. Han, W. Zhang and S. Zhang, "Manifestation of PT Symmetry Breaking in Polarization Space with Terahertz Metasurfaces", Phys. Rev. Lett. 113, 093901 (2014).
83. R. Fleury, D. Sounas and A. Alù, "An invisible acoustic sensor based on parity-time symmetry", Nat. Comm. 6, 5905 (2015).
84. J. Gear, F. Liu, S. T. Chu, S. Rotter and J. Li, "Parity-time symmetry from stacking purely dielectric and magnetic slabs", Phys. Rev. A. 91, 033825 (2015).
85. H. Benisty, A. Lupu and A. Degiron, "Transverse periodic PT symmetry for modal demultiplexing in optical waveguides", Phys. Rev. A 91, 053825 (2015).
86. F. Yang and Z. L. Mei, "Guiding SPPs with PT-symmetry", Scientific reports 5, 14981 (2015).
87. B. Peng, S. K. Özdemir, F. Lei, F. Monifi, M. Gianfreda, G. L. Long, S. Fan, F. Nori, C. M. Bender and L. Yang, "Parity-time-symmetric whispering-gallery microcavities", Nat. Phys. 10, 394-398 (2014).

88. L. Ge, Y. D. Chong and A. D. Stone, "Conservation relations and anisotropic transmission resonances in one-dimensional PT-symmetric photonic heterostructures", *Phys. Rev. A* 85, 023802 (2012).
89. Z. Lin, H. Ramezani, T. Eichelkraut, T. Kottos, H. Cao and D. N. Christodoulides, "Unidirectional Invisibility Induced by PT-Symmetric Periodic Structures", *Phys. Rev. Lett.* 106, 213901 (2011).
90. H. Alaeian and J. A. Dionne, "Parity-time-symmetric plasmonic metamaterials", *Phys. Rev. A* 89, 033829 (2014).
91. S. Savoia, G. Castaldi, V. Galdi, A. Alù and N. Engheta, "Tunneling of obliquely incident waves through PT-symmetric epsilon-near-zero bilayers", *Phys. Rev. B* 89, 085105 (2014).
92. A. Lupu, H. Benisty and A. Degiron, "Using optical PT-symmetry for switching applications", *Photonics and Nanostructures – Fundamentals and Applications* 12 (2014) p. 305–311.
93. A. Guo, G. J. Salamo, D. Duchesne, R. Morandotti, M. Volatier-Ravat, V. Aimez, G. A. Siviloglou, and D. N. Christodoulides, "Observation of PT-Symmetry Breaking in Complex Optical Potentials", *Phys. Rev. Lett.* 103, 093902 (2009).
94. Y. Sun, W. Tan, H.-Q. Li, J. Li and H. Chen, "Experimental Demonstration of a Coherent Perfect Absorber with PT Phase Transition", *Phys. Rev. Lett.* 112, 143903 (2014).
95. S. Bittner, B. Dietz, U. Günther, H. L. Harney, M. Miski-Oglu, A. Richter and F. Schäfer, "PT Symmetry and Spontaneous Symmetry Breaking in a Microwave Billiard", *Phys. Rev. Lett.* 108, 024101 (2012).
96. L. Feng, Y.-L. Xu, W. S. Fegadolli, M.-H. Lu, J. E. B. Oliveira, V. R. Almeida, Y.-F. Chen and A. Scherer, "Experimental demonstration of a unidirectional reflectionless parity-time metamaterial at optical frequencies", *Nature Materials* 12, 108-113 (2013).
97. M. P. Khanna, "Introduction to Particle Physics", PHI Learning Pvt. Ltd. (1999), p.73.
98. A. Salam and J. Strathdee, "On goldstone fermions", *Physics Letters*, 49B, 5, 465-467 (1974).
99. K. G. Makris, A. Brandstötter, P. Amblichl, Z. H. Musslimani and S. Rotter, "Wave propagation through disordered media without backscattering and intensity variations", *Light Sci. Appl.* 6, e17035 (2017).
100. S. Longhi, "PT-symmetric laser absorber", *Phys. Rev. A* 82, 031801 (2010).
101. Y. D. Chong, L. Ge and A. Douglas Stone, "PT-Symmetry Breaking and Laser-Absorber Modes in Optical Scattering Systems", *Phys. Rev. Lett.* 106, 093902 (2012).
102. S. Longhi and L. Feng, "PT-symmetric microring laser-absorber", *Optics Lett.* 39, 17, p.5026-5029 (2014).
103. Z. J. Wong, Y.-L. Xu, J. Kim, K. O'Brien, Y. Wang, L. Feng and X. Zhang, "Lasing and anti-lasing in a single cavity", *Nature Photonics* 10, 796-801 (2016).

- 104.H. Hodaiei, A. U. Hassan, S. Wittek, H. Garcia-Gracia, R. El-Ganainy, D. N. Christodoulides and M. Khajavikhan, "Enhanced sensitivity at higher-order exceptional points", *Nature* 548, 187-191 (2017).
- 105.W. Chen, S. K. Özdemir, G. Zhao, J. Wiersig and L. Wang, "Exceptional points enhance sensing in an optical microcavity", *Nature* 548, 192-196 (2017).
- 106.N. I. Landy, S. Sajuyigbe, J. J. Mock, D. R. Smith and W. J. Padilla, "Perfect Metamaterial Absorber", *Phys. Rev. Lett.* 100, 207402 (2008).
- 107.F. Ding, Y. Cui, X. Ge, Y. Jin and S. He, "Ultra-broadband microwave metamaterial absorber", *Appl. Phys. Lett.* 100, 103506 (2012).
- 108.Y. J. Yoo, S. Ju, S. Y. Park, Y. J. Kim, J. Bong, T. Lim, K. W. Kim, J. Y. Rhee and Y. Lee, "Metamaterial Absorber for Electromagnetic Waves in Periodic Water Droplets", *Scientific Reports* 5, 14018 (2015).
- 109.M. Bao and K. L. Wang, "Accurately measuring current-voltage characteristics of tunnel diodes", *IEEE Transactions on Electron Devices* 53, 10 (2006).
- 110.L. Wang, J. M. L. Figueiredo, C. N. Ironside and E. Wasige, "DC Characterization of Tunnel Diodes Under Stable Non-Oscillatory Circuit Conditions", *IEEE Transactions on Electron Devices* 58, 2 (2011).